Porous MXene Synthesis and Applications for Batteries

by

Maiwen Zhang

A thesis

presented to the University of Waterloo

in fulfillment of the

thesis requirement for the degree of

Doctor of Philosophy

in

Chemical Engineering

Waterloo, Ontario, Canada, 2022

©Maiwen Zhang 2022

Examining Committee Membership

The following served on the Examining Committee for this thesis. The decision of the Examining Committee is by majority vote.

External Examiner	Dr. Anna Ignaszak Associate Professor
Supervisor(s)	Dr. Aiping Yu Professor
Internal Member	Dr. Eric Croiset Professor
Internal Member	Dr. David Simakov Associate Professor
Internal-external Member	Dr. Mustafa Yavuz Professor

Author's Declaration

This thesis consists of material all of which I authored or co-authored: see Statement of Contributions included in the thesis. This is a true copy of the thesis, including any required final revisions, as accepted by my examiners.

I understand that my thesis may be made electronically available to the public.

Statement of Contributions

The body of this thesis is based on a combination of both published and unpublished works. Various sections are adapted from the following list of publications.

Chapter 3 of this thesis consists of a paper that was co-authored by myself; my supervisor, Dr. A. Yu; Mr. R. Liang; Dr. N. Yang; Dr. R. Gao; Dr. Y. Zheng; Dr. Y.P. Deng; Dr. Y. Hu and Dr. Z. Chen. Dr. A. Yu conceived the concept and initiated the project. I performed synthesis, electrochemical measurements and characterizations with assistance from Mr. R. Liang, Dr. R. Gao and Dr. Y.P. Deng. DFT modeling is performed by Dr. N. Yang. All authors reviewed and commented the manuscript.

"Eutectic Etching toward In-Plane Porosity Manipulation of Cl-Terminated MXene for High-Performance Dual-Ion Battery Anode". Advanced Energy Materials, 2021, 2102493.

Chapter 4 of this thesis consists of a manuscript that was co-authored by myself; my supervisor, Dr. A. Yu; Mr. R. Liang; Dr. R. Gao; Mr. S. Habibpour; Dr. Y.P. Deng; Dr. Y. Jiang; Dr. Y. Hu and Dr. Z. Chen. I designed and carried out the material synthesis, performed electrochemical analysis and prepared the draft. Mr. R. Liang helped with manuscript revision. Dr. R. Gao; Mr. S. Habibpour and Dr. Y.P. Deng assisted with the material characterization. All authors reviewed the manuscript.

"Vacancy and Growth Modulation of Cobalt Hexacyanoferrate by Porous MXene for Zinc Ion Batteries", under preparation.

Chapter 5 of this thesis consists of a manuscript that was co-authored by myself; my supervisor, Dr. A. Yu; Mr. R. Liang; Dr. R. Gao; Dr. Y.P. Deng and Dr. Z. Chen. Dr. A. Yu conceived the concept and initiated the project. I prepared samples, performed electrochemical tests and prepared the draft. Dr. R. Gao and Dr. Y. P. Deng helped with the characterizations. Mr. R. Liang helped with manuscript revision. All authors reviewed the manuscript.

"Porous Cl-terminated MXene Promoted Horizontal Growth of Zn Electrodeposition towards Non-dendritic Zn Anode", under preparation.

Abstract

Efficient electrochemical energy storage devices are of particular importance for accelerating the widespread adaption of renewable energy, and electrode materials are critical to achieve optimal system performance. MXene (transition metal carbides and/or nitrides) are recently discovered two-dimensional materials with desirable properties such as metallic conductivity and high hydrophilicity. They have shown promises in applications such as lithium ion, zinc ion and dual ion batteries, but limitations such as hazardous precursor, uncontrollable edge terminations and low surface area have restricted fulfillment of their potentials. Moreover, insights into the precise mechanism of MXene in composite formation and electrochemical reactions are still limited.

To address the above issues, this thesis mainly focuses on developing novel strategy to synthesize high surface area porous MXene with uniform terminations, while probing their capability as high-performance electrodes for different types of battery systems. Particular focus is placed on investigating the influence of uniform Cl-termination and in-plane porosity on MXene when used as dual-ion battery anode. Afterwards, functions of the porous MXene as Prussian blue analogue (PBA) crystal growth inducing host for composite material and zinc ion redistribution protective layer for dendrite-free Zn anode are systematically investigated.

Firstly, a novel one-step eutectic mixture etching method is developed to synthesize Cl-terminated MXene ($Ti_3C_2Cl_2$) with abundant in-plane porosity through carefully controlling the phase transition of the etchants. Specifically, precise selection of etching parameters and salt mixture composition activates a mechanism that enables both pore generation and preservation

through timely formation of solid salt particles within the material structure. The resulting in-plane porous MXene sheets exhibit homogeneously distributed mesoporosity and four-folds expansion in surface area to 85 $m^2 g^{-1}$. X-ray spectroscopy characterizations reveal predominately edge Cl-terminations with minimal oxidation on the as-synthesized samples, which ensure orderly crystal arrangement. Meanwhile, density functional theory calculations confirm lower diffusion barrier that are beneficial for ion diffusion. When evaluated as anode for dual ion batteries, the optimized porous $Ti_3C_2Cl_2$ achieves a high specific capacity and excellent capacity retention. This work opens a green chemistry approach of incorporating in-plane mesoporosity to MXenes for electrochemical application and provides insights for environmental responsible development in the field of energy storage.

Secondly, the porous MXene is utilized as multifunctional host material to manipulate the morphology and crystallinity of cobalt hexacyanoferrate (CoHCF). It is discovered that the negative charges on the MXene surface can induce formation of high surface area CoHCF with reduced defects, which improves the material resilience toward reversible Zn^{2+} intercalation /deintercalation. Combined with the high conductivity of porous MXene, the CoHCF/MXene composite achieves superior electrochemical performance as cathode material for zinc ion battery, delivering a high capacity of 197 mAh g^{-1} and robust capacity retention of 94.4% over 3000 cycles. This work unveiled the inducing effect of MXene when used as template to grow Prussian blue analogues, paving way for its broad composite chemistry.

In the last section, the porous MXene is adapted in a surface engineering strategy as coating layer to regulate the electrodeposition of Zn^{2+} towards dendrite-free Zn anode. Its uniform surface

charge serves to homogenize the surface electric field for even deposition, while its crystal structure resemblance with the Zn (0002) plane promotes growth of the specific crystal plane known to favor layer-by-layer deposition. Moreover, porous structure of the MXene nanosheet is also favorable for ensuring sufficient ion diffusion and electrolyte coverage during high-rate cycling. Given these advantages, the MXene coated zinc foil achieves long period cycling of over 2000 hours at a high current density of 10 mA cm^{-2}, promoting the development of zinc anodes for large-scale energy storage.

In summary, this work opens a green chemistry approach to synthesize in-plane porous MXenes, which resolves the long-standing issue of limited porosity and low surface area of MXene. Meanwhile, the proposed effect on inducing ordered CoHCF crystal growth provides insights for designing MXene-based composite material with well-controlled crystal structure. In terms of energy storage application, this thesis addresses the importance of MXene termination and porosity in two application scenarios, as DIBs anode material and as protective layers for Zn anode, offering deep understanding on the relations between the structural properties of MXene and electrochemical behavior.

Acknowledgements

I would like to send my sincere gratitude to my supervisor Prof. Aiping Yu for her guidance and advice throughout my studies, also for providing me the freedom and opportunities to explore a wide range of research areas in electrochemistry. Her comments are valuable to my study and life. I would not finish my Ph.D. without her being my inspiring mentor and supplying enlightening advice and endless support. Also, I would like to acknowledge my Ph.D. thesis examining committee members: Prof. Anna Ignaszak, Prof. Eric Croiset, Prof. David Simakov, Prof. Mustafa Yavuz for their time and suggestions.

Meanwhile, I would like to thank Dr. Yi Pei and Dr. Wenwen Liu for training me with battery analysis, and Dr. Ricky Tjandra for his assistance when I first joined the group. Also, I want to thank my group members Mr. Ruilin Liang, Dr. Rui Gao, Mr. S. Habibpour, Dr. Yi Jiang and Dr. Ya-Ping Deng for their assistance and accompany. Moreover, thank you my mother, father, grandmother and my best friend Zhifang Zhang for endless love and useful advice for both my studies and life. Special thanks to my parents for financial support, encouragement and love. I would not fulfill so much without your help.

Finally, I would like to acknowledge the funding sources, Natural Sciences and Engineering Research Council of Canada, University of Waterloo, the Waterloo Institute for Nanotechnology for the financial support.

Table of Contents

Examining Committee Membership ii
Author's Declaration iii
Statement of Contributions iv
Abstract vi
Acknowledgements ix
List of Figures xiii
List of Tables xviii
List of Abbreviations xix
Chapter 1 Introduction 1
1.1 MXene 1
1.1.1 Background 1
1.1.2 Synthesis 2
1.1.3 Properties 8
1.2 Battery 11
1.2.1 Introduction 11
1.2.2 Porosity in Battery Electrode Materials 14
1.2.3 Lithium-Ion Battery 17
1.2.4 Dual Ion Battery 19
1.2.5 Zinc Ion Battery 23
1.3 Motivation and Thesis Structure 29
Chapter 2 Experimental Methods 31
2.1 Physical Characterization 31
2.1.1 Scanning Electron Microscopy 31
2.1.2 Transmission Electron Microscopy 31
2.1.3 Energy Dispersive X-ray Spectroscopy 32
2.1.4 X-ray Photoelectron Spectroscopy 33
2.1.5 X-ray Diffraction 35

2.1.6 X-ray Adsorption Spectroscopy....37
2.1.7 Thermogravimetric Analysis....41
2.1.8 Gas Adsorption Analysis....41
2.1.9 Contact Angle....43
2.2 Electrochemical Characterization....44
2.2.1 Galvanostatic Charge Discharge....44
2.2.2 Galvanostatic Intermittent Titration Technique....46
2.2.3 Cyclic Voltammetry....46
2.2.4 Electrochemical Impedance Spectroscopy....49
Chapter 3 Eutectic Etching toward In-Plane Porosity Manipulation of Cl-Terminated MXene for High-Performance Dual-Ion Battery Anode....53
3.1 Introduction....53
3.2 Experimental Section....55
3.3 Results and Discussion....59
3.3.1 Material Characterization....59
3.3.2 Electrochemical Results....66
3.3.3 Structural Analyzation....71
3.3.4 Full Cell Performance....78
3.4 Conclusion....79
Chapter 4 Vacancy and Growth Modulation of Cobalt Hexacyanoferrate by Porous MXene for Zinc Ion Batteries....81
4.1 Introduction....81
4.2 Experimental Section....83
4.3 Results and Discussion....85
4.3.1 Material Characterization....85
4.3.2 Electrochemical Performance....97
4.3.3 *Ex-situ* Characterization....100
4.4 Conclusion....103

Chapter 5 Porous Cl-terminated MXene Promoted Horizontal Growth of Zn Electrodeposition Towards Non-Dendritic Zn Anode 105
5.1 Introduction 105
5.2 Experimental Section 107
5.3 Results and Discussion 109
5.3.1 Structural Characterization of MXene 109
5.3.2 Anodes Electrochemical Performance 114
5.3.3 Full Cell Electrochemical Performance 129
5.4 Conclusion 131
Chapter 6 Summary and Future Perspectives 132
6.1 Summary 132
6.2 Future Outlook 134
Letters of Copyright Permission 137
References 138

List of Figures

Figure 1-1. Typical structures and compositions of MXene.[3] Copyright 2021, WILEY-VCH. ...2

Figure 1-2. Scheme of molten salt etching of $Ti_3C_2Cl_2$ from Ti_3AlC_2.[22] Copyright 2019, American Chemical Society. ...6

Figure 1-3. Illustration of typical preparing process of M_3X_2 MXene from M_3AX_2 precursor.[9] Copyright 2021, WILEY-VCH...8

Figure 1-4. Illustration of typical battery system.[63] Copyright 2020, Elsevier.....12

Figure 1-5. Scheme of basic structure in a Lithium-ion battery cell.[65] Copyright 2011, American Association for the Advancement of Science.....18

Figure 1-6. Scheme of working mechanism in DIBs.[104] Copyright 2017, American Chemical Society.....20

Figure 1-7. Scheme of PBAs during Zn^{2+} intercalation/deintercalation.[129] Copyright 2018, American Chemical Society. ...26

Figure 1-8. Illustration of projects in this thesis. ...30

Figure 2-1. Scheme of a) core-level photoelectron emission and b) energy level diagram of the XPS sample.[191] Copyright 2015, Springer-Verlag Berlin Heidelberg. ...34

Figure 2-2. XPS spectra of Ti 2p in $Ti_3C_2T_X$.[192] Copyright 2016, Elsevier. ...35

Figure 2-3. Scheme of X-ray diffraction.....36

Figure 2-4. XRD patterns of $Ti_3C_2T_x$ and Ti_3AlC_2.[194] Copyright 2017, WILEY-VCH.....37

Figure 2-5. Scheme of X-ray initial excitation (left), fluorescence emission (middle) and electron emission (right).[195] Copyright 2017, Royal Society of Chemistry.....38

Figure 2-6. a) Typical XAS spectrum divided with XANES and EXAFS regions.[195] Copyright 2017, Royal Society of Chemistry. b) Fe K-edge XANES spectrum of Fe foil, FeO and Fe_2O_3.[196] c) Full region and d) pre-edge region of Fe K-edge XANES spectrum of references.[197] Copyright 2019, Elsevier. ...40

Figure 2-7. a) N_2 adsorption-desorption isotherm plot and b) size-distribution of MR (MXene ribbons).[198] Copyright 2022, Elsevier. 42

Figure 2-8. Illustration of contact angle measurement results.[199] Copyright 2017, Elsevier. 43

Figure 2-9. GCD curves of Ti_2C at 0.1 C in LIBs half cell.[200] Copyright 2012, Elsevier.....45

Figure 2-10. a) Typical CV curves showing a reversible reaction with inset graph of the voltage change.[201] Copyright 2019, Wiley-VCH. b) CV curve of Ti_2CO_x *vs.* Li/Li^+ at scan rate of 0.2 mV s^{-1}.[200] Copyright 2012, Elsevier.....47

Figure 2-11. Plot of the peak current *vs.* scan rate.....48

Figure 2-12. Scheme of diagram for a) DC circuits and b) AC circuits.[202].....49

Figure 2-13. Model of equivalent circuit and EIS graph of a LIB half-cell system.[202].....50

Figure 2-14. EIS Nyquist plot and equivalent circuit of Randles cell model.[202] 51

Figure 3-1. SEM images of a) Ti_3AlC_2, b) $Ti_3C_2Cl_2$-0, c) $Ti_3C_2Cl_2$-33 and d) $Ti_3C_2Cl_2$-60. e) Corresponding EDS analysis of $Ti_3C_2Cl_2$-60. 60

Figure 3-2. a) X-Ray diffraction patterns of Ti_3AlC_2, $Ti_3C_2Cl_2$-0, $Ti_3C_2Cl_2$-33 and $Ti_3C_2Cl_2$-60. b) N_2 adsorption–desorption isotherms, c) pore size distribution of $Ti_3C_2Cl_2$-0, $Ti_3C_2Cl_2$-33 and $Ti_3C_2Cl_2$-60. d)-f) TEM images of $Ti_3C_2Cl_2$-0, $Ti_3C_2Cl_2$-33 and $Ti_3C_2Cl_2$-60.....63

Figure 3-3. a) TEM, b) STEM-HAADF and corresponding c) Ti, d) Cl, and e) C elemental mapping images of $Ti_3C_2Cl_2$-60.....63

Figure 3-4. a) Schematic illustration of in-plane porous $Ti_3C_2Cl_2$ synthesized by MAX and salt mixture. b) Phase diagram of $NaCl/ZnCl_2$. Specific data obtained from previous literature.[223] Blue and red line represent the reaction process of $Ti_3C_2Cl_2$-33 and $Ti_3C_2Cl_2$-60. c) XRD patterns of $Ti_3C_2Cl_2$-33 and $Ti_3C_2Cl_2$-60 before the HCl washing process.....66

Figure 3-5. a) Galvanostatic charge-discharge curves of $Ti_3C_2Cl_2$-0, $Ti_3C_2Cl_2$-33, $Ti_3C_2Cl_2$-60 and $Ti_3C_2T_X$ at 0.1 A g^{-1}. b) Cycling and Coulombic Efficiency results of $Ti_3C_2Cl_2$-60, $Ti_3C_2Cl_2$-0 at 0.1 A g^{-1}. c) *Ex-situ* xrd results of $Ti_3C_2Cl_2$-60 before and after cycling for 100 cycles at 0.1 A g^{-1}. d) Rate capability test of $Ti_3C_2Cl_2$-0, $Ti_3C_2Cl_2$-33 and $Ti_3C_2Cl_2$-60. e) CV curves at various scan rates from 0.5 to 10.0 mV s^{-1} of $Ti_3C_2Cl_2$-60. f), g) Calculation of b-values and capacitive contribution of $Ti_3C_2Cl_2$-60. h) Contribution ratio of the capacitive at different scan rates of $Ti_3C_2Cl_2$-60. i) Long term cycling result of $Ti_3C_2Cl_2$-0, $Ti_3C_2Cl_2$-33 and $Ti_3C_2Cl_2$-60. 69

Figure 3-6. a) GITT curves and b) calculated Li^+ diffusion coefficients in $Ti_3C_2Cl_2$-60 and $Ti_3C_2Cl_2$-0. c) EIS data of $Ti_3C_2Cl_2$-60, $Ti_3C_2Cl_2$-33 and $Ti_3C_2Cl_2$-0. 70

Figure 3-7. a), b) Ti 2p and Cl 2p XPS spectra of $Ti_3C_2Cl_2$-60. c) Ti 2p XPS spectra of $Ti_3C_2T_X$. d) F 1s XPS spectra of $Ti_3C_2T_X$. 72

Figure 3-8. XANES spectra of Ti *K*-edge for $Ti_3C_2T_X$, $Ti_3C_2Cl_2$-0 and $Ti_3C_2Cl_2$-60 compared to references including Ti foil, Ti_3C_2 and TiO_2. 75

Figure 3-9. a) Optimized geometries and b) projected density of states of $Ti_3C_2Cl_2$ (upper) and $Ti_3C_2T_X$ (bottom). c) Adsorption energy of energetically favorable sites and d) diffusion barrier profiles of Li ion hopping migration on the selected terminations of $Ti_3C_2Cl_2$ and $Ti_3C_2T_X$ surfaces. 77

Figure 3-10. a)-c) GCD curves, rate performance and long cycling data of $Ti_3C_2Cl_2$-60 based DIBs. 79

Figure 4-1. SEM image of porous $Ti_3C_2Cl_2$. 86

Figure 4-2. a) Scheme of CoHCF/M-1% synthesis process. b)-d) SEM images, e) XRD, f) N_2 adsorption–desorption isotherms and g) pore size distribution data of CoHCF/M-2%, CoHCF/M-1% and CoHCF. 87

Figure 4-3. N_2 adsorption–desorption isotherms and pore size distribution for porous MXene.[265] 89

Figure 4-4. a)-d) TEM, STEM and HR-TEM images of CoHCF/M-1%. e) $Co2p_{3/2}$ and f) Fe $2p_{3/2}$ XPS spectra of CoHCF and CoHCF/M-1%. 91

Figure 4-5. Ti 2p XPS spectra of a) CoHCF/M-1% and b) porous MXene.[265] 91

Figure 4-6. a) Normalized Co K-edge XANES spectra, b) Co K-edge EXAFS R-space spectra, c) normalized Fe K-edge XANES spectra, d) Fe K-edge EXAFS R-space spectra of CoHCF, CoHCF/M-1% and CoHCF/M-2%. 94

Figure 4-7. TGA plots of CoHCF, CoHCF/M-1%, CoHCF/M-2%. 96

Figure 4-8. a) Galvanostatic charge and discharge curves, c) rate capability and d) long term cycling performances at 2.0 A g^{-1} of CoHCF, CoHCF/M-1% and CoHCF/M-2%. b) GCD curves of CoHCF/M-1% at different rates. e) EIS plots of ZIBs using CoHCF, CoHCF/M-1% and CoHCF/M-2% as cathodes. 99

Figure 4-9. *Ex-situ* Co $2p_{3/2}$ XPS spectra of a) CoHCF/M-1%, c) CoHCF and Fe $2p_{3/2}$ XPS spectra of b) CoHCF/M-1%, d) CoHCF at the initial state, discharged to 0.7 V and recharged to 2.0 V vs. Zn/Zn^{2+}. e) Zn $2p_{3/2}$ XPS spectra of CoHCF (top) and CoHCF/M-1% (bottom) after cycling. f) *Ex-situ* XRD patterns of CoHCF/M-1% at selected cycling potentials. 102

Figure 4-10. *Ex-situ* XRD plots of CoHCF before and after cycling. 103

Figure 5-1. a) XRD patterns of Ti_2AlC, Ti_2CCl_2 and p-Ti_2CCl_2. SEM images of b) Ti_2AlC, c) Ti_2CCl_2 and d) p-Ti_2CCl_2. 111

Figure 5-2. TEM images of a) Ti_2CCl_2 and b) p-Ti_2CCl_2. c)-d) Ti 2p, Cl 2p XPS spectra of p-Ti_2CCl_2. e) Schematic illustration of p-Ti_2CCl_2//Zn and Ti_2CCl_2//Zn electrodes fabrication.....112

Figure 5-3. SEM images of a) bare Zn, b) Ti_2CCl_2//Zn and c) p-Ti_2CCl_2//Zn.....113

Figure 5-4. Contact angles of 2 M $ZnSO_4$ solution on a) bare Zn, b) Ti_2CCl_2//Zn and c) p-Ti_2CCl_2//Zn electrodes. 114

Figure 5-5. Galvanostatic cycling voltage profiles of bare Zn foil, Ti_2CCl_2//Zn and p-Ti_2CCl_2//Zn symmetric cells at a), b) the current density of 1 mA cm^{-2} with capacity limit of 1 mAh cm^{-2}, and c), d) the current density of 10 mA cm^{-2} with capacity limit of 5 mAh cm^{-2}. e), f) Cyclic voltammetry curves and enlarged profiles of bare Zn foil, Ti_2CCl_2//Zn and p-Ti_2CCl_2//Zn plating/stripping performance.....116

Figure 5-6. a) electrode impedance spectroscopies and b) rate performance of bare Zn foil, Ti_2CCl_2//Zn and p-Ti_2CCl_2//Zn. c) Voltage polarizations of p-Ti_2CCl_2//Zn versus other reported works. d) Long term cycling performance of p-Ti_2CCl_2//Zn at 1 mA cm^{-2} and 10 mA cm^{-2} for 2000 h.....118

Figure 5-7. Cross-sectional and top-view SEM images of a), c) p-Ti_2CCl_2//Zn electrode and b), d) bare Zn electrode after cycling. 121

Figure 5-8. XRD spectra of a) p-Ti_2CCl_2//Zn and b) bare Zn after different cycles at 10 mA cm^{-2}. c) Scheme of crystallographic planes of (0002), (**1010**) and (**1011**). d) Schematic illustration of Zn deposition and cycling on p-Ti_2CCl_2//Zn (top) and bare Zn (bottom).....122

Figure 5-9. SEM images of a)-c) p-Ti_2CCl_2//Zn and d)-f) bare Zn electrodes after 20, 40, 60 min Zn deposition. *In-situ* optical microscopy visualization of g) bare Zn and h) p-Ti_2CCl_2//Zn, with scale bar representing 50 μm. *Ex-situ* XRD spectra of i) bare Zn and j) p-Ti_2CCl_2//Zn. Electric field simulation of k) bare Zn and l) p-Ti_2CCl_2//Zn.....125

Figure 5-10. a) XRD and b) SEM results of Ti_2CT_X. c) Cycling results of Ti_2CT_X//Zn symmetric cells at 1 mA cm^{-2} and 10 mA cm^{-2}. SEM images of Ti_2CT_X//Zn after electrodeposition time of d) 20 min, e) 40 min and f) 1 h. 127

Figure 5-11. *Ex-situ* XRD results of Ti_2CT_X//Zn after electrodeposition time of 20 min, 40 min and 1 h. 128

Figure 5-12. a) GCD, b) rate capability, c) CV, d) EIS and e) cycling curves of full cells with bare Zn and p-Ti_2CCl_2//Zn as anodes and MnO_2 as cathode. 130

Figure 5-13. SEM image of p-Ti_2CCl_2//Zn after full cell test. 130

List of Tables

Table 1-1. Comparison of multivalent charge carrier ions[126, 127] 23

Table 3-1. MXene-based anodes in lithium-ion batteries 70

Table 3-2. Atomic composition of $Ti_3C_2Cl_2$-60 73

Table 3-3. Elements from the XPS spectra of $Ti_3C_2Cl_2$-60 73

Table 3-4. Elements from the XPS spectra of $Ti_3C_2T_X$ ($Ti_3C_2O_{0.1}F_{1.4}(OH)_{0.5}$) 74

Table 4-1. ICP results of CoHCF in composites 96

Table 4-2. Electrochemical performance comparison of CoHCF/MXene and other Prussian blue analogues ZIBs cathode reported in literature. 100

Table 5-1. Comparison of this work and previously reported Zn anode protection results 118

Table 5-2. XRD comparasion of p-Ti_2CCl_2//Zn and bare Zn after different cycles and electrodeposition times 122

Table 5-3. XRD information of Ti_2CT_X//Zn 128

List of Abbreviations

Abbreviations	Intended Word/Phrases
2 D	Two Dimensional
BET	Brunauer-Emmett-Teller
CA	Contact Angle
CNT	Carbon Nanotubes
CV	Cyclic Voltammetry
CVD	Chemical Vapor Deposition
DFT	Density Functional Theory
DIBs	Dual Ion Batteries
DMSO	Dimethyl Sulfoxide
EDS/EDX	Energy-dispersive X-ray Spectroscopy
EIS	Electrochemical Impedance Spectra
EXAFS	Extended X-ray Absorption Fine Structure
GCD	Galvanic Charge/Discharge
GITT	Galvanostatic Intermittent Titration Technique
GO	Graphene Oxide
HER	Hydrogen Evolution Reaction
LIBs	Lithium-ion Batteries
NMP	N-methyl-2-pyrrolidinone
PA	Polyamide

PAN	Polyacrylonitrile
PBAs	Prussian Blue Analogs
PEG	Poly(ethylene glycol)
PVA	Polyvinyl Alcohol
PVDF	Polyvinylidene Difluoride
SEM	Scanning Electron Microscopy
SAED	Select Area Electron Diffraction
TBAOH	Tetrabutylammonium Hydroxide
TEM	Transmission Electron Microscopy
TEY	Total Electron Yield
TFY	Total Fluorescence Yield
TGA	Thermogravimetric Analysis
XAS	X-ray Absorption Spectroscopy
XANES	X-ray Absorption Near Edge Structure
XRD	X-Ray Diffraction
XPS	X-ray Photoelectron Spectroscopy
ZIBs	Zinc Ion Batteries

Chapter 1 Introduction

1.1 MXene

1.1.1 Background

The history of MXene (transition metal carbides and nitrides) dates back to 2011, when Dr. Yury Gogotsi discovered the chemical Ti_3C_2 that started the explorations into these family of 2D materials.[1] MXene has a general formula of $M_{n+1}X_nT_x$ (n=1-4), where M is early transition metals, X stands for C and/or N, and T_x represents various terminations such as -O, -OH, -F and -Cl.[2] Their atomistic models are shown in **Figure 1-1**, in which n layers of X are covered by n+1 layers of M in the arrangement of $[MX]_nM$.[2, 3] MXene is mostly produced by selective etching of the A-elements (typically group 13 and 14 atoms) from a MAX phase with the formula $M_{n+1}AX_n$, which exhibits layered hexagonal structures with $P6_3/mmc$ space group, where the X atoms fill the center of octahedral sites, glued by pure A layers.[4] To date, over 150 MAX precursors has been reported, offering opportunities to develop and explore a wide range of applications for MXene.[3]

As a new category of two-dimensional (2D) material, MXene possess unique characteristics such as hydrophilicity, high conductivity, and good mechanical properties. For instance, the widely explored titanium carbide MXene ($Ti_3C_2T_x$) exhibits impressive electronic conductivity of around 10000 S cm^{-1} and remarkable Young's modulus of 0.33 ± 0.03 TPa when evaluated in single layer.[5] There are thousands of publications regarding MXene in diverse fields of energy storage, medicine, sensors, optoelectronics and tribology.[3, 6, 7] Particularly, extensive works have utilized MXene towards high performance supercapacitors, batteries, water treatment, hydrogen storage,

etc.[8] Despite the important developments, material science and technology integration for MXene are still at the beginning stage with enormous potentials to be unveiled.

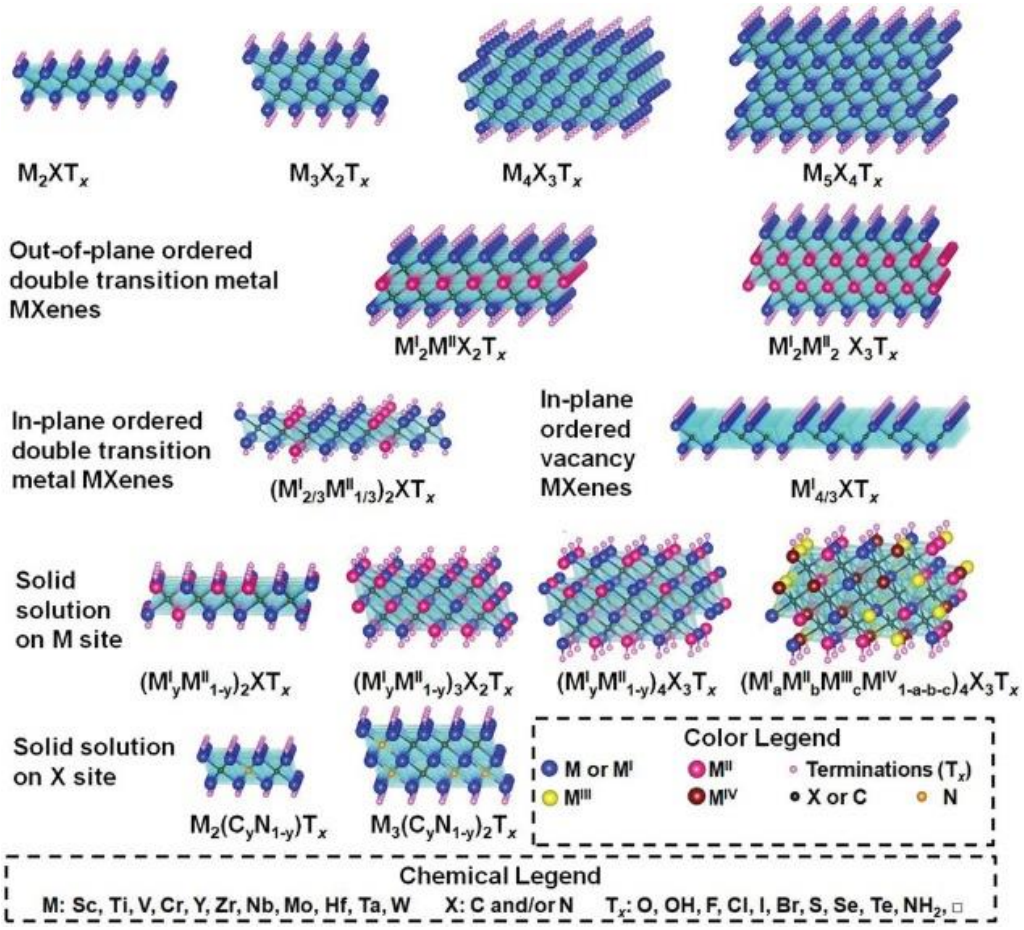


Figure 1-1. Typical structures and compositions of MXene.[3] Copyright 2021, WILEY-VCH.

1.1.2 Synthesis

The typical synthesis of MXenes from the MAX phases can be categorized as the top-down method, in which the M-A (metallic bonds) are more active than the covalent and ionic M-X bonds, enabling the chemical etching of A layers.[9] Conversely, some MXene can be prepared through bottom-up method of chemical vapor deposition (CVD). For example, ultrathin α-Mo_2C was

synthesized by CVD using methane as carbon source on Cu/Mo alloyed surface, their size, shape and thickness can be controlled via modifying the synthetic conditions.[10] Later, β-Mo_2C nanosheets were also successfully prepared using the same method.[11] Although the bottom-up strategies have benefits of growing MXenes with fewer defects and no terminations that are suitable for the intrinsic properties investigation, its high cost and harsh experiment requirement such as high temperature over 1000 ºC have limited their practical feasibility.[9, 12, 13]

For this thesis, the work focuses on the top-down approach as it is more prevalent and mature.[9] The method can be divided into the two steps of etching and delamination.

1.1.2.1 Etching

1.1.2.2 HF Etching

Hydrofluoric acid (HF) is the etchant used in the initial discovery of MXene, since then various MXenes have been developed using 10 to 50 wt.% HF with different etching durations under magnetic stirring.[1, 8] It should be noted that the addition of MAX powder should be divided into steps to lower the formation of bubbling caused by exothermic of the reaction. After the etching step, solids are washed several times to remove resultant acids. Finally, $Ti_3C_2T_x$ is separated from Ti_3AlC_2 by centrifugation.[14] Taking the widely studied $Ti_3C_2T_x$ as example, the etching reactions are shown as follows:[14]

$$Ti_3AlC_2(s) + 3HF(aq) \rightarrow AlF_3(aq) + \frac{3}{2}H_2(g) + Ti_3C_2(s) \quad (1\text{-}1)$$

$$Ti_3C_2(s) + 2H_2O(aq) \rightarrow Ti_3C_2(OH)_2(s) + H_2(g) \quad (1\text{-}2)$$

$$Ti_3C_2(s) + 2HF(aq) \rightarrow Ti_3C_2F_2(s) + H_2(g) \quad (1\text{-}3)$$

In this process, the Ti-Al bonds are cleaved by the HF, followed by reaction of the newly exposed Ti atoms with the abundant fluorine anions and hydroxyl groups in the solution to form -F, -O and -OH functional groups on the MXene surface.[15] Normally, MXenes consisting of more layers (higher n numbers) demand stronger etchant and longer reaction time.[2] The reaction conditions can also significantly influence the crystallinity, defect abundancy and surface properties of the resultant MXene,[9] providing room to finetune the MXene toward optimal property for the targeted applications.

1.1.2.3 Fluoride Salt Etching

Owing to the highly toxic and hazardous nature of HF, mixture of strong acid such as HCl and fluoride salt such as LiF, NaF and KF were developed as alternative etchant for MXene synthesis.[16] These milder synthetic approaches generate HF through reaction between the strong acid and the fluoride salt to avoid direct use of HF.[17] Below is an example of reaction between LiF and HCl.

$$LiF(aq) + HCl(aq) \rightarrow HF(aq) + LiCl(aq) \qquad (1\text{-}4)$$

Compared to the direct HF-etched MXene, MXenes prepared by fluoride salt etching exhibit fewer defects and larger lateral dimensions. The process is then further optimized by a process called Minimally Intensive Layer Delamination (MILD) that applies higher ratio of LiF and HCl ratio in the precursors.[18] The MILD method only requires manual shaking to produce large MXene monolayer flakes with few defects, whereas previous methods require sonication to shred the MXene flakes. Consequently, the MILD method can achieve higher exfoliation yield with around 70% flakes are one or two layers.

1.1.2.4 Electrochemical etching

Electrochemical etching is another approach to produce MXenes efficiently and safely from the MAX phases. For example, electro-oxidation using electrolytes consisting of 2 M HCl and 1 M NH_4Cl + 0.2 M tetramethylammonium hydroxide (TMAOH) has been reported to successfully synthesize Ti_2CT_x and $Ti_3C_2T_x$.[19, 20] The resultant $Ti_3C_2T_x$ can achieve large lateral size up to 18.6 μm, similar to the MXene prepared by MILD method.[20] However, excessive etching of the sample is a major challenge, as the MAX phase may be directly oxidized to carbon owing to dissolution of the "A" and "M" atoms, adding uncertainty and making the process difficult to control.[19]

1.1.2.5 Molten salt etching

More recently, molten salt etching has been reported as a green approach to synthesize MXene without the use of fluoride ions.[21] In 2019, the Huang group applied strong Lewis acidic molten salt $ZnCl_2$ to replace Al by Zn, synthesizing novel Zn-MAX precursors including Ti_3ZnC_2, Ti_2ZnN, Ti_2ZnC and V_2ZnC.[22] Subsequently, the excessive $ZnCl_2$ salt removes the Zn atoms and generated Cl-terminated MXenes such as $Ti_3C_2Cl_2$ (**Figure 1-2**). This method expands the list of available MAX phases for MXene synthesis, adding element such as Zn, Si and Ga to be the possible A-site elements.[21] Notably, the molten salt etching strategy also allows finer control of terminations on the MXenes surface, as uniform distribution of single termination such as -Cl, -Br and -Se can be achieved, which enables further investigations of their effect on MXene properties.[23]

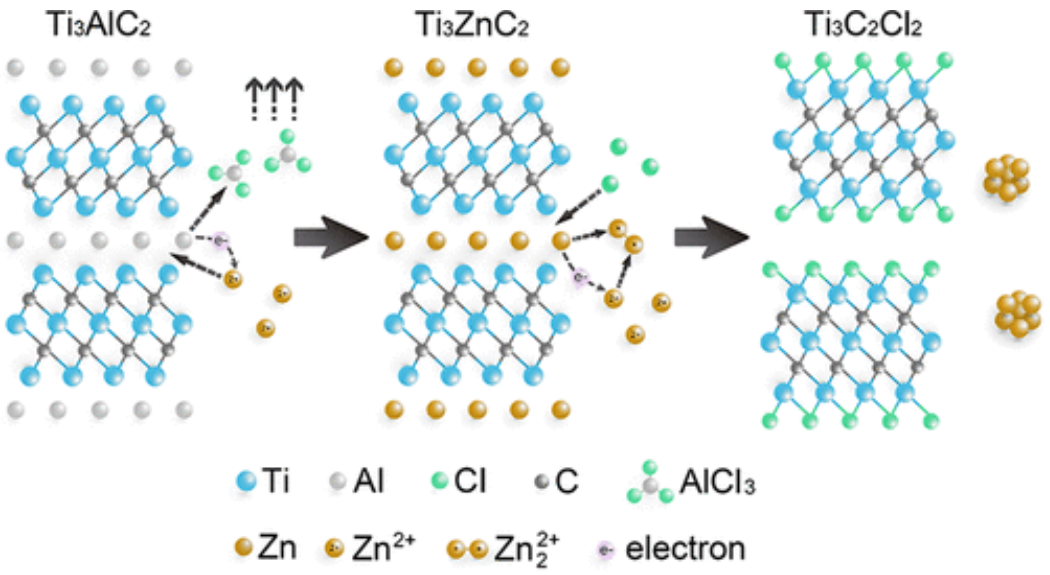


Figure 1-2. Scheme of molten salt etching of $Ti_3C_2Cl_2$ from Ti_3AlC_2.[22] Copyright 2019, American Chemical Society.

1.1.2.6 Delamination

After selective removal of the A-layers from the MAX phases, the resultant MXene flakes are held together by weak hydrogen bonds and/or van der Waals forces. In order to obtain single layer or few layers MXenes, further delamination or exfoliation are often required.[24] Organic solvents are one kind of commonly used intercalation agent to isolate multilayer MXenes. For example, dimethyl sulfoxide (DMSO) has been applied as intercalant for enlarging interlayer spacing of $Ti_3C_2T_x$ flakes prepared by HF. The flakes delaminated from sonication in DMSO are in the order of few hundred nanometers diameter.[25-27] However, DMSO residuals between the MXene layers are often difficult to be removed entirely due to their high boiling point.[28] Furthermore, other polar organic molecules including urea, hydrazine, tetrabutylammonium hydroxide (TBAOH) and iso-propylamine have also been applied to detach layers of etched

MXenes.[8, 29, 30] Additionally, alkaline ions such as Li^+, Na^+, K^+, Al^{3+} and NH_4^+ cations can also achieve delamination, due to negative charges on MXene.[31, 32] They paired particularly well with the fluoride salt etching method, as the cations can *in situ* delaminate the MXenes after the etching process without addition of extra molecules.[2] The resulting colloidal suspensions can maintain stable status after mild vibration, primarily due to the negative zeta potential of the MXenes sheets.[33]

To summarize, the synthesis route of MXene from MAX phases is illustrated in **Figure 1-3**. As shown, selective etching via fluoride-contained solution or Lewis acids molten salts is the first step to remove the A layers and generates multilayer MXene flakes. Compared to hazardous fluoride-contained compounds, Lewis acid etchants have the advantages of high safety and controllable terminations.[9] Subsequent delamination by metal cations or organic molecules separates the flakes from multilayer to few-layers, factors such as sonication time and strength in this step can significantly impact the size, defects and concentration of the resultant products. Particularly, high power sonication process with long sonication time will yield higher concentrated solution with smaller flakes and more defects.[18] It is important to note that MXenes produced through such methods are non-porous and have limited surface area, which restrict their applications. Given such, further research efforts are still required to develop feasible methods for synthesizing porous MXenes with high quantity and quality.

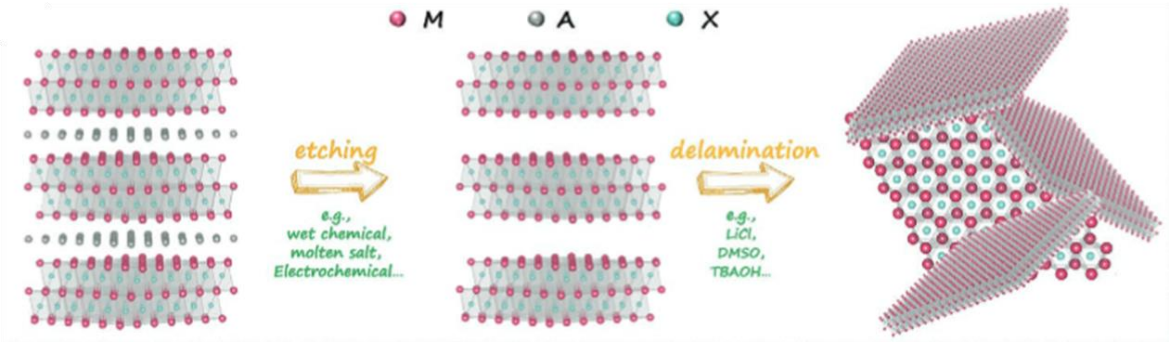


Figure 1-3. Illustration of typical preparing process of M_3X_2 MXene from M_3AX_2 precursor.[9] Copyright 2021, WILEY-VCH.

1.1.3 Properties

1.1.3.1 Surface Chemistry

As mentioned above, the synthetic methods can greatly influence the surface termination of the MXenes product. For instance, $Ti_3C_2T_x$ etched by HF has been reported to contain four times more -F terminations than samples produced via HCl/LiF.[34] The termination variances may influence the MXene crystal structure, as specific surface terminations such as -Cl and -Br were reported to enlarge the MXene interlayer spacing, which was attributed to adsorption of anion along the edges of MXene nanosheets.[35] Meanwhile, delamination conditions can also influence the type and ratio of termination on the final product. In one particular reporting, fluoride terminations of an exfoliating HF-etched MXene was observed to be replaced by hydroxyl group upon sonication in tetrabutylammonium hydroxide.[36] Additionally, post synthesis processing such as high temperature treatment and alkali hydroxide reaction can also alter the functionalities on the MXene surfaces.[37, 38]

1.1.3.2 Thermal Stability

Thermal stability of MXene sheet is highly dependent on its chemical composition and environment.[39] For example, the thermal stability of $Zr_3C_2T_x$ was reported to be better than Ti_3CT_x, as Zr_3C_2 structure is more energetically favored than ZrC, where Ti_3C_2 is metastable compared to bulk cubic TiC.[40] Meanwhile, different gas environment can also impact its stability, $Ti_3C_2T_x$ in particular has been identified to remains stable until 500 ºC in an Argon-filled environment, with its hexagonal structure preserved until 800 ºC.[41] While in an oxygen abundant atmosphere, $Ti_3C_2T_x$ is observed to be partially converted to anatase TiO_2 at 200 ºC and fully oxidized to rutile TiO_2 at 1000 ºC.[42] These conversion reactions can be manipulated by controlling other parameters such as heating rate and duration, providing opportunities to develop a varieties of MXene/TiO_2 composite for different applications.[43]

1.1.3.3 Mechanical and Physical Properties

Delaminated MXene flakes have outstanding mechanical flexibility, and can be folded into different shapes without visible damage.[44, 45] Previous study has reported an effective Young's modulus of 0.33 TPa for a freestanding monolayer $Ti_3C_2T_x$,[5] which is close to the predicted in-plane Young's modulus value of Ti_3C_2 single layer (502 GPa).[32] Additionally, the mechanical properties of MXene films can be tuned by intercalating polymers.[45] For instance, composite films of polyvinyl alcohol (PVA) intercalated $Ti_3C_2T_x$ displays improved mechanical characteristic, which can support 15000 times of their own weight (corresponding around 2.9 MPa stress). This work opens avenue for polymer/MXene composites for diverse applications.

Furthermore, its high electronic conductivity makes MXene promising candidate for electrode materials. In general, the electrical conductivity property of MXene heavily depends on the synthesis and delamination method. $Ti_3C_2T_x$ with large flake size and less defects produced by mild etching can obtain high conductivity up to 9880 S cm^{-1}, as there is coplanar alignment between individual flakes resulting in good contact.[46] In contrast, MXene etched by HF only possesses low conductivity of 850 S cm^{-1}.[47] When delaminated by large organic molecules such as DMSO, the resulted MXene show unsatisfied conductivity likely owing to the suppression of interflake electron doping.[48]

1.1.3.4 Electrochemical Properties

MXenes show privilege as host material in rechargeable batteries and hybrid supercapacitors.[49] Benefiting from abundant pseudocapacitive sites and wide interlayer spacing, MXenes can deliver high specific capacitance while maintaining its crystal structure through repeated volume expansion/contraction.[50] In one study, $Ti_3C_2T_x$ electrodes achieve specific capacitance of 450 F g^{-1} with outstanding rate performance in supercapacitor.[51] Moreover, delaminated Ti_3C_2 paper electrode is identified to exhibit outstanding Li storage capability of 410 mAh g^{-1} after 100 cycles in lithium-ion battery, which is close to its theoretical limit of 447.8 mAh g^{-1}.[29, 52] Though, further analysis reveal limited long period charge/discharge stability of 200 cycles at 1 C.[29] One of the major challenges of MXenes electrodes is the restacking issue, inhibiting electrolyte transport and decreasing the ion storage capability.[49] To resolve this problem, low dimensional molecules such as carbon nanotubes (CNTs), graphene and polymers have been incorporated with MXene nanosheets to serve as spacers and to provide additional

electrochemical capacity.[53-55] For example, sandwich-like $Ti_3C_2T_x$/CNTs paper has been fabricated by alternative filtration method with high volumetric capacitance of 390 F cm^{-3} and exceptional stability for over 10000 cycles.[45] Further modifications such as heteroatom doping and vacancies designing can also enhance the electrochemical performance.[8] Another major restriction is that conventional MXene lacks confined pores, which decreases the accessible sites on the surface.[56] One of the solutions is forming three dimensional networks by either self-assembling or hard templating, which not only enlarges the available surface area but also effectively inhibits restacking.[57, 58] Another strategy is post fabrication of in-plane porous MXene.[56] For instance, Cu^{2+} ions are found to partially oxidize MXene to TiO_2, forming mesopores after chemical etching.[59] However, these methods can only slightly increase the surface area, and inevitably complicate the process. A novel one-step synthesis of in-plane porous MXene to will be the primary of the discussion in this thesis.

1.2 Battery

1.2.1 Introduction

Climate change and air pollution concerns in recent decades have urged the transition toward renewable energy including solar and wind power,[60] but extensive integrations of the systems have been restricted by their inconsistency rooting from high dependence on local weather. These limitations place ever-increasing demands for economically viable and long lasting energy storage devices.[61] Moreover, wide spread societal adaption of electric vehicles (EV) and portable electronic devices also requires high performing energy storage system to extend their

capabilities.[62] As such, successful development of optimal energy storage systems are of great importance for continuing the advancement of modern society and quality of life.

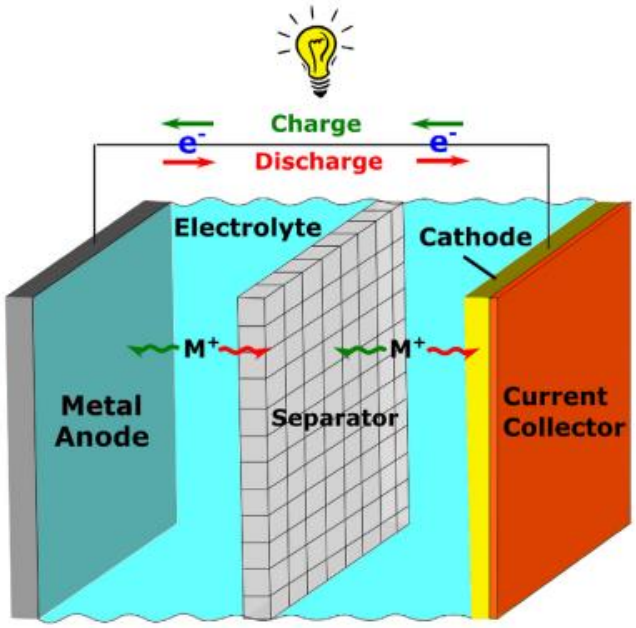


Figure 1-4. Illustration of typical battery system.[63] Copyright 2020, Elsevier.

As shown in **Figure 1-4**, a standard battery is constructed with the four main components of anode, cathode, electrolyte, and separator. The anode is responsible for storing the metal ions at a higher energy state, while the cathode provides a lower energy state for insertion of the metal ions.[63, 64] Energy levels of the anode and cathode are reflected in their redox potential, and their potential difference between the electrode materials provides the thermodynamic drive for the electrochemical reaction.[63] On the other hand, the electrolyte consisting of solvent and electrolyte salt enables diffusion of charge carrier between the two electrodes during operation. As for the separator, its primary purpose is to inhibit contact of the two electrodes to prevent short-circuiting without severely hindering the movement of ions.[65] It is often preferred for the electrolyte and

separator to not participate in the electrochemical reaction, though formation of solid electrolyte interphase (SEI) through their reaction is common, which has mix influences to the performance of the battery.[63] An ideal battery would be capable to store large amount of energy through fast charging and possesses long cycle life, which requires high energy density, high power density and good cycling stability. Moreover, low cost and high safety are also desired properties for batteries.[66]

Proper electrode materials selection and design are essential for high performance battery system.[63] In particular, redox potential and specific capacity of the electrode materials largely dictate the final energy density of the system. In terms of power density, which is particularly important for electric vehicles that calls for quick acceleration, superior reaction kinetic is desired for fast ion diffusion within the electrode matrix.[67] Meanwhile, long period cycling stability and structure resilience towards repeated reactions of the electrode materials are also important parameters that must be satisfied.

To this end, the benchmarks for superb electrodes for battery include:[68] 1) suitable redox reaction to provide high operating voltage; 2) unique architecture to improve capacity and rate capability; 3) robust structure to endure repeated charge/discharge process. Among various architectures, porosity design has been widely adopted as an effective way to maximize active material capacity utilization, enhance reaction rate and improve charge transfer by providing large surface area.[67, 69] Following are the detailed advantages of porous electrode materials.

1.2.2 Porosity in Battery Electrode Materials

Porosity is defined to be the proportion of void space in a solid, it is a critical parameter that can influence the surface area and permeability of materials.[69] According to International Union of Pure and Applied Chemistry (IUPAC) definition, material pores can be classified into three categories based on their sizes, which include the micropores under 2 nm in width, the mesopore that are between 2 to 50 nm, and the macropores with size beyond 50 nm. Generally, porosity can be incorporated into electrode materials by soft or hard templating, while some materials exhibit microporosity due to large tunnel sizes in their crystal structure.[70] In battery application, material porosity can heavily influence properties such as reaction kinetics and capacity utilization, porous carbons for instance are often adapted to improve the performance of electrode materials at high currents. Below are further discussions of battery properties that are affected by the presence of porosity in electrode materials.

1.2.2.1 Ion Diffusion

One obvious property that porosity influences is ion diffusion in the electrode material. As shown in equation 1-5, the characteristic diffusion time (τ) for active ions is proportional to the square of the effective diffusion length (l), where D is the ionic diffusion coefficient[70]:

$$\tau \sim \frac{l^2}{D} \qquad (1\text{-}5)$$

A porous material can effectively shorten the diffusion time through establishing a shorter diffusion length l for the ions, allowing rapid transportation of the active ions to the intercalation site. It should be noted that performance improvement through elevated ion diffused are most significant at high current application, while the increasement at low current is less significant as

kinetics limitation becomes less impactful.[71] Examples including porous TiO_2 have demonstrated drastically improved rate capability upon introduction of porosity to the electrode materials.[72, 73]

1.2.2.2 Internal Battery Resistance

In batteries, the relationship between battery power density (P) and current (I) is expressed as follows[74]:

$$P = VI \tag{1-6}$$

In which, the actual battery voltage (V) is related to the open-circuit voltage (V_{OC}) and the battery internal resistance (R_b) as shown below[74]:

$$V = V_{OC} - IR_b \tag{1-7}$$

While R_b is the sum of resistances in all battery component[69]:

$$R_b = R_{el} + R_C + R_A + R_{in(C)} + R_{in(A)} + R_{c(C)} + R_{c(A)} \tag{1-8}$$

Here, R_{el} represents the electrolyte resistance; R_C and R_A are the resistances of cathode and anode; $R_{in(C)}$ and $R_{in(A)}$ are the resistances of working ion to transport across the electrolyte-cathode and electrolyte-anode interfaces; and $R_{C(C)}$, $R_{C(A)}$ are the resistances of current collector of cathode and anode, respectively.

For the internal electrolyte resistance R_{el} in a theoretical model of cylindrical pores, R_{el} can be calculated by the following equation[75]:

$$R_{el} = \frac{\rho l}{3n\pi r^2} \tag{1-9}$$

Where ρ is the electrolyte resistivity, l is the depth of the pore, n and r are the number and radius of pores in the electrode. To achieve low R_{el}, large quantities of pore architecture with large radius (r) and short depth (l) are desired.

Meanwhile, the ion interfacial resistance $R_{in(C)}$ and $R_{in(A)}$ are proportional to the ratio of geometrical area (A) and interfacial area (A_{in}) of the electrode[74]:

$$R_{in} \sim \frac{A}{A_{in}} \tag{1-10}$$

Given that interfacial area between electrode and electrolyte in porous materials is considerably increased, its R_{in} can be decreased significantly as a result.[76]

Therefore, porosity design of electrode materials can greatly decrease the internal battery resistance R_b by providing unique structure and abundant electrode surface area, which permits a high power density for the device.[69]

1.2.2.3 Active Material Utilization

Bulk materials with no porosity often struggle with site accessibility of the active metal ions, which restricts complete utilization of intercalation site within the allowed voltage window. Porous nanomaterials with small feature sizes and high specific surface area can remarkably boost contact between electrolyte and electrode, minimizing unused intercalation site and thus increasing the utilization of available capacity.[77] As energy density is proportional to the specific capacity, this would drastically improve the energy storage capability of the electrode material.[76] However, it is crucial to note that excessive porosity would lead to low material density and available capacity, therefore balance must be maintained to achieve optimal electrode performance.

1.2.2.4 Suppressing Volume Changes

When alloy materials such as Al and Si are used as anode materials, severe volume change during charge and discharge will result in particle pulverization, interparticle contact loss and mechanical integrity degradation.[78] Proper pore engineering of such alloy electrodes can alleviate the stresses by providing room for volume expansion, prolonging cycling time of the batteries.[69]

Overall, incorporation of porous structure to electrode materials can provide benefits to the battery performance in terms of power density, energy density and cycling stability.[69] Along with high electronic conductivity and structural stability of MXene, it is anticipated that their successful combination would lead to electrode materials that exhibit various desirable properties for battery applications. The synthesis methods and impact of the intrinsic pores of MXene will be further studied in this thesis.

1.2.3 Lithium-Ion Battery

Lithium-ion batteries (LIBs) are regarded as the main energy storage technology of the 21st century since their market introduction in 1991 by Sony Corporation.[64, 79-82] A representative structure of LIBs is presented in **Figure 1-5**, which shows a LIBs assembled with the commercially adapted $LiMO_2$ (M stands for Fe, Mn, Co, *etc.*) cathode and graphite anode.[65]

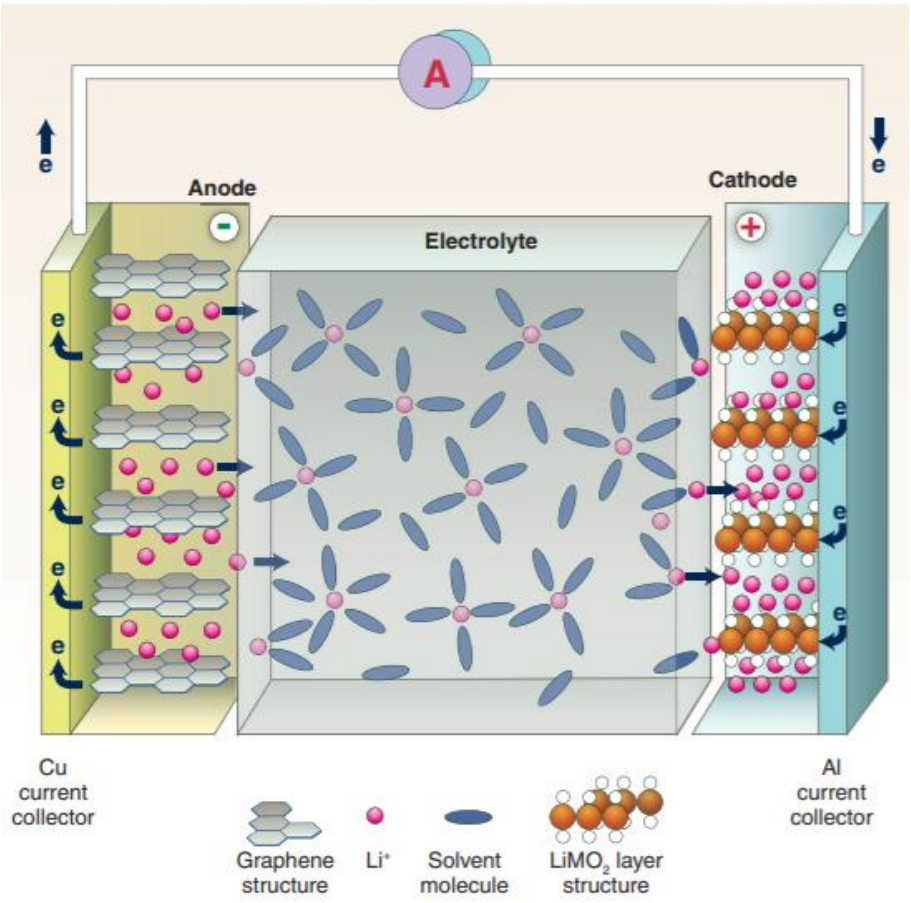


Figure 1-5. Scheme of basic structure in a Lithium-ion battery cell.[65] Copyright 2011, American Association for the Advancement of Science.

Taking the $LiCoO_2$/graphite cell as an example, the redox reactions are as follows,[83]

Cathode: $$LiCoO_2 \leftrightarrow Li_{(1-x)}CoO_2 + xLi^+ + xe^- \quad (1\text{-}11)$$

Anode: $$6C + xLi^+ + xe^- \leftrightarrow Li_xC_6 \quad (1\text{-}12)$$

Full reactions: $$LiCoO_2 + 6C \leftrightarrow Li_{(1-x)}CoO_2 + Li_xC_6 \quad (1\text{-}13)$$

As shown in the reaction equation and **Figure 1-5**, Li^+ ions are extracted from the graphitic anode and released into the electrolyte during discharge. At the same time, Li^+ ions are inserted

into the $LiCoO_2$ cathode, which keeps the electrolyte ion concentration consistent. These processes are paired with the transfer of electron from anode to cathode in the external circuit that maintains the charge balance. Vice versa, the Li^+ ions would return from $LiCoO_2$ to the graphite when the cell is charged.[83] Batteries in which the cations are the only ions actively shuttling between cathode and anode during the charge and discharge process are termed rocking-chair batteries, other well-known batteries that behave in this manner include sodium ion batteries and zinc ion batteries.[60]

At the current stage, LIBs remain the most widely applied electrochemical system owing to their relatively high energy density as well as mature technology. However, inherent safety concerns such as thermal runaway,[84-86] increasing raw material prices and supply shortages have encouraged the development of possible alternatives.[87-90] Particularly, systems towards 'beyond lithium' devices such as dual-ion, Zn^{2+}, K^+ and Na^+ batteries have been intensively investigated over the past decade.[91-99]

1.2.4 Dual Ion Battery

Among the alternative batteries, dual ion batteries (DIBs) possessing high working voltage have attracted considerable attentions.[87, 100-103] Unlike conventional LIBs with rocking-chair working mechanism, both the anions (A^-: PF_6^-, ClO_4^-, $TFSI^-$) and cations (M^+: Li^+, Na^+, K^+) participate in intercalation during the charge and discharge in DIBs.[104] As shown in **Figure 1-6**, typical DIBs called dual graphite battery (DGB) use graphite as both cathode and anode. Their working reactions are as follows[60, 100]:

Cathode: $C_{Cathode} + xA^- \leftrightarrow A_xC_{Cathode} + xe^-$ (1-14)

Anode: $C_{Anode} + xM^+ + xe^- \leftrightarrow M_xC_{Anode}$ (1-15)

Reaction: $C_{Anode} + xM^+ + xe^- + C_{Cathode} + xA^- \leftrightarrow M_xC_{Anode} + A_xC_{Cathode}$ (1-16)

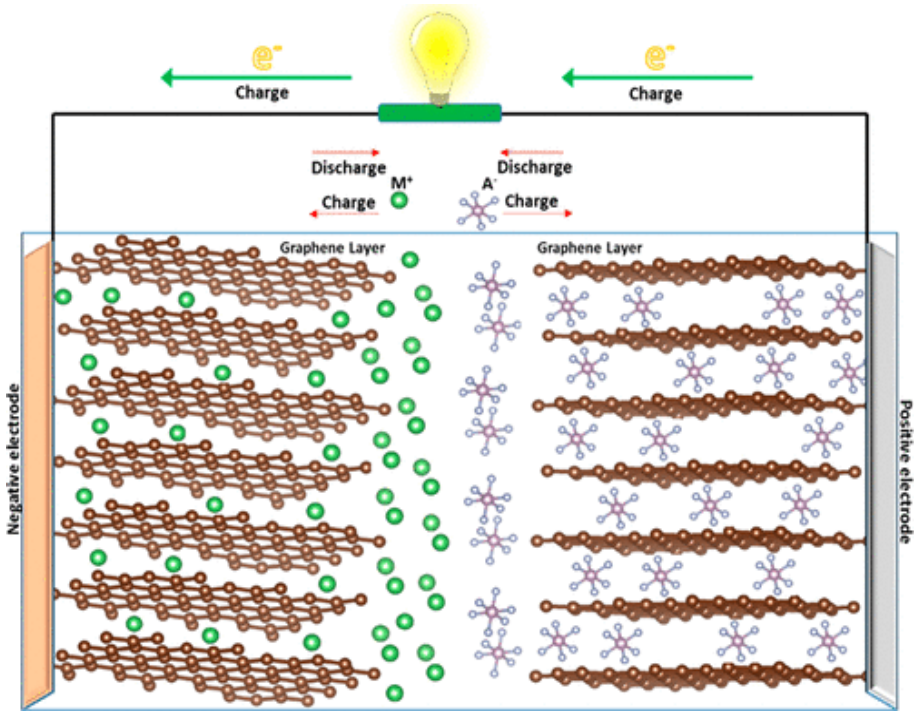


Figure 1-6. Scheme of working mechanism in DIBs.[104] Copyright 2017, American Chemical Society.

The primary specialty of DIBs is the behaviors of the anions during cycling, as they actively intercalate/de-intercalate from cathode during the charge/discharge process. Benefiting from this reaction, DGB has high discharge potential above 4.5 V *vs.* Li/Li$^+$, which is significantly higher than traditional LIBs. However, a direct result of activating the anion intercalation reaction is consumption of electrolyte ions that lowers the available charge carrier in the system, which can influence battery performance negatively.[61] To ensure sufficient ions availability, thickness of the separator/electrolyte layer in DIBs is often beyond 100 μm, which is thicker than 30-50 μm in

LIBs, lowering the overall battery energy density.[105] Given such, high ion concentrate and high voltage stability are both important properties for DIBs electrolyte.[61, 106]

1.2.4.1 Cathode

To reversibly host large size anions, layered structure cathode materials with large interstitial sites are generally preferred for DIBs. Graphite is the first reported anion host for DIBs application, its ABAB sequenced layer structure assembled by van der Waals forces is suitable for repeated anion intercalation, and it has the benefits of low cost and processing maturity.[104] For these graphite cathodes, morphology, particle size and surface area are properties that have high impacts on the performance, as graphite with smaller particle size and higher surface area have shown increased capacity and rate performance due to shorter diffusion distance. While large size graphite exhibits enhanced structural stability, but diffusion limitation severely hinders its reversible capacity.[107] To date, discharge capacities of graphitic cathodes studied for DIBs remains between 100 to 150 mAh g^{-1}, which are lower than commercial cathodes of LIBs.[60] Given so, there are strong interests in developing alternative cathode such as organic compound and metal-organic frameworks (MOFs), though specific capacity of these materials are still under 200 mAh g^{-1}, which requires further improvement to be competitive.[108, 109]

1.2.4.2 Anode

Albeit the cathode material being the significant bottleneck on cell performance of DIBs, the anode material should provide excess capacity to prevent metal plating that will endanger cell safety and lifetime.[110] One obvious anode material candidate for DIBs is the intercalation-type graphite commonly used in LIBs that shares the same working mechanism. Building on previous

LIBs works, carbonaceous materials such as microporous soft carbon nanosheets with high specific surface area was developed and achieved high reversibility of 93% capacity retention after 3500 cycles.[111] Heteroatom-doped carbon materials were also explored owing to their improved electronic conductivity and porous structure.[112] N-doped carbon fibers and P-doped hollow carbon rods with hierarchical structure in particular show enhanced ion transportation and effective suppression of volume expansion, which lead to stable operation up to 1500 cycles with 90% capacity retention.[112-114]

Despite the development, a major drawback for intercalation-type anode is their low capacity ceiling, which leave little room for further improvement in energy density.[112] To address this issue, alloying-type materials such as Al, Si, Sn and P have been heavily investigated as possible alternative with far higher theoretical capacity.[115] For example, Si that exhibits a theoretical capacity higher than 4000 $mAhg^{-1}$ is very attractive for anode application, but volume expansion of over 300% during cycling and deficient electrical conductivity of 10^{-5}-10^{-3} S cm^{-1} are their limitations.[116] Coating the Si particles with carbon is selected to reduce mechanical stress and increase electric conductivity.[117] As for the Al metal, it has a relatively high theoretical capacity of 993 mAh g^{-1}, and it can be applied directly as DIBs anode without current collector. However, volume fluctuation and pulverization during alloying/dealloying often cause capacity decay,[118] artificial protective layer and structural modification are strategies that show effectiveness alleviating this issue.[119, 120]

1.2.5 Zinc Ion Battery

Recently, multivalent-ion (Zn, Mg, Ca, Al, *etc.*) batteries have gained extensive research attention owing to their relatively low cost, environmental benignity and operational safety, their electrochemical properties are summarize in **Table 1-1**.[121-125] Among them, Zn^{2+} ion exhibits a suitable potential of –0.76 V vs SHE (standard hydrogen electrode) for aqueous system, relative small ionic radius (0.75 Å) and medium-high volumetric capacity of 5855 mAh cm^{-3}.[126] Importantly, zinc foil exhibits acceptable reversibility toward stripping/platting in aqueous condition and various cathode options with promising performance are available.[127]

Table 1-1. Comparison of multivalent charge carrier ions[128, 129]

Category	Zn^{2+}	Mg^{2+}	Ca^{2+}	Al^{3+}
Electrode potential vs SHE [V]	-0.76	-2.37	-2.87	-1.66
Ionic radius [Å]	0.75	0.72	1.00	0.53
Specific capacity [mAh g^{-1}]	820	2205	1337	2980
Capacity density [mAh cm^{-3}]	5855	3832	2072	8046

Zn battery application began in the 1860s when the first primary alkaline Zn battery was introduced into the market, and they remain a staple for common household electronic.[130] Its rechargeable version introduced in the 1980s did not achieve any meaningful market adaptation, as they often lose half of its initial capacity after twenty cycles of use.[131] To address the rechargeability issues, in 1986, Yamamoto *et al* promised the replacement of alkaline electrolyte with $ZnSO_4$ electrolytes, which fundamentally altered the electrochemical behavior.[132-136] The

mildly acidic system allows direct conversion between Zn^{2+} and Zn in the anode side, completely eliminating the electrochemically passive by-products such as ZnO formed in alkaline electrolyte, enabling remarkably enhanced cycling performance.[137] However, unsatisfactory intercalation capacity and cyclability due to strong electrostatic interactions between cathode materials and divalent Zn^{2+} ions remain a challenge to be overcome.[137]

1.2.5.1 Cathode

Upon discoveries of the mildly acidic ZIBs, a large varieties of cathode materials were investigated for suitability with the new system. To date, manganese oxides, vanadium oxides and Prussian blue analogues (PBAs) are three material groups that have received the most research attentions.[138-140]

MnO_2 has been extensively explored as ZIBs cathode materials owing to its low cost and relatively high operating voltage of 1.3-1.4 V.[137, 138] MnO_2 can form many different polymorphous including the α-, β-, γ-, ε-, δ-, λ- and R-phase, this is due to the fundamental unit MnO_6 octahedra can be linked by sharing corners and/or edges, allowing the formation of tunnel, chain or layered structure.[141] In ZIBs, MnO_2 cathode can react through three different mechanisms: Zn^{2+} insertion/extraction, H^+ conversion and combination of the two reactions.[129] In the early stages of development, manganese oxides often demonstrate poor cycling performance due to irreversible structural transformation and manganese dissolution in the cycling process.[130, 142-147] The dissolution issue can be suppressed by addition of $MnSO_4$ to the electrolyte, as studies have reported achieving over 5000 cycles of operation at specific condition with the modification.[148] In comparison to the manganese oxide cathode, most vanadium oxide cathodes

exhibit higher capacity and stability owing to their larger and more durable structure.[149-152] Nevertheless, the average discharge voltages of most V_2O_5-based cathodes are only ~0.75 V *vs.* Zn/Zn^{2+}, making it difficult to achieve high energy density ZIBs.[140, 153-155]

Lately, PBAs with advantages of inexpensiveness, non-toxicity and facile synthesis are also promising cathode candidates for both mono-valent cation[156-159] and multi-valent cation batteries.[123, 160-163] They are also called transition-metal hexa-cyanoferrates (MHCFs), with a general chemical formula of $MFe(CN)_6$ (M = Fe, Cu, Mo, Ni, Fe, V, Mn...) and face centered cubic structure in *Fm-3m* space group. The typical crystal structure of PBAs is shown in **Figure 1-7**, where Fe (III) and M metal ions are linked by cyanide (C≡N) ligands and the structure is established by FeC_6 octahedra and MN_6 octahedra.[164, 165] Owing to the distinctive crystal structure with sufficient large three-dimensional diffusion tunnels and interstitial sites for metal ions, PBAs have been reported to be ideal host material for multivalent cation transportation.[166] When used as cathode for ZIBs, PBAs can achieve average operating voltages higher than 1.5 V, which significantly exceed the majority of reported ZIBs cathodes.[167] There are two redox pairs in theory, the Fe^{2+}/Fe^{3+} and M^{2+}/M^{3+}, offering two moles of electron for transfer. However, inherent vacancies and lattice defects of $Fe(CN)_6$ formed during traditional production methods often hinder the complete use of active sites in PBAs. Meanwhile, various types of M give rise to different electrochemical performances of PBAs by altering the crystal structure.[165, 166]

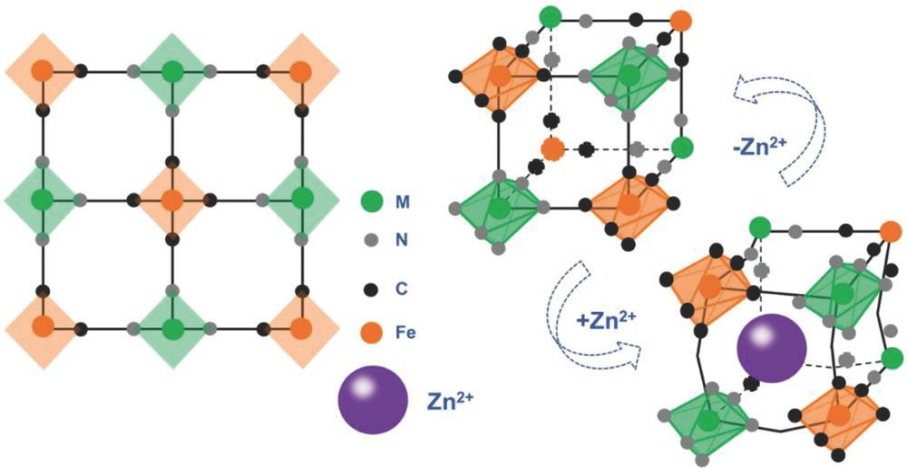


Figure 1-7. Scheme of PBAs during Zn^{2+} intercalation/deintercalation.[129] Copyright 2018, American Chemical Society.

In 2015, ZnHCF was first used as ZIB cathode materials and attained a high discharge voltage of 1.7 V.[167] The redox reactions of the cell are as shown below:

Cathode: $xZn^{2+} + 2xe^{-} + Zn_3[Fe(CN)_6]_2 \leftrightarrow Zn_{3+x}[Fe(CN)_6]_2$ (1-17)

Anode : $xZn \leftrightarrow xZn^{2+} + 2xe^{-}$ (1-18)

Reaction: $xZn + Zn_3[Fe(CN)_6]_2 \leftrightarrow Zn_{3+x}[Fe(CN)_6]_2$ (1-19)

Although its discharge capacity of 65.4 mAh g^{-1} is low, it still achieves a decent energy density of 100 Wh kg^{-1} because of the high operating voltage. Follow up study identified that the ZnHCF morphology can be controlled by changing the mixing period of the co-participation process, opening additional path for further optimizations.[168]

In addition to ZnHCF, other PBAs including CuHCF, FeHCF, MnHCF, CoHCF, NiHCF and multi-metal HCF such as CuZnHCF have also been applied as ZIBs cathodes.[169] Among them, the newly discovered CoHCF delivered high capacity of 173.4 mAh g^{-1} at 0.3 A g^{-1}, with

operational voltage of 1.75 V and excellent cycling stability of nearly 100% after 2200 cycles at 3.0 A g^{-1}.[170] The exceptional electrochemical result is achieved through double activation of Co^{2+}/Co^{3+} and Fe^{2+}/Fe^{3+} redox pairs, whereas other reported PBAs typically utilize the Fe redox only. As crystal vacancies in PBAs often occupy the intercalation sites of Zn^{2+}, it can trigger uncontrolled phase transformation during cycling. Further material modification focused on reducing the lattice defects in the crystal structures can improve the structural stability and redox utilization of PBAs.[171]

Aside for the above three types of materials, researchers have also investigated new families of cathode materials for ZIBs such as polyanionic compounds,[172] organic compounds,[173] and metal sulfides[174, 175]. These materials with Zn^{2+} hosting ability each have their own attractive features that are valuable as rechargeable ZIBs cathodes. For instances, polyanion materials with large channels can facilitate rapid cation intercalation/de-intercalation, organic cathodes exhibit extraordinary discharge capacity with outstanding cycling performance owing to their unique redox chemistry, and metal sulfides with layered structure such as MoS_2 and VS_2 can endure volume change during cycling, resulting in high capacity retention.[126, 137, 168, 176] The exploration of unconventional ZIBs cathodes is still at its starting stage and more suitable nanomaterials are to be discovered.

1.2.5.2 Anodes Protection

Zinc foil is commonly used directly as the anode for aqueous ZIBs, which involves zinc plating/striping reactions during charging/discharging process.[177] However, zinc dendrite formation is an inevitable obstacle for aqueous ZIBs using mild acidic electrolyte. On one hand,

corrosion and hydrogen evolution reaction (HER) can easily be promoted by the enlarged surface area of the dendrites. On the other hand, acute dendrites can puncture the separators and cause internal short-circuiting in the cells, directly causing failure of the battery.[178] To date, there are three main strategies to modify the zinc deposition behavior in the zinc-electrolyte interface and host-zinc interface, which are electrolyte modification, artificial protective layer design and host development.[179]

Electrolyte additives such as thiourea is found to suppress the electroplated zinc growth towards $(10\bar{1}0)$ and $(10\bar{1}1)$ directions, which are crystal planes that are widely reported to be responsible for zinc dendrites formation.[180] Moreover, highly concentrated electrolytes such as 1 M $Zn(TFSI)_2$/21 M LiTFSI were also utilized as ion-enriched electrolytes, which lead to uniform zinc deposition and the successful suppression of HER.[181] However, organic additives and electrolyte with high concentration often lower the electrolyte ionic conductivity, which would deteriorate battery performance due to slower ion transportation.[179]

As for artificial protectively layers, it can reduce zinc dendrite formation through either spatial shielding or multimode-guided ion homogeneous diffusion.[182, 183] The criteria for suitable interfacial layer include: 1) good wettability with electrolyte for low ion interface transfer resistance; 2) excellent mechanical property to accommodate volume change; 3) no chemical reactions with electrolyte.[179] For example, inorganic protective layer such as TiO_2 and $CaCO_3$ with low electrical conductivity and high dielectric constant were reported to successfully redistribute zinc ions and guide uniform electrolyte flux near the zinc surface by enriching Zn^{2+} within a limited range.[184, 185] Meanwhile, organic hydrophilic polymers membranes made with

polyamide (PA), poly(ethylene glycol) (PEG) or polyacrylonitrile (PAN) have also been utilized as nanofences with ion immobility effect and suppress the water splitting side reaction.[186] The artificial layers are normally prepared by doctor bade coating, atomic layer deposition, spin coating or *in situ* interface synthesis. It is believed that thickness is an important parameter to guide ion flow and lower diffusion resistance.[187]

As zinc often grow randomly on bare zinc foils rather than returning back to its initial position, host materials have been developed as structural network to regulate zinc growth.[179] For instance, conductive host such as three-dimensional carbon nanotube exhibits high surface area has been reported to mediate electric field distribution for uniform Zn deposition.[177] Meanwhile, zincophilic hosts including Cu and Sn also enable host-zinc surface with abundant nucleation sites and lowered zinc nucleation barrier.[188, 189] According to the density functional theory (DFT), Sn and Cu metals show higher adsorption affinity with Zn atom than carbon, which is favorable for zinc deposition over the surface. Other strategies including heteroatom or defect doping modifications on carbon materials are also expected to enhance their zincophilicity by changing it surface electronegativity and local dipole.[190]

1.3 Motivation and Thesis Structure

The objectives of this work are to: 1) develop a green-chemistry method to synthesize porous MXene; 2) evaluate the performance of porous MXene and its composites as battery electrodes and electrode supplement in different battery applications; 3) investigate the influence of MXene properties such as porosity and surface termination on its performance in different battery systems. **Figure 1-7** shows a breakdown of studies conducted in this thesis.

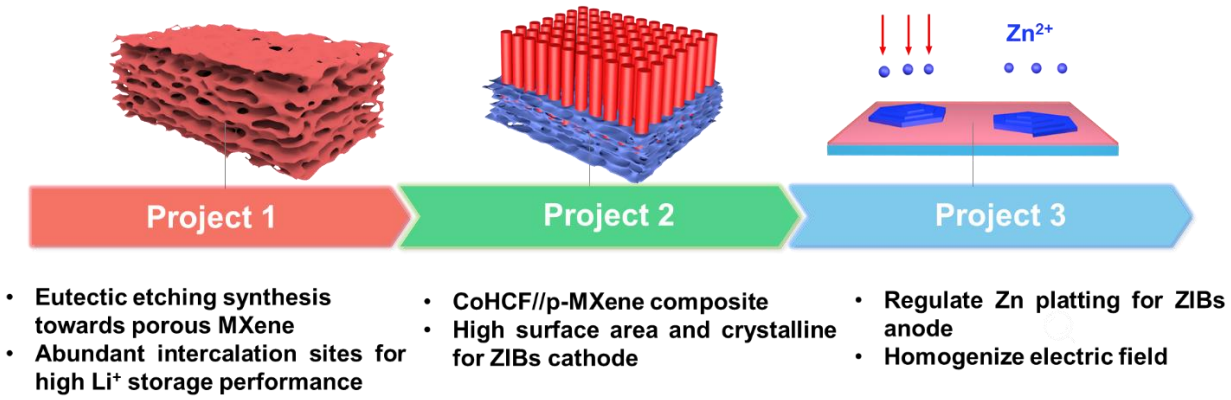


Figure 1-8. Illustration of projects in this thesis.

This thesis contains six chapters. **Chapter 1** introduces the basic properties, synthetic methods and research development of MXene. Background of different energy storage devices involving dual ion batteries and zinc ion batteries are also provided. This chapter ends with motivation and structure of this thesis. **Chapter 2** includes key characterization and experimental techniques employed in this thesis, with more detailed descriptions are provided in Chapter 3 to Chapter 5. **Chapter 3** presents work done on developing a feasible and non-toxic eutectic etching method to synthesize in-plane porous MXene. Electrochemical performance and behaviors of the porous MXene as dual ion battery anode materials are also discussed. **Chapter 4** focuses on the development of porous MXene/CoHCF composite for application as high performance zinc ion battery cathode. The functions of porous MXene during the CoHCF crystalline growth is investigated. **Chapter 5** highlights the utilization of porous MXene as protective layer for zinc anode, effect of the porous MXene in modulation of zinc deposition is elucidated. **Chapter 6** outlines the key conclusions and outlook on the basis of this thesis.

Chapter 2 Experimental Methods

2.1 Physical Characterization

2.1.1 Scanning Electron Microscopy

Scanning electron microscopy (SEM) is a widely used physical technique to image the morphology of the sample surface. The main advantage of adapting electrons for imaging is the drastically shorter wavelengths compared to visible light, providing SEM with high resolution down to around 10 nm. Generally, the instrument is constructed with an electron gun, multiple condenser/objectives lens as well as electron detectors in a high vacuum system. During operation, electrons are emitted from a heated filament and then accelerated by an electric field ranging between 5 to 20 kV, it is then focused onto the sample by the condenser and focusing lens. When the electron beam strikes the surface of the sample, it is either scattered or absorbed, generating signals including secondary electrons, characteristic X-ray, back scattering electron, *etc.* These signals are then collected by the detectors, which convert the signal into current that reflects the brightness in the final images.

In this thesis, SEM was utilized to examine the morphology of synthesized porous MXene and its composite. It was also used as post cycling characterization to examine the change of the sample before and after the cycling process.

2.1.2 Transmission Electron Microscopy

Similar to SEM, transmission electron microscopy (TEM) is a commonly adapted tool to probe structural information of samples. TEM employs electron beam accelerated by very high

voltages (50-300 kV) to strike through ultra-thin specimen. The number of electrons transmitted through the sample in each location are then converted to create the final image. Typically, TEM samples should be very thin with thickness less than 1 μm. For TEMs that apply very high voltage, higher resolution structural information such as lattice distance, defects and dislocations in the nanometer scale can be obtained.

In this thesis, TEM was primary applied as supplement for the SEM to verify the morphology of the samples. In specific case when high resolution TEM is applied, it was used to directly observed crystal structure of samples in nanoscale, especially in the interface regime of two materials in a composite.

2.1.3 Energy Dispersive X-ray Spectroscopy

Energy dispersive X-ray spectroscopy (EDX or EDS) is a characterization technique usually coupled with TEM or SEM system to identify and quantify the sample chemical composition. EDS collects the characteristic X-ray signals of electrons ejected from the sample after electron beam bombardment. When the atom is struck by the beam, an electron in the inner shell is ejected from its ground state. An electron at higher energy level would then drop into the vacancy left by the pristine electron, and emit X-ray in the process, which corresponds to the energy gap between two energy levels. As the energy of emitted X-ray is characteristic for different elements, EDS allows the analysis of the type, percentage and distribution of each element within a particular area of the specimen. In this project, the EDS techniques were employed to obtained elemental proportion and distribution information in MXene and its composites.

2.1.4 X-ray Photoelectron Spectroscopy

X-ray photoelectron spectroscopy (XPS) is another technique that allows surface elemental investigation of the sample. XPS functions by exposing x-ray beam with selected energy to sample surface and measuring the kinetic energy and quantity of the photoelectrons emission. As shown in **Figure 2-1**, the binding energy is calculated based on the following equation:

$$E_K = hv - E_B - \varphi \qquad (2\text{-}1)$$

where E_K is the photoelectron kinetic energy and E_B is the binding energy of an electron at a particular level, hv represents the incident photon energy and φ is the minimum energy to move the electron to infinity from the surface. This information is used to verify the binding energy of the escaped electrons, which are then compared with the binding energy reference to confirm the type and chemical states of elements in the sample. XPS peaks are identified as njl, where n is the principle quantum number, l represents the angular momentum quantum (l = 0,1,2,3 for s, p, d, f orbitals, respectively) and j stands for the spin angular momentum number which equals to l + s (s is ± ½). For example, XPS peaks for 3p will be separated to $3p_{1/2}$ and $3p_{3/2}$ peaks. Compared to EDS, XPS can provide specific chemical information on the surface chemical interactions and electronic states, shifting of the characteristic peaks can be used to identify changes in chemical and electronic states of the same element in different samples as well.

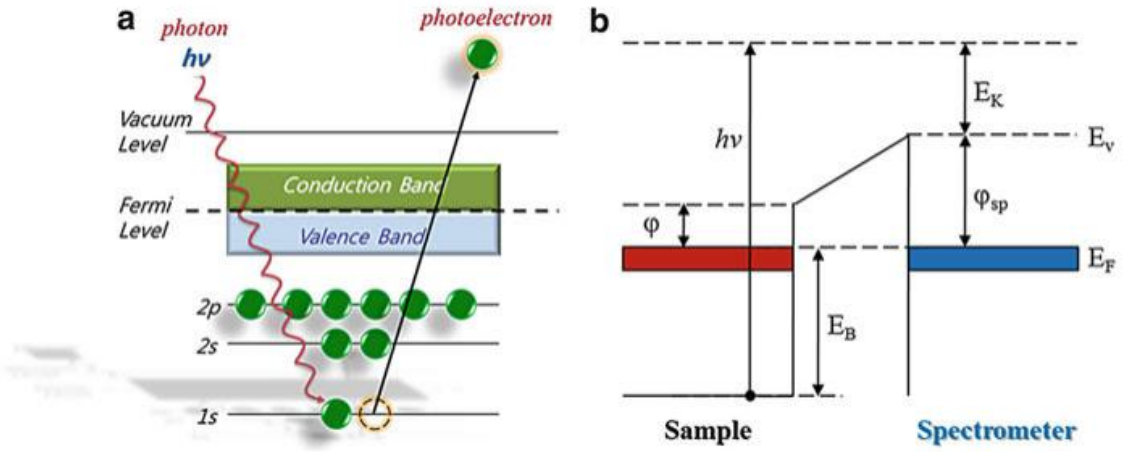


Figure 2-1. Scheme of a) core-level photoelectron emission and b) energy level diagram of the XPS sample.[191] Copyright 2015, Springer-Verlag Berlin Heidelberg.

In $Ti_3C_2T_X$, XPS spectra of Ti 2p is often detected to investigate the oxidation state of titanium element. The peaks are separated according to the oxidation states of titanium, where Ti $2p_{3/2}$ peaks locating at 457.2 eV, 455.8 eV, and 455.0 eV are ascribed to Ti^{+3}, Ti^{+2}, Ti^{+1}, respectively. Additionally, peaks set at 458.6 eV, 459.3 eV and 460.2 eV are assigned to TiO_2, $TiO_{2-x}F_{2x}$ and C-Ti-F. The existence of Ti-O bonds attributed to TiO_2 implies the partial oxidation of synthesized MXene.

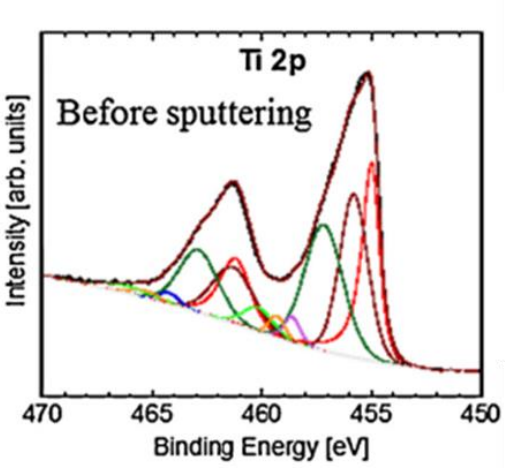


Figure 2-2. XPS spectra of Ti 2p in $Ti_3C_2T_X$.[192] Copyright 2016, Elsevier.

In this thesis, XPS analysis was used primary to detect the elemental states of the prepared chemicals. It was also used to study the changes of sample oxidation state in different phase of the battery cycling process.

2.1.5 X-ray Diffraction

X-ray diffraction (XRD) is a widely used non-destructive characterization method to characterize the crystal structure of the specimen. XRD is commonly employed to determine sample identity by comparing the results with JCPDS reference and obtain detailed information including grain sizes. It works primary by directing monochromatic X-rays beam to materials in varying angle and measuring the diffracted beam that returns. Its working mechanism is shown in **Figure 2-3**, two x-ray paths with same wavelength λ are diffracted off two adjacent lattice planes, and the distance between the two paths are illustrate by the dashed line. The relationship between the diffraction angle, X-ray and the crystal interlayer spacing in the lattice is described as Bragg's Law as shown below,

$$n\lambda = 2dsin\theta \qquad (2\text{-}2)$$

in which *n* represents integer, *d* stands for the lattice spacing and θ is the incident angle. When θ turns to a value that n results in a positive integer, a constructive interference occurs and generates a peak in the spectrum. The resulting XRD pattern over a range of angles can then be used to define the material identity and calculate the lattice spacing *d*.

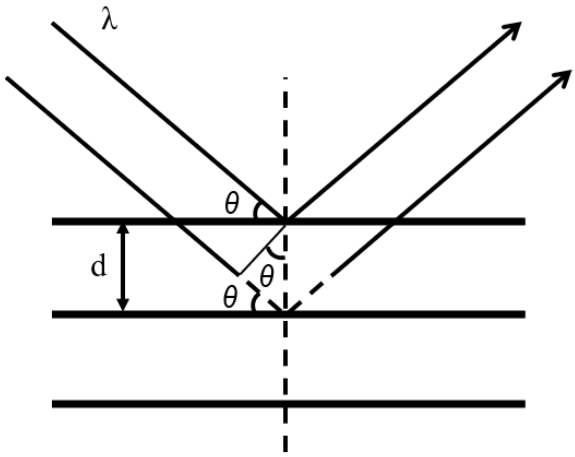


Figure 2-3. Scheme of X-ray diffraction.

As shown in **Figure 2-4**, the 2θ peaks located at 39˚ and 9.5˚ correspond the (104) and (002) peaks of Ti_3AlC_2.[193] After etching by HF, the disappearance of (104) peak and lower shift of (002) peak suggest the removal of Al layers and formation of $Ti_3C_2T_x$.[194] Moreover, the lowered (002) peak indicates the enlarged *d*-spacing of synthesized MXene compared to MAX phase, confirming the exfoliation of layered structure MXene.

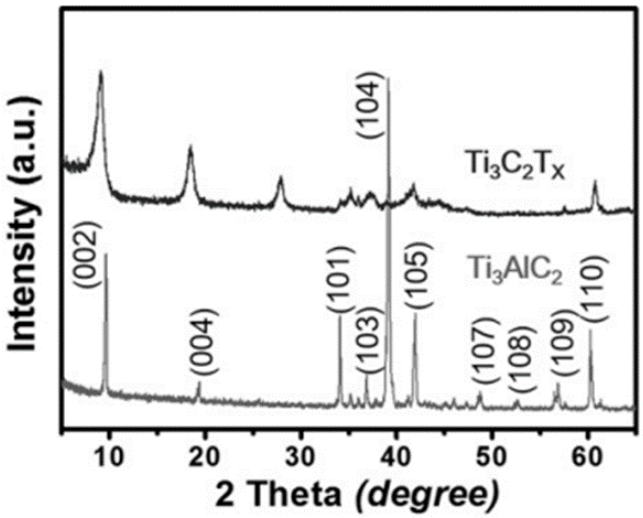


Figure 2-4. XRD patterns of $Ti_3C_2T_x$ and Ti_3AlC_2.[194] Copyright 2017, WILEY-VCH.

In this project, XRD technique was used to determine the structure and phase of MXene and its composite. It was also used for post-cycling characterization of the materials by comparing the spacing distance *d* in different charged/discharged states. Lastly, it was adapted to study occurrence of different zinc crystal plane to investigate the effectiveness of MXene as an anode protective layer for ZIBs.

2.1.6 X-ray Adsorption Spectroscopy

X-ray adsorption spectroscopy (XAS) is an advanced synchrotron radiation characterization suitable for studying the electronic structure, oxidation state and atomic structure information of sample elements. XAS spectrum is attained by detecting the absorption coefficient $\mu(E)$ over a photon energy region based on the absorption law:

$$\mu(E) = \ln\left(\frac{I_0}{I}\right) \qquad (2\text{-}3)$$

where I and I_0 are the transmitted and incident beams.

The mechanism is shown in **Figure 2-5**, the incident photon with specific energy excites the core electron to an unoccupied orbital (left), causing sharp absorption rise named absorption energy. This atom which is in the excited state with one hole will eventually decay to its "ground state". This decay mostly proceeds X-ray fluorescence (middle) and Auger effect (right). Measuring the emissions of fluorescence and the Auger electron are two methods to evaluate the absorption coefficient as they are both considered as proportional to the absorption coefficient.

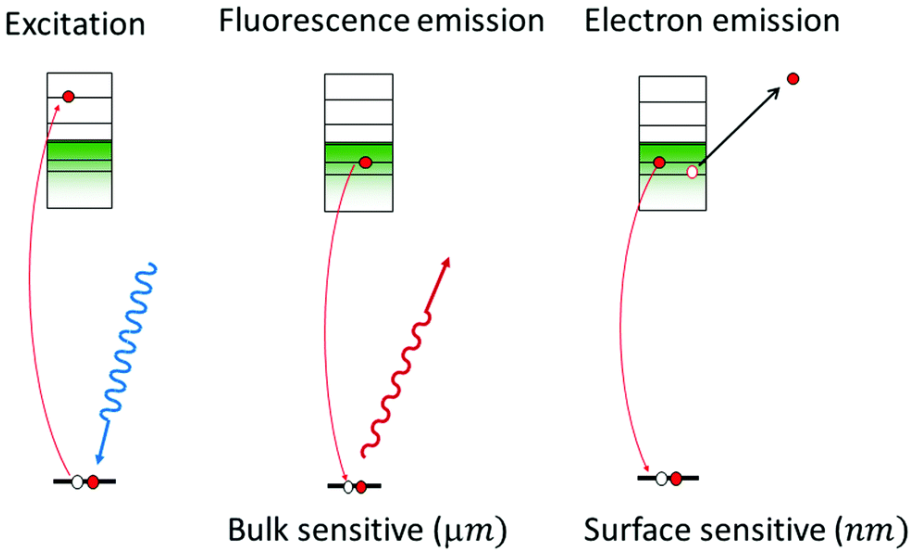


Figure 2-5. Scheme of X-ray initial excitation (left), fluorescence emission (middle) and electron emission (right).[195] Copyright 2017, Royal Society of Chemistry.

A typical XAS pattern can be split into two sections: extended X-ray absorption fine structures (EXAFS) and X-ray absorption near edge structure (XANES). As shown in **Figure 2-6a**, the large jump around 7130 eV is featured as absorption edge. The portion before and after absorption edge is referred as XANES, and the oscillations occurring at energies higher than

absorption edge are EXAFS region. The XANES section can be further divided into main-edge and edge-edge regions. The Fe K-edge XAS spectrum of Fe foil, FeO and Fe_2O_3 is shown in **Figure 2-6b**. The main-edge part consists of dipolar Fe $1s \rightarrow 4p$ states, whose energy is indicative of the oxidation state. Since the increase in the oxidation state lowers the screening amount of the nucleus that core electron will experience, more energy is required to excite the electron from the nucleus. Therefore, higher edge energy is detected for ion with more positive oxidation state. It is obvious that the absorption edge of FeO (Fe^{2+}) is shifted to lower energy compared to Fe_2O_3 (Fe^{3+}) owing to the lower oxidation state. The pre-edge part can further provide information regarding the coordination environment of transition metal center, such as coordination geometry and d-orbital occupancy. The intensity of pre-edge is highly dependent on the dipolar character. Since the inversion symmetry lost leads to the mix of *np* and *(n-1)d* states of transition metal, increasing the dipolar feature of the excitation, the intensity of pre-edge can probe the symmetry of transition metal in the compounds. For instance, there are two pre-edge peaks (7113.0 eV and 7114.5 eV) in the octahedrally coordinated Fe K-edge pattern of $FePO_4 \cdot H_2O$, arising from excitations to Fe 3d t_{2g} and e_g^* states (**Figure 2-6c,d**). It is obvious that the shape of pre-edge changes after removal of water, indicating the formation of new Fe 3d states in tetrahedrally coordinated Fe. Moreover, the strong and sharp pre-edge peak is because of the increased dipolar character of tetrahedral Fe in $FePO_4$. In general, XANES region is related to the local or atomic characteristic including coordination chemistry, orbital or band structure and oxidation states of the atoms.

EXAFS portion reveals the scattering information of the neighboring atom when the core electron is excited. Destructive and constructive interference photoelectron wave will occur when the scattering path involves the absorbing atom, resulting decreased or increased probability of

absorption. Normally, k-space patterns are plotted to reveal the oscillations intensity. Bonding information in atomic level such as coordination number in R-space pattern can be achieved through the Fourier transformation of k-space.

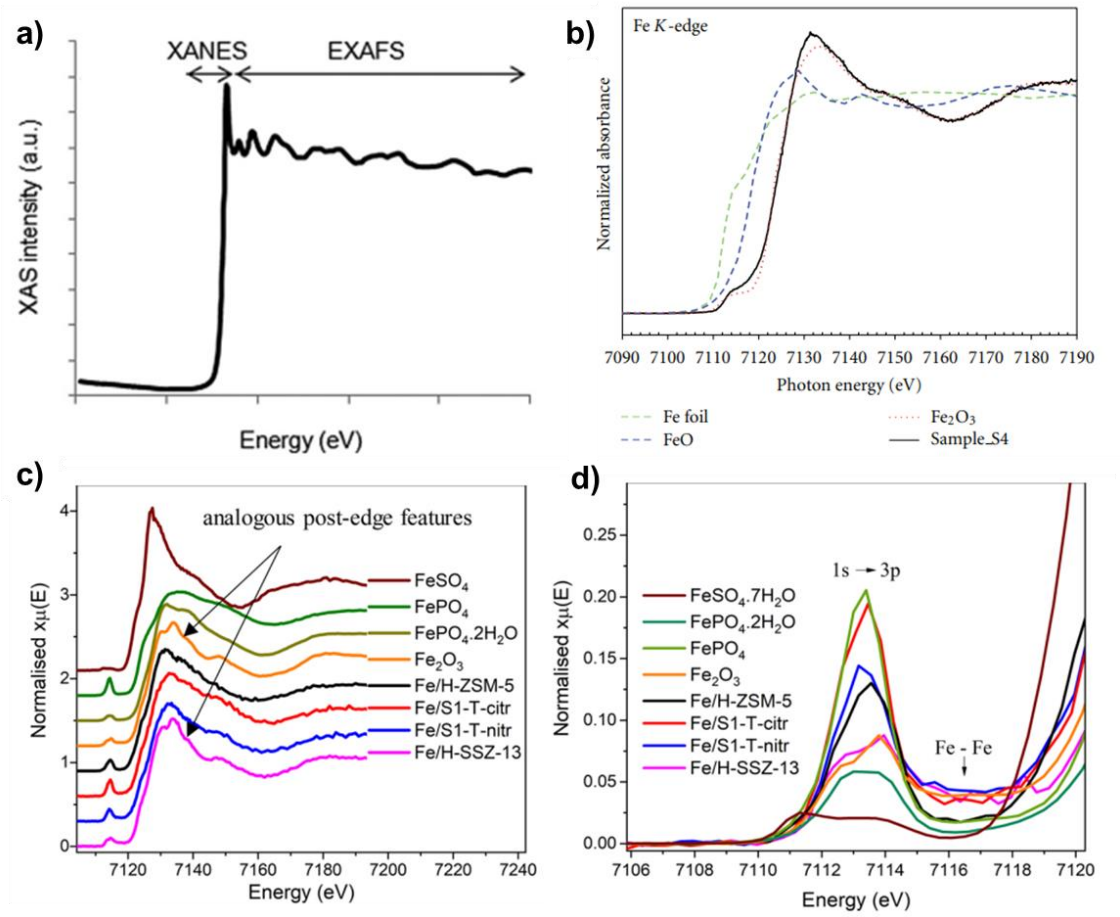


Figure 2-6. a) Typical XAS spectrum divided with XANES and EXAFS regions.[195] Copyright 2017, Royal Society of Chemistry. b) Fe K-edge XANES spectrum of Fe foil, FeO and Fe_2O_3.[196] c) Full region and d) pre-edge region of Fe K-edge XANES spectrum of references.[197] Copyright 2019, Elsevier.

In this work, XAS method was utilized to attain the oxidation state and structural information of Ti, Co and Fe in the porous MXene and its composites. By comparing the pre-edge and main-edge patterns of Ti K-edge in $Ti_3C_2Cl_2$ and $Ti_3C_2T_x$, the symmetry and oxidation degree of Ti atoms in two samples are compared. Moreover, Co and Fe R-space difference of CoHCF and CoHCF/MXene infer the existence of Co-C-Ti bond in the composite.

2.1.7 Thermogravimetric Analysis

Thermogravimetric analysis (TGA) is a widely used thermal analysis method to determine the composition information by measuring the weight loss of sample in a chamber with increasing of temperature. The samples are placed in a furnace in which the temperature is precisely controlled, and a high sensitivity balance allows precise measurement of material mass change in specific gas atmosphere. The project in Chapter 4 utilizes TGA in Ar atmosphere to determine the crystal water content within CoHCF and CoHCF/MXene composites, which is a widely used to investigate the vacancy information of PBAs.

2.1.8 Gas Adsorption Analysis

Gas adsorption analysis is the most common technology to quantify the specific surface area and obtain pore size distribution of porous samples. The method is based on the relationship between inert gas volume adsorbed on the sample surface and equilibrium pressure. The Langmuir theory can be used for monolayer adsorption condition, whereas the Brunauer-Emmett-Teller (BET) calculation is more universal with the assumption of multilayer adsorption condition. To start the gas adsorption analysis, the sample is first purified by a degas process in vacuum and a high temperature that is lower than the decomposition point of the material. Then the sample is

placed to interact with inert N_2 gas in a small tube is cooled down by liquid nitrogen. By measuring the pressure profile, the volume of adsorbed/desorbed gas is calculated. Finally, the software can analysis the specific surface area (SSA) and pore size.

BET specific surface area of MXene ribbons with width of 0.5 mm and 2 mm (denoted as MR-0.5 and MR-2) are shown in **Figure 2-7a**. The SSA of MR-2 is lower than that of MR-0.5, indicating lower ion-accessible surface when used as electrode material. Although they show similar mesoporosity concentrated at 3.8 nm, MR-0.5 possesses more pores with range of 4.2 – 18.3 nm, which permits facilitated electrolyte infiltration and ion transportation.

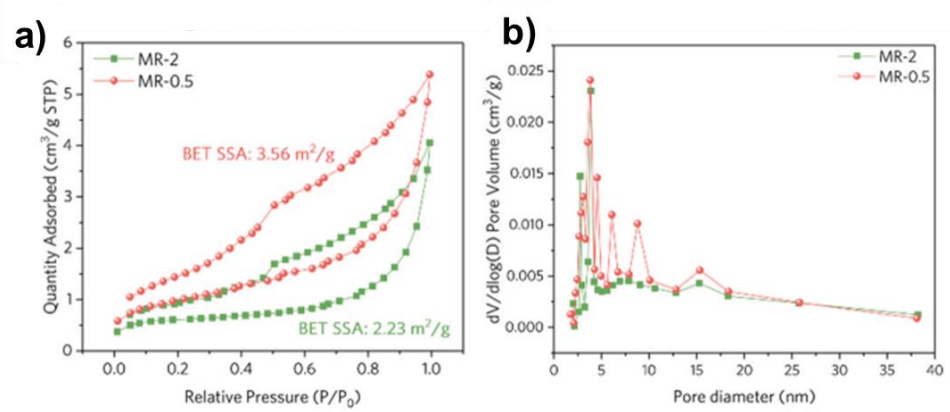


Figure 2-7. a) N_2 adsorption-desorption isotherm plot and b) size-distribution of MR (MXene ribbons).[198] Copyright 2022, Elsevier.

As this work is focused on the synthesis of MXene and its composites with porous structure, BET analysis was employed to evaluate the porosity of the prepared samples. Moreover, the results are combined with battery performance to investigate the relationship between porosity and electrochemical behavior of prepared nanomaterials.

2.1.9 Contact Angle

Contact angle (CA) measurement is a useful technique to characterize the wettability of the solid surface by measuring the angle between liquid-vapor interface and solid surface in the solid-liquid-vapor system (**Figure 2-7**). The contact angle θ is determined based on the Young-Dupree equation as follows:

$$\cos(\theta) = \frac{\gamma_{SV} - \gamma_{SL}}{\gamma_{LV}} \qquad (2\text{-}4)$$

where γ is the interfacial energy between two surfaces (S-solid, L-liquid and V-vapor). According to the Young equation, the solid surface with high surface-vapor interfacial tension tends to exhibit low contact angle, revealing good wettability. In Chapter 5, the contact angles between the electrolyte and various zinc anodes were compared to study the hydrophilicity change induced by surface modification.

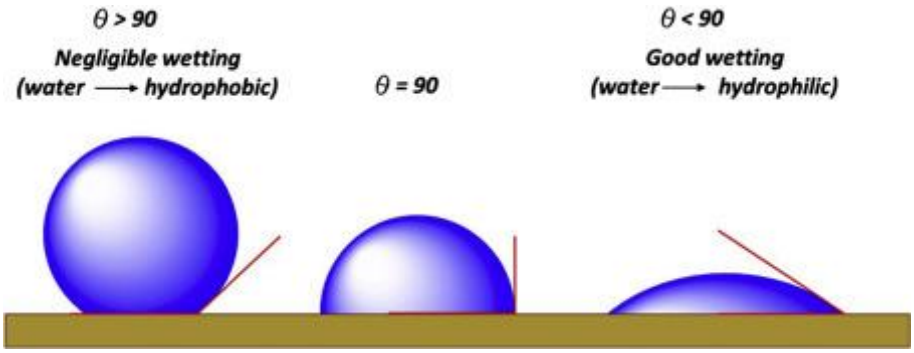


Figure 2-8. Illustration of contact angle measurement results.[199] Copyright 2017, Elsevier.

2.2 Electrochemical Characterization

Various electrochemical characterizations are applied in this project to investigate the energy storage performance of the synthesized electrode materials. Specific power and energy density, cycling stability can be measured by detecting the current and potential of the devices in various measurements. In this work, two types of cells are adopted for the investigation, one is the half-cell, where the targeted material is tested against a standard counter electrode such as lithium or zinc foil. The other is full cell, where the targeted material is tested against common electrode material used in commercial applications. High voltage window of 2.0-5.0 V vs. Li/Li^+ is selected for dual-ion battery full cell, using stable electrolyte of 4 M $LiPF_4$/EMC. Aqueous electrolyte of 15 M $ZnCl_2$ is chosen for CoHCF and its composite for higher capacity in zinc ion battery.

2.2.1 Galvanostatic Charge Discharge

Galvanostatic charge discharge (GCD) characterization tests electrochemical cells by applying a constant current while measuring the cell potential within a specific range of voltage. The test identifies voltages of the redox reaction plateaus and the practical capacity of the electrode materials. The specific capacity C $(mAh\ g^{-1})$ is calculated based on the following formula:

$$C = \frac{I\Delta t}{3.6\ m} \qquad (2\text{-}5)$$

where I (A) represents the constant current, Δt (s) is the time and m (g) is the mass of the active material. The specific current used for this analysis is called the C-rate, which is determined as the time required to fully discharge an electrode material based on its theoretical capacity. When fabricating full cell, the mass loading of two electrodes is determined by the balancing equation:

$$\frac{m_+}{m_-} = \frac{C_-}{C_+} \quad (2\text{-}6)$$

where C is the specific capacity of active material measured in half cell.

Figure 2-9 show the GCD curves of Ti_2CO_x at 0.1 C in a half cell. The capacity loss is mainly attributed to the solid electrolyte interface (SEI) formation at MXene/electrolyte surface and electrolyte decomposition in the first cycle. The SEI is known to be formed by reduction of electrolytes (salt, solvent and additives), which results in a passivation layer on the anode surface. Continuous growth of SEI would consume cations and cause irreversible capacity loss in the initial cycles. In the case of Ti_2CO_x, the discharge capacity stabilizes at around 160 mAh g^{-1} after five cycles, corresponding to $y \approx 0.75$ in the following redox reaction:

$$Ti_2CO_x + yLi^+ + ye^- \leftrightarrow Ti_2CO_xLi_y \quad (2\text{-}7)$$

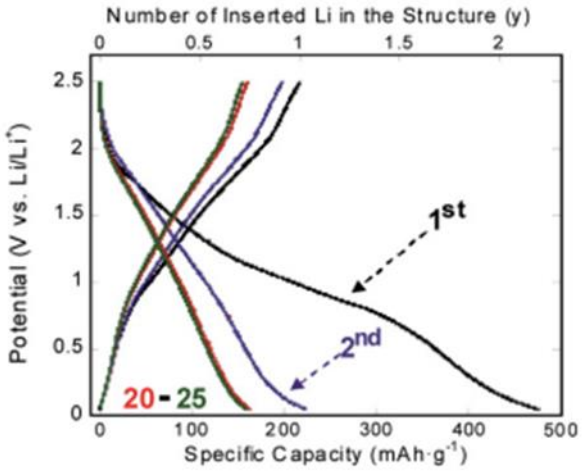


Figure 2-9. GCD curves of Ti_2C at 0.1 C in LIBs half cell.[200] Copyright 2012, Elsevier.

In addition to determining the voltage and capacity, GCD data can also determine other battery parameter such as Columbic Efficiency (CE), which is the ratio between charge and discharge capacity. Moreover, battery life cycles and durability can also be determined by

prolonged cycling of the GCD analysis. In this thesis, GCD tests were performed on LAND-CT2001A battery tester to assess the electrochemical performance of fabricated dual ion batteries and zinc ion batteries.

2.2.2 Galvanostatic Intermittent Titration Technique

Galvanostatic intermittent titration technique (GITT) is applied by evenly dividing the GCD process into small pulses with relaxation time. This analysis method enables investigation of reaction mechanism and kinetics during the charge/discharge process. Diffusion coefficient of the active ion in the electrodes can be calculated based on the GITT result. In this thesis, the diffusion coefficients of Li^+ transportation in non-porous and porous MXenes are compared in Chapter 3.

2.2.3 Cyclic Voltammetry

Cyclic voltammetry (CV) technique is utilized to study the redox reactions of electrode materials. The measurement is accomplished by linearly sweeping the working electrode voltage under a designated scan rate in a fixed voltage window. The cyclic voltammetry curve is plotted by recording the current change under different voltage. By analyzing the CV curve shape, location and intensity of peaks, the redox behavior of the samples can be compared.

Figure 2-8a is a CV plot for a reversible reaction:

$$O + ne^- \leftrightarrow R \qquad (2\text{-}8)$$

where O and R are oxidized and reduced species, respectively. Under a specific scan rate of v, the linearly swept potential is applied to the electrode, and the current response is as result of the redox reaction at the interface of electrode/electrolyte. The cathodic scan normally begins from OCV (open circuit voltage), which is higher than the reduction voltage and thus merely generating

capacitive current. The reduction starts when the voltage reaches reduction potential, which consumes O at the electrode surface. Therefore, there is a concentration gradient between the bulk solution and electrode surface. The cathodic current is formed by diffusion flux, which is proportionate to the concentration gradient. When the voltage is more negative, the flux increases as the surface O concentration decreases. The flux reaches highest if the surface O is exhausted, resulting cathodic peak potential ($E_{p,c}$) and current ($i_{p,c}$). Similarly, the oxidation potential ($E_{p,a}$) and anodic peak current ($i_{p,a}$) are obtained during the anodic scan.

Cyclic voltammetry curves of Ti_2CO_x at 0.2 mV s^{-1} are shown in **Figure 2-8b**. In the first lithiation cycle, irreversible peak around 0.6 V is observed, which disappears in the following cycles due to the formation of SEI, corresponding to the capacity loss in **Figure 2-7**. Broad reversible peaks located at 1.6 V and 2.0 V in the subsequent cycles matches the redox reaction (2-7).

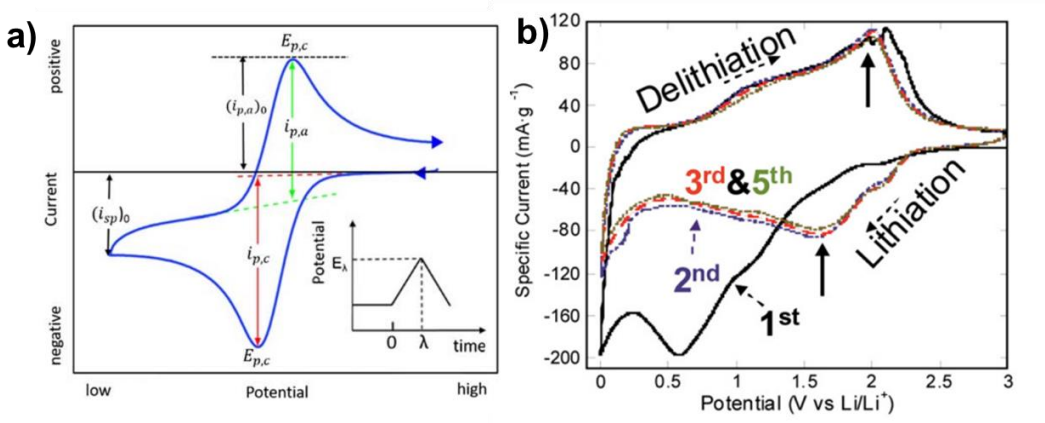


Figure 2-10. a) Typical CV curves showing a reversible reaction with inset graph of the voltage change.[201] Copyright 2019, Wiley-VCH. b) CV curve of Ti_2CO_x *vs.* Li/Li^+ at scan rate of 0.2 mV s^{-1}.[200] Copyright 2012, Elsevier.

Furthermore, the reaction kinetic of cation in the system can be evaluated by using the relationship between peak current (i) and scan rate (v) using on the following equation:

$$i = av^b \qquad (2\text{-}9)$$

where a and b are constant numbers. By plotting the data of log i *vs.* log v (**Figure 2-9**), the value of b can be calculated:

$$\log i = \log a + b \log v \qquad (2\text{-}10)$$

$$b = \frac{\log i - \log a}{\log v} \qquad (0.5 < b < 1) \qquad (2\text{-}11)$$

b value is the sum of electrochemical reactions consisted of diffusion and capacitive process. If b equals to 0.5, the reaction is a diffusion-controlled process. If b is 1, the process exhibits capacitive behavior.

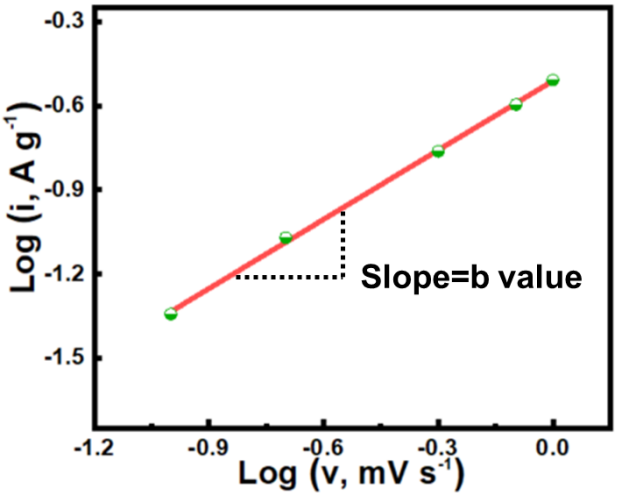


Figure 2-11. Plot of the peak current *vs.* scan rate.

In this thesis, CV analysis was applied to identify the redox potential of MXene and as fabricated zinc ion batteries, as well as to evaluate the diffusion-controlled behaviors of porous MXene when used as anode for dual-ion batteries.

2.2.4 Electrochemical Impedance Spectroscopy

Electrochemical impedance spectroscopy (EIS) is a useful method used to probe the dielectric property of the material. This measurement records the current response of the system to the AC voltage, providing the system impedance over a range of frequency (normally 10 mHz~100 kHz). As shown in **Figure 2-10a**, the relationship of resistance R and voltage V and current I follows Ohm's law when DC voltage is employed. Similarly, when AC voltage is applied to a cell, the impedance $Z(\omega)$ can be expressed by the following equation:

$$Z(\omega) = \frac{V(\omega)}{I(\omega)} \qquad (2\text{-}12)$$

where ω is the angular frequency of the AC voltage.

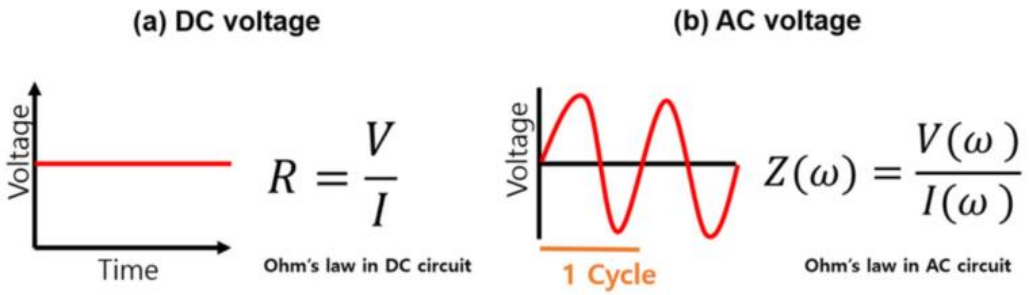


Figure 2-12. Scheme of diagram for a) DC circuits and b) AC circuits.[202]

The impedance can then be analyzed in a Nyquist plot, which compares the real segment *vs.* inverse imaginary segment of the impedance. Modeling of the result with circuit elements can be

further performed combining resistors (R) and capacitors (C) to determine impedance of composition in the cell. In the case of LIBs, CPE (constant phase element) and W (Warburg impedance) are added to complement non-ideal capacitor and lithium diffusion character. As illustrated in **Figure 2-11**, the equivalent circuit can be simplified with following components:

R_b represents bulk resistance of the cell including separator, electrolyte and electrodes;

CPE_{SEI} and **R_{SEI}** are the capacitance and resistance of interfacial layer;

$CPE_{electrode}$ and **R_{ct}** are double-layer capacitance and charge-transfer resistance;

W (Warburg impedance/resistance) demonstrates the diffusional effects of Li^+ on the host material.

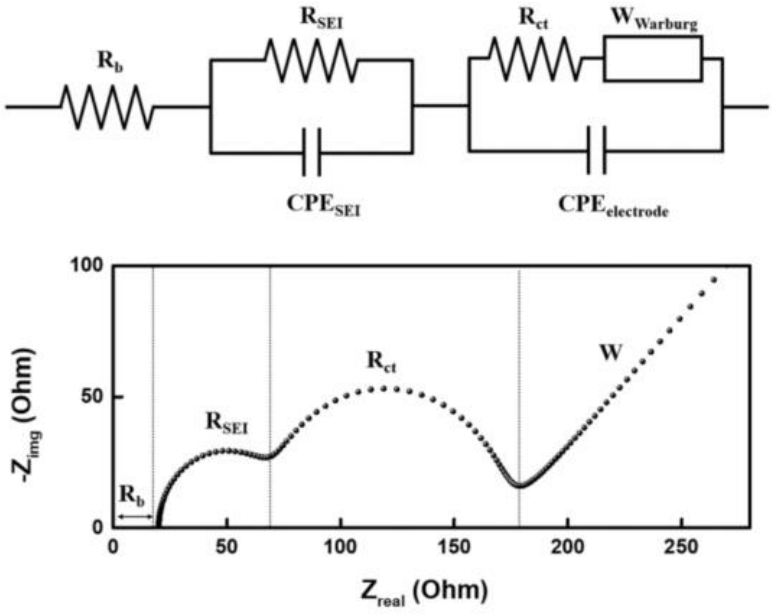


Figure 2-13. Model of equivalent circuit and EIS graph of a LIB half-cell system.[202]

When SEI layer is absent or dissolved/destroyed, Nyquist EIS spectra of the cell consists of a low frequency tail and high frequency semicircle, whose equivalent circuit is Randles-type (**Figure 2-14**). In this case, bulk resistance is the initial x-axis intercept value (R_b = 20 Ω), charge-transfer resistance is the diameter of the semicircle (R_{ct} = 100 Ω). The value R_{ct} can be used to evaluate the electronic resistance and reaction kinetics. Moreover, Warburg impedance follows the relationship of:

$$W = \sigma\omega^{-1/2} - j\sigma\omega^{-1/2} \qquad (2\text{-}13)$$

where σ is Warburg coefficient. As the straight line in **Figure 2-14** appears 45˚ slope, the Warburg coefficient σ is 1 Ω $s^{-1/2}$. When comparing different cells, the increased slope of straight line in Nyquist plots indicates the facilitated ion diffusion and capacitive behavior of the electrode.

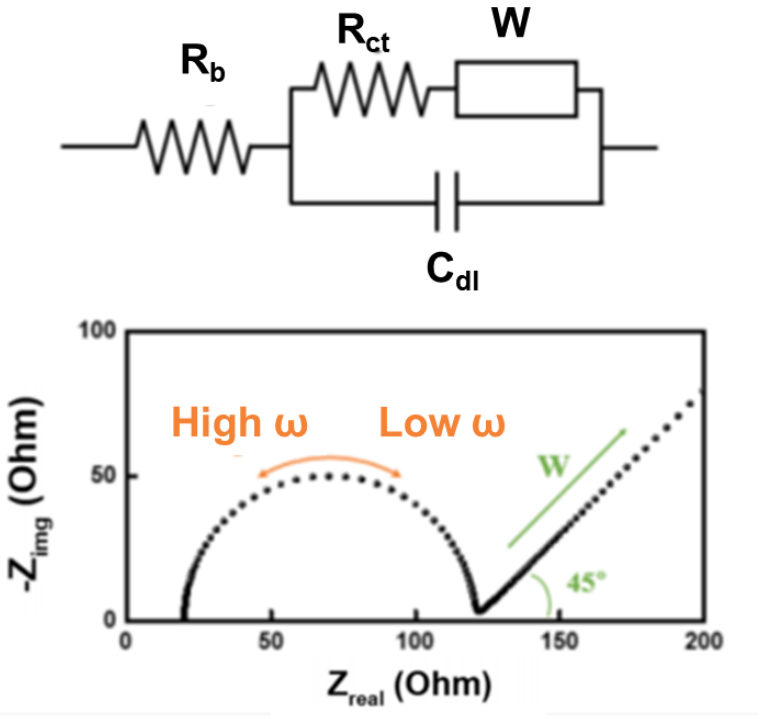


Figure 2-14. EIS Nyquist plot and equivalent circuit of Randles cell model.[202]

Generally, EIS is used to compare the charge-transfer resistance, diffusion coefficient and electrolyte resistance of the fabricated batteries. In this thesis, CV and EIS characterizations of fabricated cells were performed on Biologic VMP-300 station.

Chapter 3 Eutectic Etching toward In-Plane Porosity Manipulation of Cl-Terminated MXene for High-Performance Dual-Ion Battery Anode

3.1 Introduction

Dual-ion batteries (DIBs) are emerging lithium-ion battery alternative with a working mechanism that involves intercalation of both anions and cations in respective electrodes. They have advantages of high theoretical energy density and discharge voltage, but struggle with low anode capacity and reversibility.[60, 104, 106, 203-205] To this matter, MXenes with excellent conductivity (6000-8000 S cm^{-1}) may be an adequate solution given their promising performances in studies as intercalation anode.[9, 206] They have a general chemical formula of $M_{n+1}X_nT_x$, with M being early transition metal, X representing carbon and/or nitrogen, T_x are surface terminations such as F, OH, O, Cl and n can be integer of 1, 2 or 3.[56, 207, 208] Typically, MXenes are synthesized via selectively etching of A elements from MAX ($M_{n+1}AX_n$, with A being mostly III A and IVA elements) precursors using hazardous fluoride containing solutions.[2, 17] The material family have demonstrated capability in forming flexible three dimensional (3D) foam electrodes with out-of-plane porosity through methods such as hard-templating, achieving rapid mass transport and high rate capability desired for battery application.[57] Despite so, low surface area and limited site accessibility of MXenes remain major challenges to be overcome.[51, 54, 209-211]

Previous studies have attempted to resolve the limitations by incorporating in-plane porosity on MXene with post-synthesis processing such as sulfur loading-removal and oxidative chemical etching, but these often result in partial oxidation to the undesired TiO_2.[56, 59, 212] Alternatively,

redox coupling between A-site elements in MAX phases and cations in Lewis acids melts was investigated to explore new MAX phases and surface chemistries to achieve desirable properties for specific applications.[213, 214] For example, non-porous MXenes with exclusively Cl-terminations can be obtained using molten salt etching agent, leading to increased lattice symmetry and improved stability.[2, 19, 215] These developments significantly reduce the environmental impacts of the synthetic process and expanded the range of possible applications for the MXene family, especially in the field of energy storage and conversion. Given such, a fluoride-free process to synthesize in-plane porous MXene with elevated Li^+ storage capability and cycling stability is highly desired.

In this work, a one-step nonhazardous eutectic etching method is reported for the first time to directly synthesize in-plane porous MXene ($Ti_3C_2Cl_2$) from MAX (Ti_3AlC_2) without post etching treatment for applications as DIBs anode. A salt mixture of NaCl/$ZnCl_2$ is developed as the etching reagent to generate porous MXene with high specific surface area of 85 m^2 g^{-1} and enhanced discharge capacity up to 382 mAh g^{-1} at 0.1 A g^{-1} for half cell, which is much higher than the 230 $mAhg^{-1}$ of non-porous MXene. A pore preserving mechanism in the etching process is proposed to explain the modified pores distribution and its correlation with the salt mixture compositions. X-Ray spectroscopies identify symmetric Ti core in the porous MXene, which enables long term cycling stability of 89% after 1000 cycles at 2.0 A g^{-1}. Furthermore, DFT calculation reveals a lower diffusion barrier of 0.20 eV for Li ions in the $Ti_3C_2Cl_2$ layers, further confirming their improved ion transportation compared to the HF treated sample. When assembled with graphitic cathode, the porous $Ti_3C_2Cl_2$ shows high discharge capacity of 242 mAh g^{-1} (calculated based on anode mass) at 0.1 A g^{-1} with stability up to 83% after 1000 cycles at 1.0 A g^{-1}. Overall, this green

chemistry approach not only provides a safer and cleaner method to synthesize MXene, but also enables selective generation of mesoporous anode with ordered crystal structure that excels in Li^+ storage.

3.2 Experimental Section

Materials: Sodium chloride (ACS reagent, ≥ 99.0%), zinc chloride (anhydrous, reagent grade, ≥ 98.0%), Ti_3AlC_2 (≥ 90.0%), natural graphite powder (325 mesh), lithium hexafluorophosphate (≥ 99.99%), hydrochloric acid (ACS reagent, 37%), Al foil, Cu foil, poly(vinylidene fluoride) and 1-Methyl-2-pyrrolidone were purchased from Sigma Aldrich. Super P conductive carbon black was purchased from MTI corporation.

Synthesis of MXene/porous MXene: In a typical process, $Ti_3C_2Cl_2$ was synthesized by annealing grinded mixture of Ti_3AlC_2 and $ZnCl_2$ under Ar at 550 ºC for 5 hours. The molar ratio of Ti_3AlC_2 to $ZnCl_2$ is 1:6.[22] Porous $Ti_3C_2Cl_2$, the $ZnCl_2$ was replaced by $ZnCl_2$/NaCl mixture with 33 mol% or 60 mol% of NaCl, the mole ratio between Ti_3AlC_2 and $ZnCl_2$ remained 1:6. Upon completion of the annealing process, the products were washed with deionized water and collected by centrifugation. Then the products were washed by 5 wt% HCl for 2 h to remove the metallic Zn, followed by washes of deionized water and freeze-drying.

Molar ratio of NaCl before and after the etching reaction. Initially, the mole ratio of MAX to $ZnCl_2$ is 1 to 6, while the ratio between $ZnCl_2$ and NaCl is 40 to 60. When the reaction between MAX and $ZnCl_2$ is processed to completion, 2.5 of the 6 $ZnCl_2$ are consumed, which would lead to changes of the NaCl mole ratio in the salt melt.[213] The final weight ratio is calculated by the equation below.

$$\frac{60}{60+\frac{40\times(6-2.5)}{6}} \times 100\% = 72\% \quad (3\text{-}1)$$

Likewise, the ratio of NaCl in $Ti_3C_2Cl_2$-33 is increased to 45.8%.

Material characterization: Morphologies of the prepared materials were obtained by Zeiss ULTRA plus Field Emission Scanning Electron Microscope. Transmission electron microscopy was tested by JEOL, JEM-2010 with voltage of 200 kV, the machine was equipped with energy-dispersive X-ray spectroscopy (EDS) for elemental mapping. X-ray diffraction patterns of the obtained samples were operated by Rigaku Miniflex 600 X-ray Diffractometer containing graphite monochromator and a Cu Kα radiation source (λ=1.5406Å). The surface area information were tested by N_2 adsorption-desorption isotherm analysis using a Brunauer-Emmett-Teller surface area analyzer (Quantachrome Instruments QuadraSorb SI4). The pore size distributions were calculated based on BJH model. X-ray photoelectron spectra measurements were carried out via Thermal Scientific K-Alpha X-ray Photoelectron Spectrometer System. Ti *K*-edge XANES measurements were presented at Canadian Light Source Inc, Canada by the SXRMB beamline in TEY mode. Reference chemicals were all purchased from Sigma-Aldrich. XANES data were processed by Athena in Demeter program.[216]

Electrochemical characterization: The battery anodes were obtained by mixing the $Ti_3C_2Cl_2$ or porous $Ti_3C_2Cl_2$ with super P and PVDF at a mass ratio of 8:1:1. With the help of solvent, the slurry was pasted onto Cu foil and subsequently dried overnight at 80 °C in vacuum oven. Afterwards, the anodes were cut into circles (d=15 mm). Meanwhile, 15 mm circular Li foil are used as counter and reference electrode, with polypropylene separator (Celgard 2400) as separator. Finally, the battery was assembled using CR2016 coin cell with 4 M $LiPF_6$/EMC as electrolyte in

argon-filled glove box. GCD tests were performed on LAND CT2001A while CV tests were conducted by computer-controlled BioLogic VMP-300 workstation from 0.01 V to 3 V. To fabricate the dual ion battery full cells, graphite was used as cathode material. The mass ratio of graphite to $Ti_3C_2Cl_2$ or porous $Ti_3C_2Cl_2$ was calibrated based on their respective discharge capacity. The full cells were tested between the voltage range of 2.0 V to 5.0 V.

Cyclic voltammetry reaction kinetic calculation: The kinetic relationship are evaluated between peak current (*i*) and scan rate (*v*) based on the following equation[217]:

$$i = av^b \tag{3-2}$$

a, b are constants. If b-value equals to 0.5, the process is a standard battery behavior; when value is 1, the surface-controlled current indicates normally capacitive behavior.

The non-diffusion contribution ratio to the discharge capacity is estimated by isolating non-diffusion current from the current *i*[217]:

$$i = k_1 v + k_2 v^{1/2} \tag{3-3}$$

where $k_1 v$ and $k_2 v^{1/2}$ are the non-diffusion and diffusion-controlled current at specific voltage. The non-diffusion ratio is analyzed by scheming $i/v^{1/2}$ vs. $v^{1/2}$ at various voltages.

Diffusion coefficient of Li^+: GITT tests are measured with pulse current of 0.1 A g^{-1} for 10 min current pulse between 30 min rest intervals. Li^+ diffusivity coefficient (D_{Li^+}) is estimated based on the folloing equation using Fick's second law[207]:

$$D_{Li^+} = \frac{4}{\pi\tau}\left(\frac{m_B V_M}{M_B A}\right)^2 \left(\frac{\Delta E_S}{\Delta E_\tau}\right)^2 \tag{3-4}$$

where τ is the time of current pulse, m_B, M_B and V_M stand for the mass, molecular weight and molecular volume of the active material, A corresponds to the geometric area of the anode, ΔE_τ and ΔE_S are the voltage difference between current pulse and rest steps.

Density functional theory. The computational simulations in this work were performed using Vienna ab-initio simulation package (VASP) with the projector augmented wave (PAW) pseudo-potentials for describing the atomic cores interaction and valence electrons based on density functional theory (DFT). The Perdew–Burke–Ernzerhof (PBE) functional within the generalized gradient approximation (GGA) were applied to implement DFT calculations.[218] In order to simulate the solvent environment throughout the calculations, an implicit solvent model was also implemented in VASPsol. A Hubbard-U correction (DFT+U method) was implemented to improve the description of localized metal d-electrons in the $Ti_3C_2T_X$ and $Ti_3C_2Cl_2$ systems. The calculations were spin-polarized. The valence electrons wave functions were expanded using a plane wave cut-off energy of 450 eV. The convergence criteria of force and energy during geometrical optimization were set to 0.02 eV $Å^{-1}$ and 10^{-5} eV, respectively. A vacuum of 15 Å was used to avoid any interactions along the z-direction. Brillouin zone integration was conducted by a Monkhorst–Pack grid with 2 × 2 × 1 k-point mesh. The diffusion energy barrier and diffusion behaviors of lithium cations on the $Ti_3C_2T_X$ and $Ti_3C_2Cl_2$ monolayers were achieved by the climbing image nudged elastic band (CI-NEB) approach.[219]

The adsorption energy can be estimated by using the equation:

$$\Delta E = E_{system-Li} - E_{system} - E_{Li} \quad (3\text{-}5)$$

where $E_{system-Li}$, E_{system} and E_{Li} are the total energy of the adsorption system, the clean surface, and the adsorption species, respectively. Accordingly, adsorption energy that are more negative indicates an adsorption process that is energetically favorable.

3.3 Results and Discussion

3.3.1 Material Characterization

Three sets of MXene, $Ti_3C_2Cl_2$-0, $Ti_3C_2Cl_2$-33 and $Ti_3C_2Cl_2$-60 were prepared through a one-step etching method using NaCl/$ZnCl_2$ eutectic mixture of varying composition; the number behind the chemical formula represents the NaCl mole percent in the salt mixture. Furthermore, basal planes exfoliation of the treated MXene is confirmed by comparing their scanning electron microscopy (SEM) images to the MAX precursor (**Figure 3-1a-d**), which show clear separations of layers along the entire particle. While corresponding energy-dispersive spectroscopy (EDS) analysis reveals elemental composition similar to previous reporting (**Figure 3-1e**).[22]

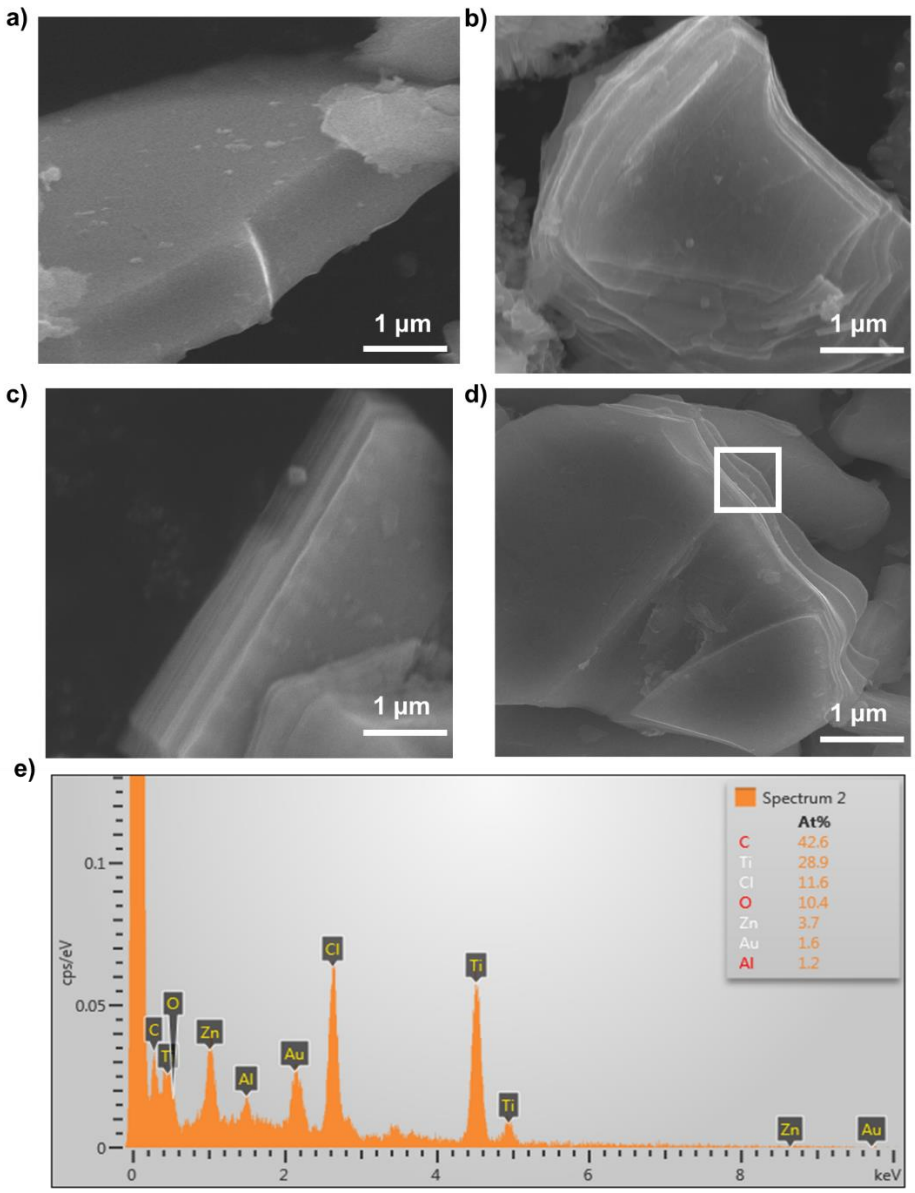


Figure 3-1. SEM images of a) Ti_3AlC_2, b) $Ti_3C_2Cl_2$-0, c) $Ti_3C_2Cl_2$-33 and d) $Ti_3C_2Cl_2$-60. e) Corresponding EDS analysis of $Ti_3C_2Cl_2$-60.

Identities and crystal structures of the samples were first verified using X-ray diffraction (XRD) analysis (**Figure 3-2a**). The results show that the (104) peak intensity of Ti_3AlCl_2 (JCPFD:

#52-0875) at 39º is substantially reduced for all three samples, indicating significant crystal structure modification and successful exfoliation of the MAX phase. Meanwhile, an intense (002) peak emerges for $Ti_3C_2Cl_2$-0, $Ti_3C_2Cl_2$-33 and $Ti_3C_2Cl_2$-60 at 7.94º, 7.92º and 7.23º, respectively, corresponding to interlayer spacing of 11.13 Å, 11.15 Å and 12 Å. The expansion reflects increasing abundancy of Cl terminations on the TiC layers, which enact repulsion forces between the layers. These lattice spacing parameters are also wider than ones typically measured on $Ti_3C_2T_x$ terminated with -OH or -F functionalities due to the larger radius of Cl atoms.[1] Upon confirming their identity and physical morphologies, the samples were further investigated by N_2 adsorption-desorption analysis to evaluate their surface area and porosity. As shown in **Figure 3-2b**, both $Ti_3C_2Cl_2$-33 and $Ti_3C_2Cl_2$-60 exhibit Type IV-isotherm with clear hysteresis loops, which is indicative of their mesoporosity.[220] This contrast clearly against the isotherm of $Ti_3C_2Cl_2$-0 prepared using only $ZnCl_2$, with minimal hysteresis at the high pressure range. Specific surface area of the $Ti_3C_2Cl_2$-0, $Ti_3C_2Cl_2$-33 and $Ti_3C_2Cl_2$-60 calculated using the Brunauer-Emmett-Teller (BET) model are 17 m^2g^{-1}, 37 m^2g^{-1}, and 85 m^2g^{-1}, respectively. Pore size distribution analysis shows that $Ti_3C_2Cl_2$-0 contains primarily micropores with sizes below 2 nm and almost no mesopores (**Figure 3-2c**). In comparison, $Ti_3C_2Cl_2$-33 prepared with the NaCl/$ZnCl_2$ eutectic mixture shows slight micropores and large mesopores volume growth. The increase in mesopore volume is even more substantial for $Ti_3C_2Cl_2$-60 prepared with additional NaCl, with the increment particularly concentrated on pores with diameter between 3 to 4 nm. The increase in porosity would likely benefit the material electrochemical performance as both site accessibility and mass diffusion are improved.

Given that NaCl is not expected to participate in the etching process,[22] the porosity changes must therefore be a direct result of the differences in salt melt phase transition temperature and recrystallize particle sizes induced by varying NaCl proportion. The differences in sample porosity can be clearly identified from their transmission electron microscopy (TEM) figures. As shown in **Figure 3-2d**, in-plane micropores can hardly be found on the $Ti_3C_2Cl_2$-0 sheet that exhibits crystal lattice pattern with interlayer spacing of 1.1 nm. As for the $Ti_3C_2Cl_2$-33 sheet, pores smaller than 3 nm and interlayer spacing of 1.1 nm can be observed (**Figure 3-2e**). Lastly for $Ti_3C_2Cl_2$-60, numerous mesopores ranging from 2-6 nm are observed to be homogenously distributed across the entire sheet surface, and expanded interlayer spacing of 1.2 nm is identified (**Figure 3-2f**). Uniform distribution of Ti, C, Cl in $Ti_3C_2Cl_2$-60 is also confirmed by corresponding scanning transmission electron microscopy (STEM) elements mapping (**Figure 3-3)**. These TEM results agree well with the previous characterizations, with the interlayer spacing measured precisely matching the XRD (002) peak angles of the targeted MXene, while the pore size and quantity observed complement the N_2 adsorption findings of mesopore volume growth with increasing NaCl content.

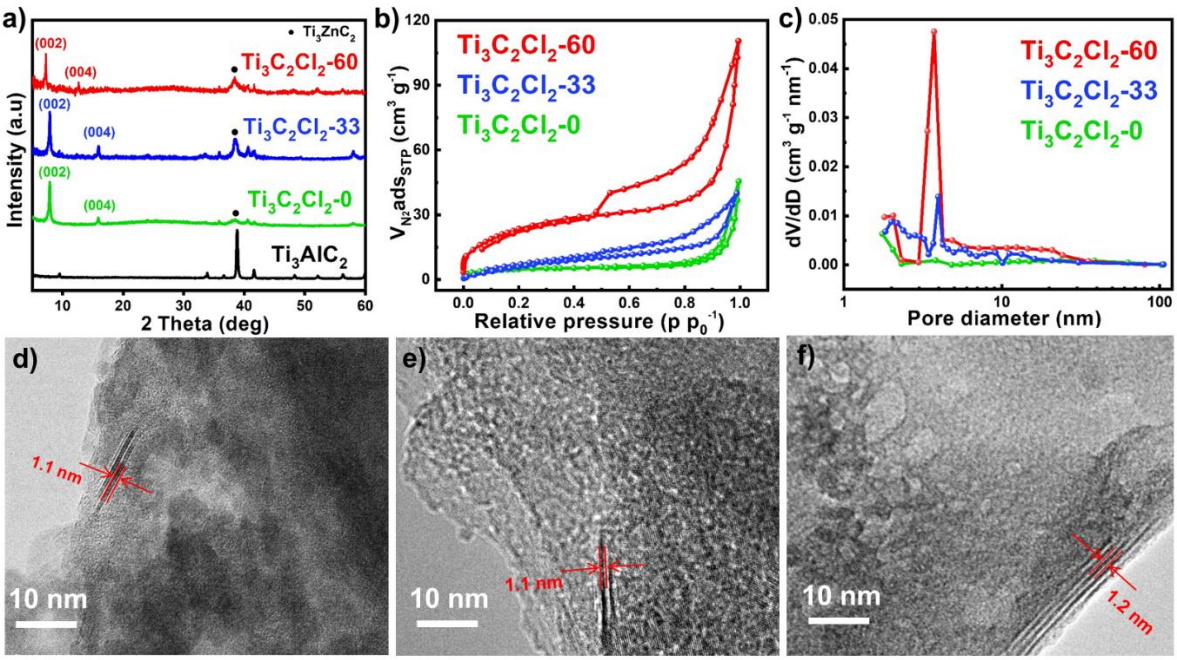


Figure 3-2. a) X-Ray diffraction patterns of Ti_3AlC_2, $Ti_3C_2Cl_2$-0, $Ti_3C_2Cl_2$-33 and $Ti_3C_2Cl_2$-60. b) N_2 adsorption–desorption isotherms, c) pore size distribution of $Ti_3C_2Cl_2$-0, $Ti_3C_2Cl_2$-33 and $Ti_3C_2Cl_2$-60. d)-f) TEM images of $Ti_3C_2Cl_2$-0, $Ti_3C_2Cl_2$-33 and $Ti_3C_2Cl_2$-60.

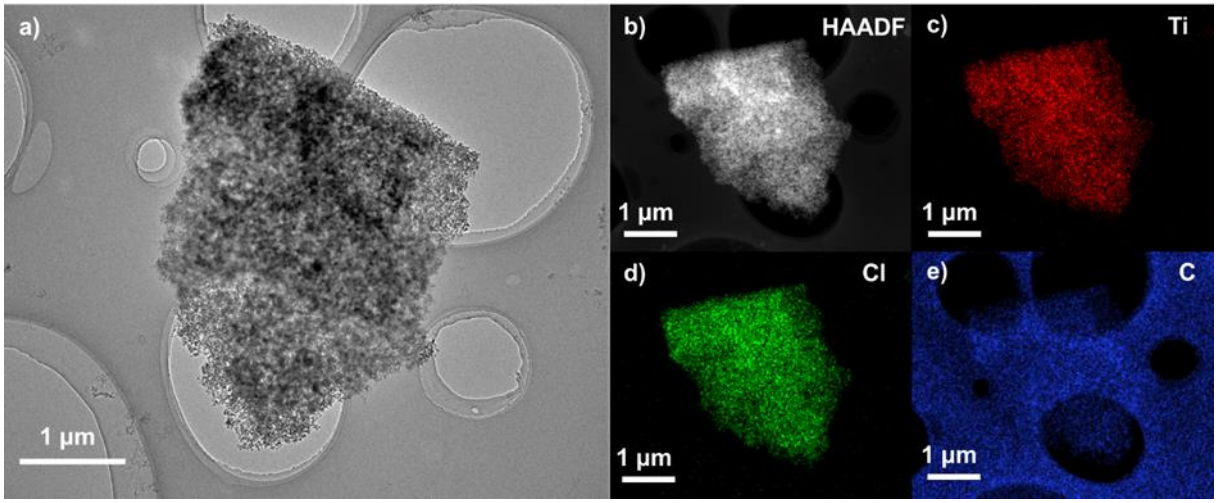


Figure 3-3. a) TEM, b) STEM-HAADF and corresponding c) Ti, d) Cl, and e) C elemental mapping images of $Ti_3C_2Cl_2$-60.

Combining the above findings, working mechanism of the one-step eutectic mixture etching method and effects of salt mixture composition on tuning material porosity are proposed and illustrated in **Figure 3-4a**. It shows that with increasing temperature, the melting salt mixture gains mobility that allows the $ZnCl_2$ to undergo redox reaction with the weakly bonded Al layers in Ti_3AlC_2, generating $Ti_3C_2Cl_2$, Zn metal and $AlCl_3$. The overall reaction can be described by the formulas below reported in previous literature:[213]

$$2Ti_3AlC_2 + 3ZnCl_2 \rightarrow 2Ti_3C_2 + 2AlCl_3(g) \uparrow + 3Zn \qquad (3\text{-}6)$$

$$Ti_3C_2 + ZnCl_2 \rightarrow Ti_3C_2Cl_2 + Zn \qquad (3\text{-}7)$$

Of the three products, the $AlCl_3$ is vaporized by the high annealing temperature, along with structural/crystal defects originally on the precursor, they form void spaces that are then occupied by the freely moving salt melt. These newly established pores are vulnerable to collapse when the salt melt gradually recrystallizes and applies retraction motion that causes surface tension.[221, 222] To avoid this, formation of larger individual crystals within the MXene layers from the NaCl/$ZnCl_2$ salt melt can provide temporary physical supports, which enables adequate post-synthesis treatment (acid wash and freeze dry) to maintain the mesopores.

The specific transition can be explained with the salt mix phase diagram, in which the samples are all first heated to the temperature of 550 ºC required to react with Ti_3AlC_2 (**Figure 3-4b**).[22, 223] At this temperature, $ZnCl_2$ in the salt melt are gradually consumed as the reaction is progress to completion, shifting the NaCl mole faction from 33% to 45.8% for $Ti_3C_2Cl_2$-33 and from 60% to 72% for $Ti_3C_2Cl_2$-60. For $Ti_3C_2Cl_2$-60, the mole fraction change moves the salt melt across the phase boundary, simultaneously causing the formation of NaCl particles, which would then reside in the void space created by the etching process. In the ensuing cooling process, presence of these

NaCl particles provides physical reinforcement for the pores as the salt melts retract away and crystallize, preventing the immediate collapse of the structure. In comparison, the salt melt in $Ti_3C_2Cl_2$-33 would not form any solid particles at 550 ºC, instead the solid particles (Na_2ZnCl_4) formation only occurs when the sample is cool to around 300 ºC. The delayed particle formation means that a portion of the pores in $Ti_3C_2Cl_2$-33 will not have the support to avoid the collapse, resulting in lower pore volume and surface area compared to $Ti_3C_2Cl_2$-60. As for the $Ti_3C_2Cl_2$-0 sample prepared using $ZnCl_2$ as the sole etching agent, absence of mesopore in their nitrogen adsorption analysis likely indicates the $ZnCl_2$ particles are either not sufficiently large to support the structure or their formation occurred after the structure has already collapsed. Based on these analyses, the 60% NaCl mole fraction is identified to be an appropriate value for effective functioning of the pore-preserving mechanism. Lowering the value is shown to be less effective in the $Ti_3C_2Cl_2$-33 sample as delayed particle formation will result in less pore being preserved, while further increasing the ratio would cause solid formation prior to the etching reaction, which prevents particles entry into the MXene interior to provide structural support during fluid retraction. This hypothesis is supported by XRD patterns of $Ti_3C_2Cl_2$-33 and $Ti_3C_2Cl_2$-60 before they were washed by HCl (**Figure 3-4c**) which confirms the presence of Na_2ZnCl_4 (ICSD #402063) and NaCl (#ICSD 41439) in $Ti_3C_2Cl_2$-60 as predicted by the phase diagram, whereas the annealed $Ti_3C_2Cl_2$-33 is found to consist of $ZnCl_2$ (#ICSD 16787) and Na_2ZnCl_4.

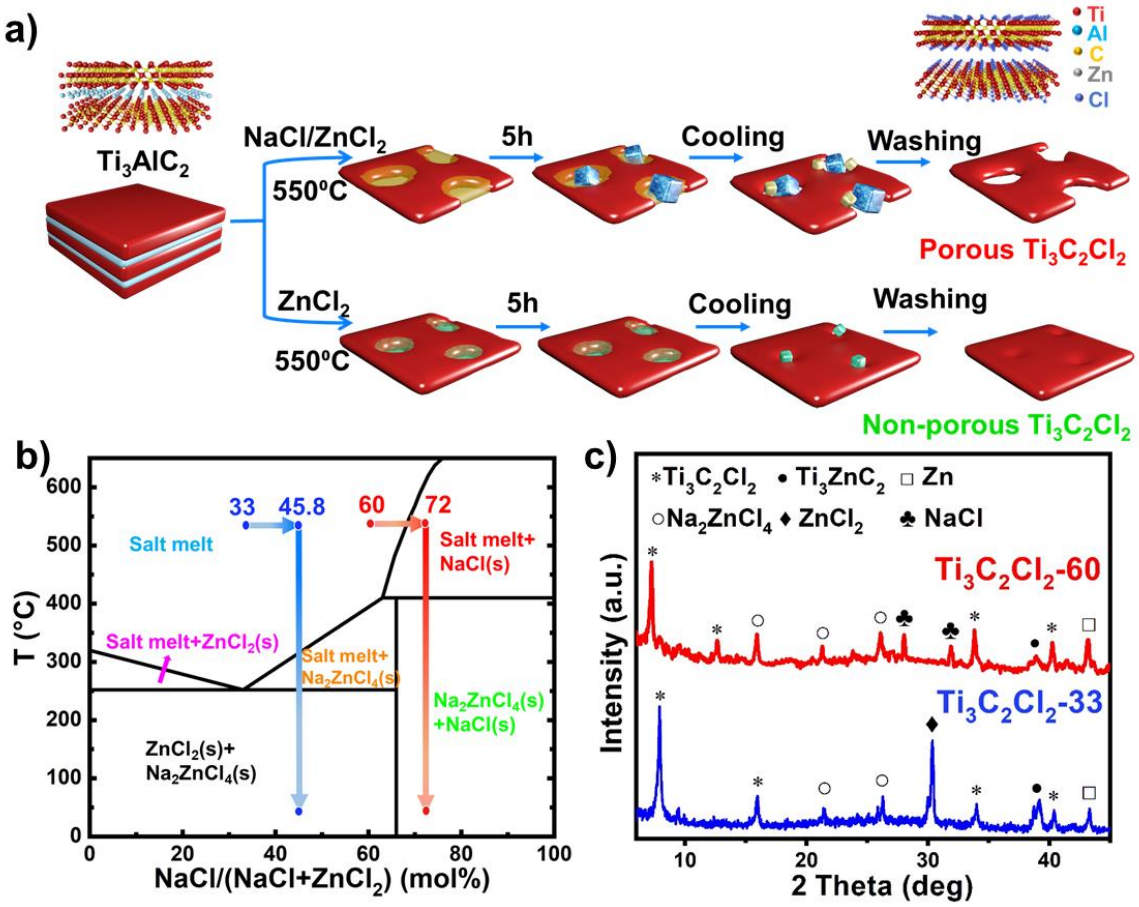


Figure 3-4. a) Schematic illustration of in-plane porous $Ti_3C_2Cl_2$ synthesized by MAX and salt mixture. b) Phase diagram of $NaCl/ZnCl_2$. Specific data obtained from previous literature.[223] Blue and red line represent the reaction process of $Ti_3C_2Cl_2$-33 and $Ti_3C_2Cl_2$-60. c) XRD patterns of $Ti_3C_2Cl_2$-33 and $Ti_3C_2Cl_2$-60 before the HCl washing process.

3.3.2 Electrochemical Results

Influence of the structural porosity on lithium-ion storage capabilities were then evaluated through galvanostatic charge and discharge (GCD) on MXenes half cells in the potential window of 0.01V–3.0 V vs Li^+/Li. As shown in **Figure 3-5a**, $Ti_3C_2Cl_2$-60 delivers a capacity of 382 mAh

g^{-1} at the rate of 0.1 A g^{-1}, which is higher than the 230 $mAhg^{-1}$ of $Ti_3C_2Cl_2$-0, the 292 mAh g^{-1} of $Ti_3C_2Cl_2$-33, the 146 $mAhg^{-1}$ of $Ti_3C_2T_x$ prepared by HF etching and outperforms most Ti-based MXene previously reported in the literatures (**Table 3-1**). After several cycles of stabilization, $Ti_3C_2Cl_2$-60 reaches an average Coulombic Efficiency (CE) of around 99.5%, indicating high reversibility toward Li intercalation/de-intercalation (**Figure 3-5b**).[208, 224] Its high structural stability is also reflected through the 95.7% capacity retention after 100 cycles of charge and discharge, as well as the minor (002) diffraction interlayer space expansion from 12.0 Å to 12.4 Å in the same period (**Figure 3-5c**).[225, 226] Benefiting from its mesoporous structure that provides shorter diffusion paths and lower ion-transport resistance, $Ti_3C_2Cl_2$-60 also achieves high capacity of 320, 281, 251, and 216 mAh g^{-1} at the current density of 0.2, 0.5, 1.0 and 2.0 A g^{-1}, exceeding those of $Ti_3C_2Cl_2$-33 and $Ti_3C_2Cl_2$-0 (**Figure 3-5d**). All three samples experience no performance lost when the current is returned to 0.1A g^{-1}, reflecting their suitability toward rapid exchange between high and low current cycling.

The cyclic voltammetry (CV) curves of $Ti_3C_2Cl_2$-60 aligns well with the GCD results, displaying a pair of broad redox peaks at around 1.9/1.6 V, which corresponds to the extraction/insertion of Li^+ in a typical anode electrode (**Figure 3-5e**).[200] Kinetic analysis of the CV scan rate (v) and peak current density (i) by log(v)-log(i) plots shows linear fits with slope of 0.844 for the cathodic peak and 0.839 for the anodic peak (**Figure 3-5f**), suggesting the electrochemical reactions of $Ti_3C_2Cl_2$-60 are primarily non-diffusion limited.[207] This is further confirmed by quantifying the diffusion dependency of the electrochemical process, which shows over 59.4% of the electrochemical process at the 1 mV s^{-1} scan rate is not diffusion restricted (**Figure 3-5g**). The non-diffusion limited contribution becomes more pronounced as the scan rate

increases and reaches 89.7% at 10 mV s^{-1} (**Figure 3-5h**), reflecting its capability in accommodating high current cycling. Given its predominately non-diffusion limited charge storage mechanism combining the metallic conductivity, $Ti_3C_2Cl_2$-60 presents the possibility to overcome the often problematic trade-off between energy density and power density.[212] Moreover, cycling stability of the three as-prepared $Ti_3C_2Cl_2$ samples were compared by standard GCD at the current density of 2.0 A g^{-1} (**Figure 3-5i**). As shown, $Ti_3C_2Cl_2$-60 retains 89% of its initial capacity after 1000 cycles of operation, verifying its suitability for practical long-term cycling, whereas $Ti_3C_2Cl_2$-33 and $Ti_3C_2Cl_2$-0 achieve lower capacity retention of 87% and 86%, respectively. Lastly, galvanostatic intermittent titration technique (GITT) is employed and Li^+ diffusion coefficients (D_{Li^+}) of $Ti_3C_2Cl_2$-60 and $Ti_3C_2Cl_2$-0 electrodes are calculated for comparison (**Figure 3-6a, b**). The result suggests higher Li^+ diffusivity for $Ti_3C_2Cl_2$-60 in all voltage window, revealing enhanced reaction kinetic and lower diffusion barrier as a result of induced porous structure.[207, 227] Analysis by electrochemical impedance spectroscopy (EIS) also clearly shows that the porous-structured $Ti_3C_2Cl_2$-33 and $Ti_3C_2Cl_2$-60 exhibit lower electron-transfer resistance with smaller semicircle and steeper slope that indicates faster ion diffusion (**Figure 3-6c**).[228, 229] In view of the above results, $Ti_3C_2Cl_2$-60 with high mesoporosity and specific area that affords superior electrochemical performance fits best as the anode material of DIBs.

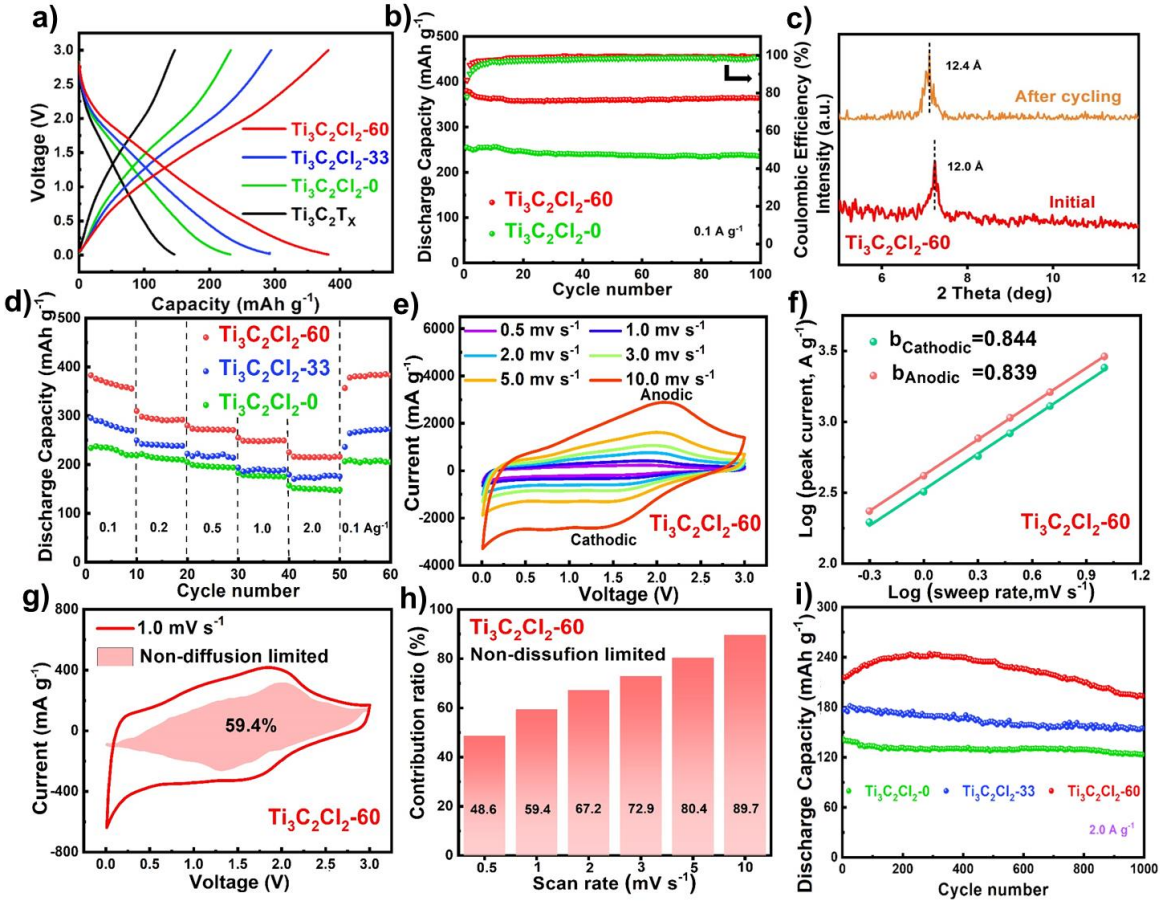


Figure 3-5. a) Galvanostatic charge-discharge curves of $Ti_3C_2Cl_2$-0, $Ti_3C_2Cl_2$-33, $Ti_3C_2Cl_2$-60 and $Ti_3C_2T_X$ at 0.1 A g^{-1}. b) Cycling and Coulombic Efficiency results of $Ti_3C_2Cl_2$-60, $Ti_3C_2Cl_2$-0 at 0.1 A g^{-1}. c) *Ex-situ* xrd results of $Ti_3C_2Cl_2$-60 before and after cycling for 100 cycles at 0.1 A g^{-1}. d) Rate capability test of $Ti_3C_2Cl_2$-0, $Ti_3C_2Cl_2$-33 and $Ti_3C_2Cl_2$-60. e) CV curves at various scan rates from 0.5 to 10.0 mV s^{-1} of $Ti_3C_2Cl_2$-60. f), g) Calculation of b-values and capacitive contribution of $Ti_3C_2Cl_2$-60. h) Contribution ratio of the capacitive at different scan rates of $Ti_3C_2Cl_2$-60. i) Long term cycling result of $Ti_3C_2Cl_2$-0, $Ti_3C_2Cl_2$-33 and $Ti_3C_2Cl_2$-60.

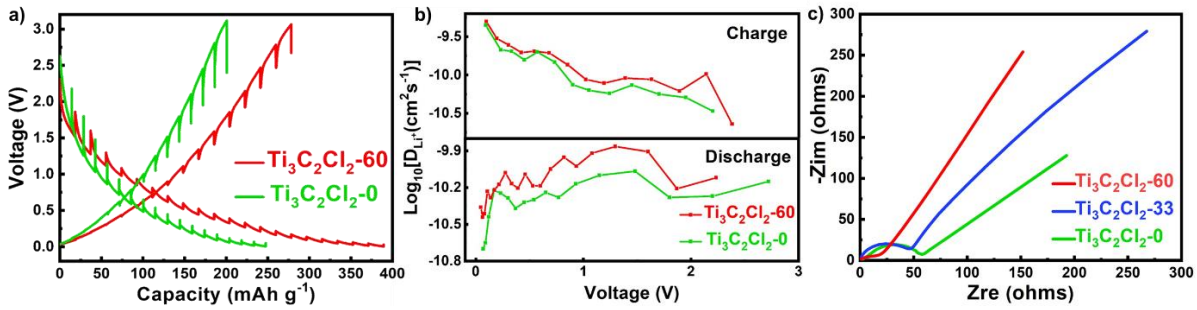


Figure 3-6. a) GITT curves and b) calculated Li^+ diffusion coefficients in $Ti_3C_2Cl_2$-60 and $Ti_3C_2Cl_2$-0. c) EIS data of $Ti_3C_2Cl_2$-60, $Ti_3C_2Cl_2$-33 and $Ti_3C_2Cl_2$-0.

Table 3-1. MXene-based anodes in lithium-ion batteries

Material	**Etching/ Treatment**	**Potential (V vs. Li/Li^+)**	**Electrolyte**	**Capacity ($mAhg^{-1}$)**	**Cyclability**	**Ref.**
$Ti_3C_2T_x$	HF	0.005-3	1 M $LiPF_6$	120 at 0.03A/g	~25% after 50 cycles	230
$Ti_3C_2T_x$	HF	0.05-2.5	1 M $LiPF_6$	123 at 0.26 A/g	96% after 75 cycles	231
$Ti_3C_2T_x/TiO_2$	Heat under CO_2	1-3	1 M $LiClO_4$	124 at 0.05 A/g	Stable for 400 cycles	232
$Ti_3C_2T_x$/Si	Ultrasonication	0.05-2.5	/	188 at 0.2 A/g	Stable for 150 cycles	233
$Ti_3C_2T_x$/CNT	Mix with 10% CNT	1-3	1 M $LiPF_6$	~210 at 0.5 C	~95% after 100 cycles	207
Porous $Ti_3C_2Cl_2$	$NaCl/ZnCl_2$	0.01-3	4 M $LiPF_6$	382 at 0.1 A/g	89% after 1000 cycles	**This work**

3.3.3 Structural Analyzation

Given the much-improved electrochemical performance of $Ti_3C_2Cl_2$-60 over previously reported F, or OH terminated MXenes (**Table 3-1**), elemental characteristics of $Ti_3C_2Cl_2$-60 and the HF etched $Ti_3C_2T_x$ were further analyzed. X-ray photoelectron spectroscopy (XPS) analysis determines the atomic ratio in $Ti_3C_2Cl_2$-60 of Ti to Cl is 1.53 to 1 (**Table 3-2**), with small amount of residual Zn particles, which matches that reported in the literature.[22] Deconvolution of the Ti 2*p* spectra shows fours peaks at 461.6 eV, 460.3 eV, 455.6 eV, and 454.2 eV that correspond to the $2p_{1/2}$ and $2p_{3/2}$ orbitals of the core TiC_6 octahedral structures in Ti_3C_2 based MXene (**Figure 3-7a**).[192, 234] Two additional peaks with higher valence at 458.2 eV and 464.0 eV are also observed, which are assigned to the $2p_{3/2}$ and $2p_{1/2}$ orbital of Ti bonded to Cl terminations.[235, 236] Presence of the Ti-Cl bond is also supported by identification of its corresponding $2p_{3/2}$ and $2p_{1/2}$ peak at 198.7 eV and 200.4 eV in the Cl 2*p* spectrum (**Figure 3-7b**).[235, 236] These analyses suggest that the $Ti_3C_2Cl_2$-60 is almost entirely Cl-terminated, specific details of the XPS analysis is provided in **Table 3-3**. As for the HF-etched $Ti_3C_2T_x$, five separate peaks are identified in the deconvolution of its $2p_{3/2}$ spectrum, which include the Ti-C (I) bond at 455.0 eV, the Ti-C (II) bond at 456.0 eV, Ti-C (III) bond at 457.5 eV, Ti-O bond at 459.1 eV and Ti-F_x bond at 460.4 eV (**Figure 3-7c**, **Table 3-4**).[192, 237-239] Separation of the Ti-C adsorption to three peaks with different oxidation states is likely caused by incorporation of -O, -F and -OH terminations on the $Ti_3C_2T_x$, which causes polarization of different strengths to the core Ti_3C_2 layers.[238, 239] The presence of the -F and -O groups are also confirmed from the F *1s* spectra showing signals of Ti-F and $Al(OF)_x$ (**Figure 3-7d**).[239] These comparisons between the two samples reveal that $Ti_3C_2Cl_2$-60 prepared by the one step eutectic etching methods exhibit more ordered elemental distribution in its core,

which is attributed to the use of high temperature annealing that prevents the formation of O_x termination and leads to edges that are almost entirely Cl terminated.[240] Previous studies have reported that steric from the enlarged Cl terminations allows more rapid and extensive Li interaction,[215] which would explain the improved electrochemical performance of the $Ti_3C_2Cl_2$ samples over the HF-treated $Ti_3C_2T_x$.

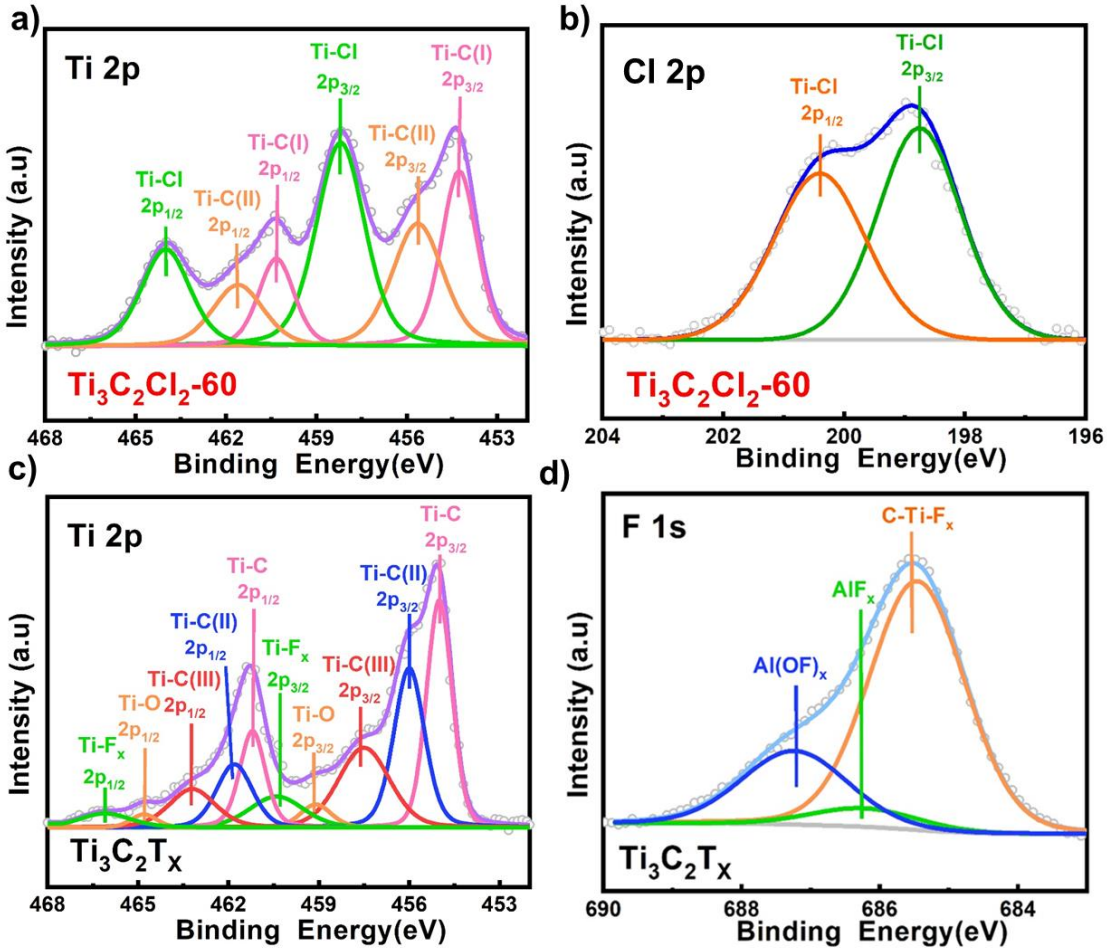


Figure 3-7. a), b) Ti 2p and Cl 2p XPS spectra of $Ti_3C_2Cl_2$-60. c) Ti 2p XPS spectra of $Ti_3C_2T_X$. d) F 1s XPS spectra of $Ti_3C_2T_X$.

Table 3-2. Atomic composition of $Ti_3C_2Cl_2$-60

Element	Ti	C	Cl	Zn
mol%	41.1	29.6	26.9	2.4

Table 3-3. Elements from the XPS spectra of $Ti_3C_2Cl_2$-60

Region	BE(eV)	FWHM(eV)	Fraction	Assigned to
Ti $2p_{3/2}$ ($2p_{1/2}$)	454.2 (460.3)	1.4	24.5	Ti-C
	455.6 (461.6)	2	31.5	Ti-C
	458.2 (464.0)	1.9	44	Ti-Cl
Cl $2p_{3/2}$ ($2p_{1/2}$)	198.7 (200.4)	1.6 (1.8)	100	Ti-Cl

Table 3-4. Elements from the XPS spectra of $Ti_3C_2T_X$ ($Ti_3C_2O_{0.1}F_{1.4}(OH)_{0.5}$)

Region	BE(eV)	FWHM(eV)	Fraction	Assigned to
Ti $2p_{3/2}$ ($2p_{1/2}$)	455.0 (461.2)	1	33	Ti-C
	456.0 (461.7)	1.2 (1.4)	29	Ti(II)
	457.5 (463.2)	2 (1.8)	24	Ti(III)
	459.1 (464.8)	1.2 (1)	4.3	Ti-O
	460.4 (466.1)	2.1 (2)	9.6	Ti-F_X
F $2p_{3/2}$ ($2p_{1/2}$)	685.46	1.62	71	Ti-F
	686.2	1.8	5.8	Al-F_X
	687.2	1.8	23.2	$Al(OF)_X$
O 1s	529.9	1.74	17	Ti-O
	532	2.1	83	Ti-OH

X-ray absorption spectroscopy (XAS) was also employed to compare the chemical nature of the molten salt synthesized $Ti_3C_2Cl_2$ and the HF-etched $Ti_3C_2T_x$. **Figure 3-8** shows the Ti *K*-edge X-ray absorption near edge spectroscopy (XANES) of different samples. The adsorption edge of $Ti_3C_2Cl_2$-0, $Ti_3C_2Cl_2$-60 and $Ti_3C_2T_x$ all resemble more closely to the curve of Ti_3C_2 in comparison to TiO_2 or Ti foil. In MXene, the weak pre-edge absorption features represent the Ti 1*s* → C 2*p*-Ti 3*d* hybridized molecular orbital excitation, while the main-edge region is assigned to the dipole-allowed transition from Ti 1*s* to the unoccupied 4*p* orbital.[241, 242] The adsorption edge of $Ti_3C_2Cl_2$ (4973 eV) and $Ti_3C_2T_x$ (4976 eV) are both near that of Ti_3C_2 (4975.8 eV), which locates between

the edges of TiO_2 (4983 eV) and Ti foil (4971.9 eV), indicating their carbide nature.[1] The lower edge energy of the two $Ti_3C_2Cl_2$ indicates lower average Ti oxidation state compared to $Ti_3C_2T_x$, which is consistent with its lower Ti-C $2p_{3/2}$ binding energy measured in XPS. This can be explained by the lower electronegativity of Cl compared to F, which attracts less electron density from the Ti_3C_2 core.[37] Moreover, pre-edge peak of the $Ti_3C_2Cl_2$ samples is visibly less distinct compare to the peak of $Ti_3C_2T_x$, revealing their more symmetric Ti_6C octahedra core.[241, 243] This is likely due to Cl being the primary termination of their edges, which predominately occupies the face-centered cubic (fcc) site.[243, 244] Such arrangement is favorable for ion transport, which likely contributes to the improved electrochemical performance.

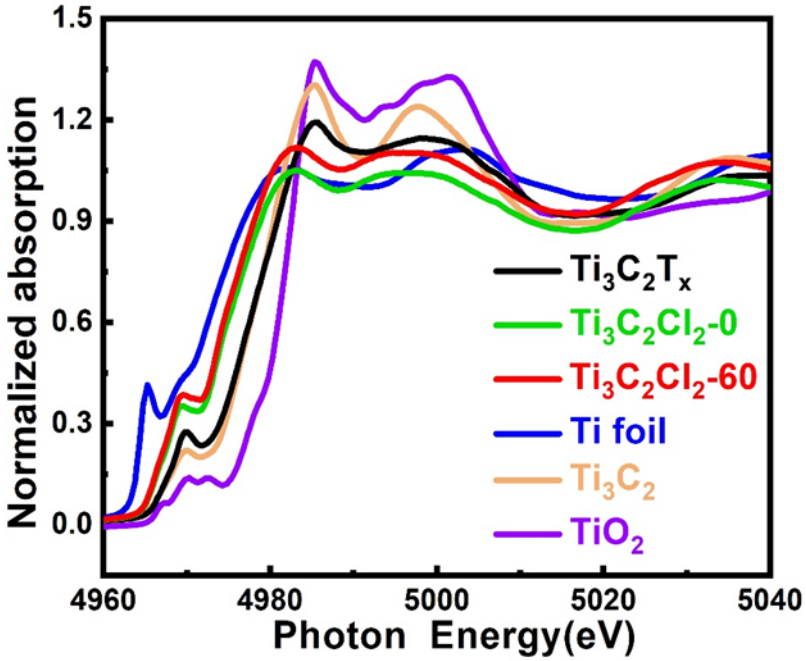


Figure 3-8. XANES spectra of Ti *K*-edge for $Ti_3C_2T_X$, $Ti_3C_2Cl_2$-0 and $Ti_3C_2Cl_2$-60 compared to references including Ti foil, Ti_3C_2 and TiO_2.

Electronic states of the samples were also analyzed through comparing their stable monolayer configuration in DFT modeling, $Ti_3C_2O_{0.1}F_{1.4}(OH)_{0.5}$ was adapted for the HF-treated $Ti_3C_2T_X$ based on the elemental composition measured by XPS (**Figure 3-9a**). As shown in **Figure 3-9b**, both $Ti_3C_2Cl_2$ and $Ti_3C_2T_X$ exhibit non-zero density of states (DOS) at the Fermi energy (E_f), indicating that both are electronic conductors.[245] It is revealed that their high electronic conductivity mainly originates from the Ti d orbitals (Ti_d), as contribution of these orbitals dominates the conduction bands.[246] As for the valance bands, states of $Ti_3C_2Cl_2$ consist of mix contributions from the Ti *d* orbitals, C *p* orbitals and Cl *p* orbitals, which suggest hybridization of orbitals from the three elements.[247] In contrast, valance band of the $Ti_3C_2T_X$ sample exhibits a section of highly densed states between the range of -8 eV to -6 eV that are almost solely occupied by the F *p* orbitals.

Furthermore, adsorption and diffusion behaviors of Li ions on surface of the two MXenes models were examined, and two adsorption sites in green and black cycles that are most energetically favorable were identified for each sample (**Figure 3-9c**). The results suggest that $Ti_3C_2T_X$ actually exhibits a slightly lower adsorption energy compared to $Ti_3C_2Cl_2$, this may be caused by the higher electronegativity of F that causes stronger negative dipoles on the material surface. However, when comparing the diffusion barrier of Li ions hopping pass the terminations as demonstrated by the green arrow in **Figure 3-9d**, Cl atoms on $Ti_3C_2Cl_2$ provides a path with relatively low activation energy of 0.20 eV. In comparison, Li ions migration on top of the F atoms on $Ti_3C_2T_X$ would require an activation energy of 0.72 eV, making it less likely to occur.[248] It is noted that hopping migration on top of an termination occurs less frequently compare to hopping between adjacent Ti and C atom, but the accessibility to an additional migration path through the

Cl atoms would likely be beneficial for battery performance when high power charging/discharging is required.

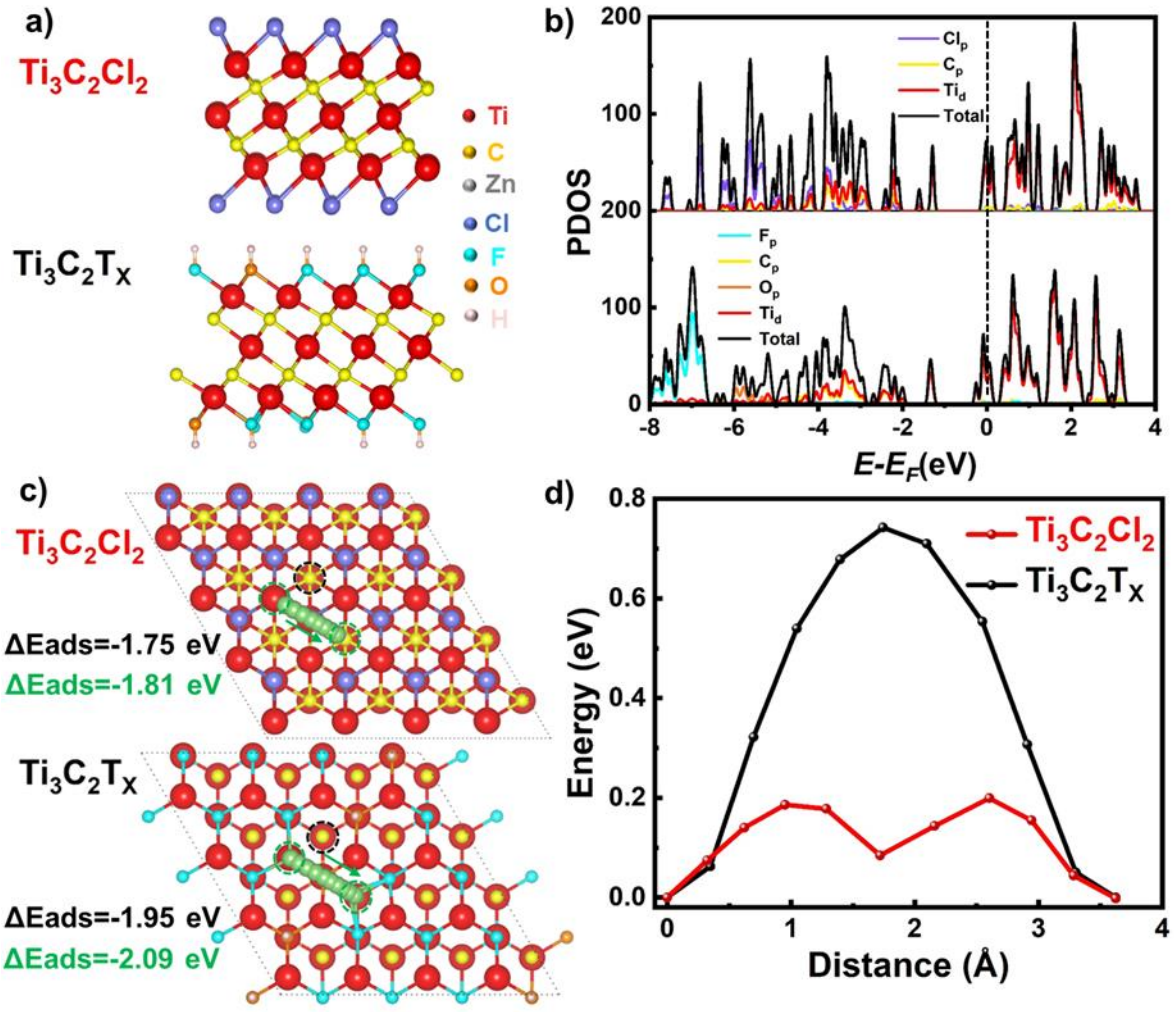


Figure 3-9. a) Optimized geometries and b) projected density of states of $Ti_3C_2Cl_2$ (upper) and $Ti_3C_2T_X$ (bottom). c) Adsorption energy of energetically favorable sites and d) diffusion barrier profiles of Li ion hopping migration on the selected terminations of $Ti_3C_2Cl_2$ and $Ti_3C_2T_X$ surfaces.

3.3.4 Full Cell Performance

To demonstrate the practical potential of the porous MXene, DIB full cell fabricated using $Ti_3C_2Cl_2$-60 as anodes and graphite as cathode, was cycled between 2.0-5.0 V (**Figure 3-10a**). Two distinctive charge (4.75 V and 4.9 V)/discharge (4.5 V and 4.7 V) plateaus corresponding to the intercalation/de-intercalation of PF_6^- can be observed.[249] The discharge capacities of $Ti_3C_2Cl_2$-60/graphite DIB are 242, 219, 201, 161, 112 mAh g^{-1} at 0.1, 0.2, 0.5, 1.0 and 2.0 A g^{-1}, respectively (**Figure 3-10a, b**). Notably, the $Ti_3C_2Cl_2$-60/graphite cell can still deliver a capacity of 141 mAh g^{-1} after 1000 cycles, with 83% retention at 1.0 A g^{-1} (**Figure 3-10c**). The average CE of approximately 95% is not desirable, and this deficiency is attributed to unoptimized electrolyte composition and unsatisfactory reversibility of PF_6^- intercalation/extraction in the cathode.[250, 251] Despite so, overall performance of the full cell is competitive versus DIBs based on other anode reported in previous studies,[204, 252-255] and improvement is expected with further development in high voltage electrolyte and novel anion-host cathodes to pursue high CE.[106]

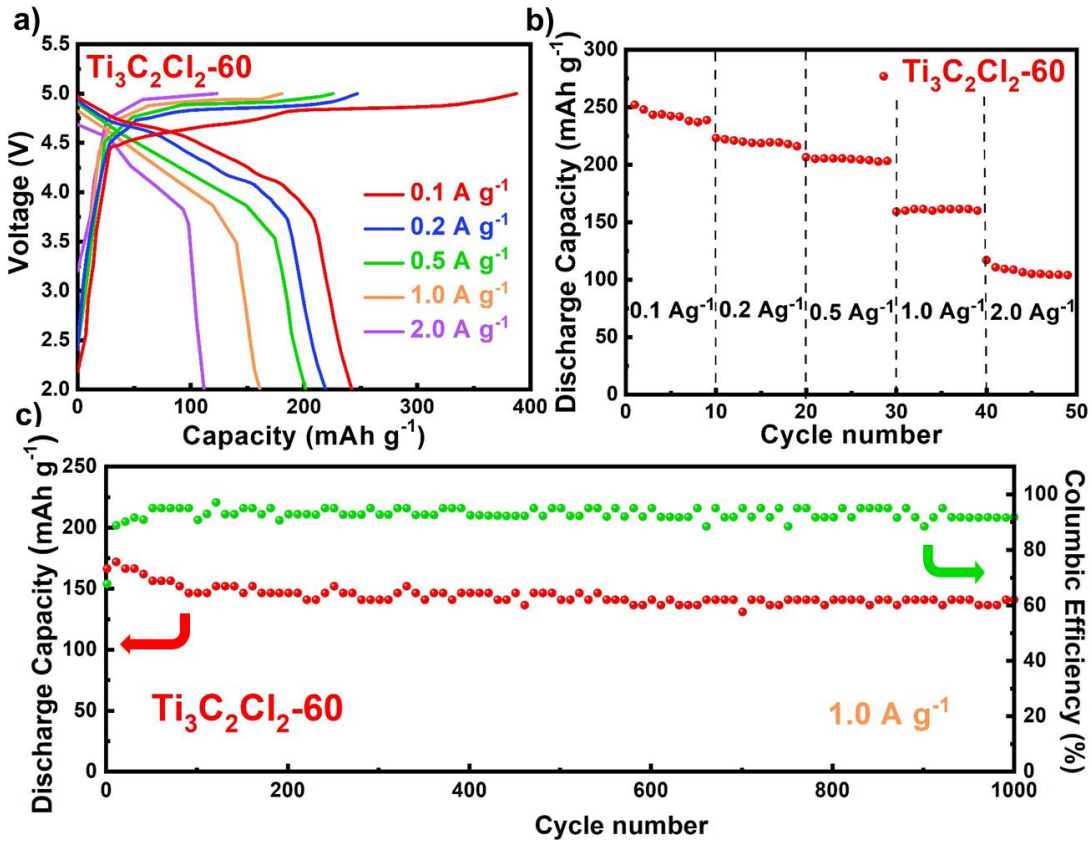


Figure 3-10. a)-c) GCD curves, rate performance and long cycling data of $Ti_3C_2Cl_2$-60 based DIBs.

3.4 Conclusion

In summary, NaCl/$ZnCl_2$ salt mixture is firstly applied to produce in-plane porous MXene in a facile annealing process. Influences of the salt proportion to structure morphologies were evaluated and a pore preserving mechanism of the eutectic mixture has been proposed. The increased surface area and mesoporosity of the samples greatly benefit the site accessibility and Li ion transportation for DIB anode applications. The optimal $Ti_3C_2Cl_2$ sample achieves a high discharge capacity of 382 mAh g^{-1} at 0.1 A g^{-1}. Moreover, the process also incorporates

predominately Cl-terminations to the Ti_3C_2 sheets, which leads to more ordered crystal structures that affords high capacity retention of 89% after operation of 1000 cycles. When assembles with graphite as full dual-ion batteries, $Ti_3C_2Cl_2$-60 achieves a reversible capacity of 242 mAh g^{-1} at 0.1 A g^{-1} (calculated based on the anode mass), and 1000 cycle capacity retention up to 83%. Overall, the eutectic mixture etching method proposed herein demonstrates a green approach for generating porous MXene with high crystal stability for DIB anode applications and presents a highly adaptable technique to achieve mesoporosity with MXene for other applications.

Chapter 4 Vacancy and Growth Modulation of Cobalt Hexacyanoferrate by Porous MXene for Zinc Ion Batteries

4.1 Introduction

Intrinsically safe and inexpensive rechargeable aqueous zinc-ion batteries (ZIBs) are one of the most attractive candidates for the next-generation energy storage devices, especially for stationary storage.[95, 140, 256] Although continuous efforts have been made to improve the electrochemical performances of ZIBs, cathode materials can yet fulfill the commercial applications requirements.[126, 129] Among the candidates of interest, Prussian blue analogues (PBAs) are favoured for their relatively high redox potential.[170] They have general formula of $MFe(CN)_6$ (M = Mo, V, Fe, Mn, Cu, Co, Ni), with FeC_6 octahedra and MN_6 octahedra forming cubic arrangement linked through the cyanide ligands.[164, 165, 257] Their unique crystal structure provides sufficient large three dimensional diffusion channels as well as weak interactions with charge-carrier active ions. Among them, cobalt hexa-cyanoferrates (CoHCF) particularly have been reported to possess ultrahigh discharge voltage and specific capacity through proper utilization of the redox pairs.[170, 258] However, low electronic conductivity and uncontrolled agglomerations that occur in conventional synthesis methods have led to significantly reduced energy density in practical application.[259-261] Moreover, abundant structural defects found in the PBAs crystals could be occupied by coordinating water molecules, which have been identified to restrict zinc insertion/extraction and weaken structural stability during electrochemical processes, causing performance decay and poor cycling stability.[262] To date, most existing modifications can only regulate single obstacle of PBAs.[263] Given such, full spectra optimization strategies are

of high interests to elevate material electronic conductivity and surface area and to reduce structural vacancies for PBAs-based electrodes to further promote the practical applications of ZIBs.

MXenes are emerging two-dimensional layered transition metal carbides and/or nitrides ($M_{n+1}X_n$, n=1,2,3) with abundant surface terminations T_X (-O, -F, -OH and -Cl).[21] Their exceptional conductivity, hydrophilicity and negatively charged surfaces make them ideal candidates as host material for composition to alleviate common drawbacks associated with energy storage materials in aqueous batteries.[2] For instance, V_2CT_X has been reported to be suitable host for the low-conductive δ-MnO_2 nanosheets, and significantly improved its rate capability as ZIBs cathode.[264] More recently, a non-hazardous and scalable method to prepare in-plane porous MXene with chemical formula of $Ti_3C_2Cl_2$ has been discovered.[265] This new MXene product not only possesses the common strengths and conductivity of MXene, but also demonstrates high surface area with uniformly distributed Cl terminations, which could interact with PBAs precursor molecules and further influence its structural and electrochemical properties.

In this work, the abovementioned $Ti_3C_2Cl_2$ are utilized to induce self-assembled growth of CoHCF nanotubes to give rise to a new composite product to be applied as ZIBs cathode. The new structure has significantly reduced all the drawbacks of original CoHCF particles and resulted in a synergistic effect on boosting the battery performance. Specifically, Co^{2+} precursors are preabsorbed onto the negatively charged MXene surface to form a metastable state that alters their interaction with CN^- and H_2O during nucleation process, which hinders formation of interstitial H_2O and reduces structural vacancies. At the same time, the CoHCF adapts a nanotube morphology with uniform mesopore under influence of the surface charges on the MXene

nanosheet. As a result of these modifications, the CoHCF nanotube and porous MXene composite achieves a high surface area of 237.9 m^2 g^{-1} and delivers high capacity of 197 mAh g^{-1} at current density of 0.1 A g^{-1}, with excellent capacity retention of 94.4% after 3000 cycles of operation at 2 A g^{-1}. This synthetic strategy presents an effective approach to inductively grow high surface area, low-vacancies PBAs homogeneously on conductive porous MXene for high performance ZIBs cathodes, paving road for future MXene-based composite development.

4.2 Experimental Section

Synthesis of porous MXene. The porous $Ti_3C_2Cl_2$ was prepared using an eutectic etching method previously reported by our group.[265] Specifically, Ti_3AlC_2 precursor was mixed with solid NaCl and $ZnCl_2$ in the molar ratio of 1:9:6. Then the mixture was annealed at 550 ºC for 5 h, followed by 1 M HCl washing and freeze-drying.

Synthesis of CoHCF and CoHCF/porous MXene composites. Firstly, $KCoFe(CN)_6$ was synthesized by simple co-precipitation of 0.1 M $K_3[Fe(CN)_6]$ and 0.1 M $Co(NO_3)_2$ in 40 mL DDI water. After stirring for 24 h in room temperature, the precipitates were washed by DDI water for several times. Then the products were dried in oven at 80 ºC overnight. $CoFe(CN)_6$ (CoHCF) was achieved by extracting K atoms from $KCoFe(CN)_6$ via electrochemical process as reported.[170] $KCoFe(CN)_6$ was applied as cathode, with 15 M $ZnCl_2$ and Zn foil as electrolyte and anode. $CoFe(CN)_6$ was formed with cut-off voltage as 1.9 V. CoHCF/M-1% and CoHCF/M-2% were prepared similarly with 10 mg and 20 mg porous $Ti_3C_2Cl_2$ stir with $Co(NO_3)_2$ for 1 h at room temperature prior to precipitation process.

Material Characterization. X-ray diffraction results (XRD, Rigaku Miniflex 600) were achieved with graphite monochromator and Cu Kα radiation as X-ray source (λ=1.5406Å). The morphology and crystal structure of CoHCF and CoHCF/MXene composites were obtained by Scanning Electron Microscope (SEM, Zeiss ULTRA) and Transmission Electron Microscopy (TEM, JEOL, JEM-2010, 200 kV). The surface area and pore structure were studied by N_2 adsorption-desorption measurements on the surface area analyzer Quantachrome Instruments QuadraSorb SI4, the surface area were calculated using the BET theory and the pore size distributions were obtained via the Barrett-Joyner-Halenda (BJH) model on the desorption isotherm. Elemental and oxidation state information of CoHCF and CoHCF/M-1% was collected by X-ray photoelectron spectra (XPS, Thermal Scientific K-Alpha X-ray Photoelectron Spectrometer System) and the binding energies were calibrated by C 1s of 284.5 eV. X-ray absorption spectroscopy (XAS) measurements on Co and Fe K-edge spectra were collected at Canadian Light Source on the hard X-ray microanalysis (HXMA) beamline and Soft X-ray Microcharacterization Beamline (SXRMB). The data were then analyzed using Athena and Artemis software packages. The elemental composition of the $CoFe(CN)_6$ material in the composites were confirmed by inductively coupled plasma atomic emission spectrometry (ICP-AES). The water content in the synthesized materials were determined by thermogravimetry (TG) with TGA Q500 thermogravimetric analyzer from room temperature to 500 ºC at a rate of 2 ºC/min in nitrogen.

Electrochemical Measurement. Typically, the active materials were mixed and sonicated with multiwalled carbon nanotube in a mass ratio of 3:1 in ethanol. The solutions were then filtrated onto a glass fiber sheet, which was then left to dry in oven at 80 °C overnight. Prior to

assembly, they were punch into disks in diameter of 12 mm, and the active material loading can range between 1.2-1.5 mg cm^{-2}. The battery was then fabricated by pairing these disks with Ti foil current collector and Zn foil anode. Glass microfiber filter membrane with diameter of 15 mm and 15 M $ZnCl_2$ electrolyte were used as separator and electrolyte. Galvanostatic charge/discharge (GCD), cyclic voltammetry (CV), cyclability tests and electrochemical impedance spectroscopy (EIS) measurement were conducted on electrochemical station (BioLogic VMP-300).

4.3 Results and Discussion

4.3.1 Material Characterization

The porous $Ti_3C_2Cl_2$ MXene was first synthesized following a method previously reported by our group, proper replication of the process is confirmed by scanning electron microscopy images of the products (**Figure 4-1**).[265] The CoHCF/MXene-1% composite was prepared through passive adsorption of the $Co(NO_3)_2$ precursor onto the negatively charged porous MXene surface,[266] followed by slow addition of $K_3Fe(CN)_6$ to trigger the nucleation mechanism (**Figure 4-2a**). The partial negative charges on the chlorine functionalized MXene surface is anticipated to enact a repulsion force to anions in the solution, which in turn would induce anisotropic growth of CoHCF to form nanotubes.[267-269] SEM image of composite prepared with a MXene weight percent of 2 (CoHCF/M-2%) shows short CoHCF nanotubes with sizes around 400 nm seeded directly on the MXene nanosheet (**Figure 4-2b**). When further lowering the MXene weight percent to 1, the CoHCF is observed to grow into close-packed bundles of nanotubes on the MXene surface with length of around 3 μm (CoHCF/M-1%, **Figure 4-2c**).[270] This change is attributed to the higher amount of precursor available for crystal growth in the CoHCF/M-1% synthesis solution

due to reduced seeding/adsorbing sites. Furthermore, the nanotube morphology contrast distinctively against the pure CoHCF nanospheres produced through uniform nucleus stabilization and isotropic growth in standard co-precipitation (**Figure 4-2d**),[271] indicative of altered CoHCF crystal growth mechanism due to the presence of MXene in the synthetic process. XRD patterns of all three samples exhibit individual peaks corresponding to the (200), (220), (400) and (420) diffractions of CoHCF, which forms face-centered cubic lattice in three-dimensional cyanide-bridged structure (**Figure 4-2e**).[170] The increased (400) crystal facet observed on the composite materials indicates preferred growth along the <100> crystallographic orientation,[272, 273] verifying the hypothesis regarding the influence of MXene surface charge on the CoHCF growth patterns. Meanwhile, the (002) peaks position of MXene remain largely unchanged in the two composite samples, suggesting minimal lattice expansion from the synthetic process.

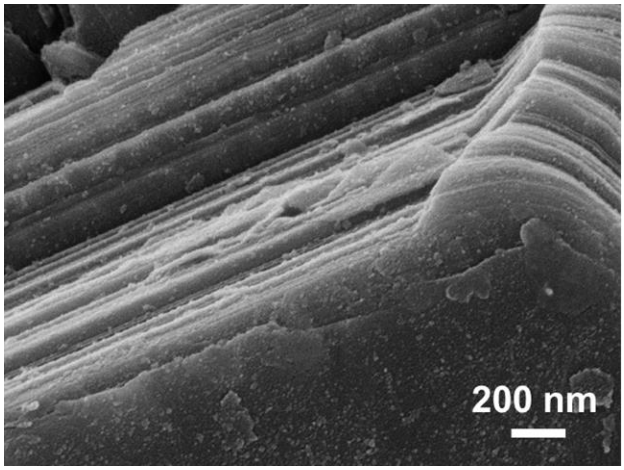


Figure 4-1. SEM image of porous $Ti_3C_2Cl_2$.

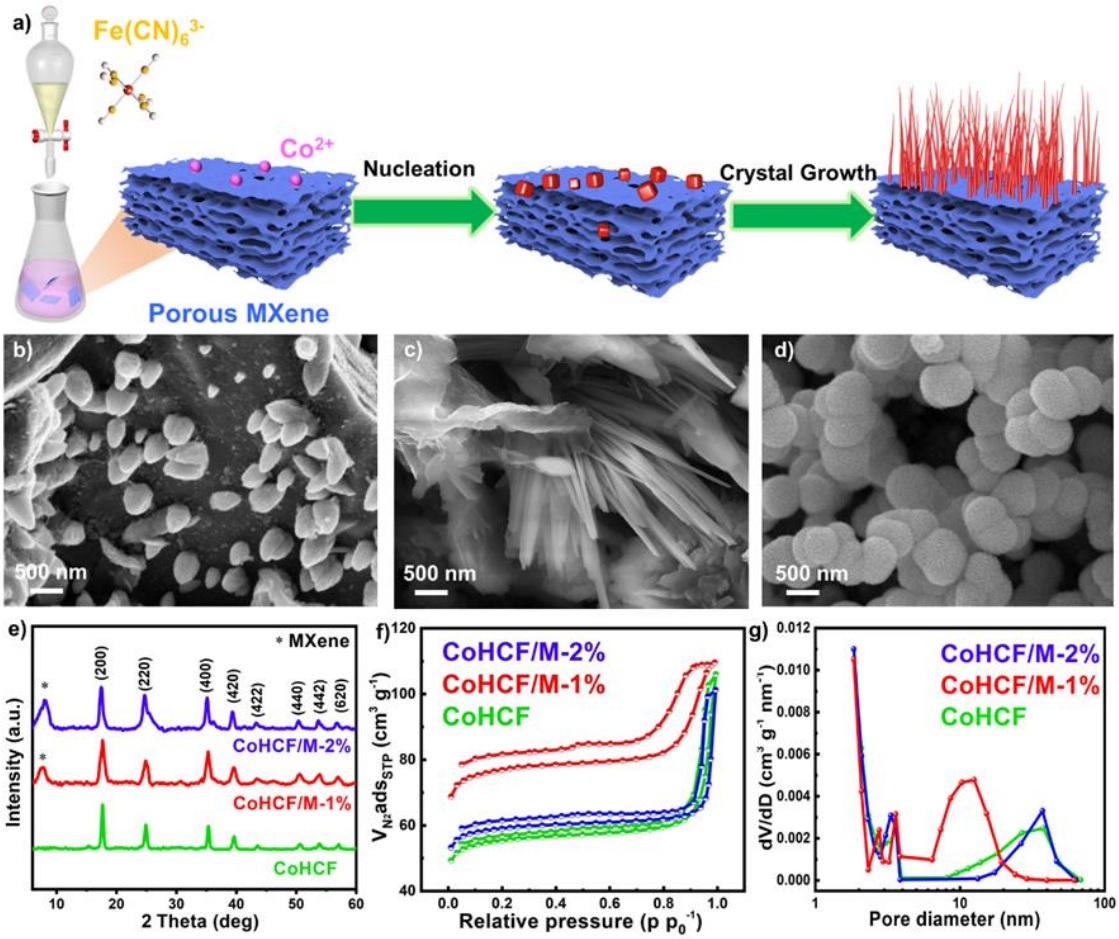


Figure 4-2. a) Scheme of CoHCF/M-1% synthesis process. b)-d) SEM images, e) XRD, f) N_2 adsorption–desorption isotherms and g) pore size distribution data of CoHCF/M-2%, CoHCF/M-1% and CoHCF.

Nitrogen adsorption isotherms of the three samples shown in **Figure 4-2f** reveal points of similarities between the pure CoHCF and CoHCF/M-2%, and their calculated Brunauer-Emmett-Teller (BET) surface area of 171 and 184 m^2 g^{-1} are also relatively close in value. In contrast, CoHCF/M-1% exhibits a much more distinct hysteresis loop between the adsorption and desorption isotherm that is commonly associated with mesoporosity.[274] Its BET surface of 237.9

m^2 g^{-1} is also the highest among all three samples. Pore size distribution analysis of pure CoHCF shows concentrated formation of pores in the range below 3.6 nm and above 20 nm (**Figure 4-2g**). This is again comparable to the CoHCF/M-2% distribution that exhibits high pore concentration above 20 nm, except for the additional pore volume around 3 nm contributed by the porous MXene (**Figure 4-3**). While CoHCF/M-1% contains primarily mesopores with sizes between 3.6 to 30 nm plus the < 3.6 nm pores. The high resemblance between the pore size distribution results of pure CoHCF and CoHCF/M-2% composite may be explained by their relatively similar Co compound particle sizes and morphology, whereas significantly increased amount of mesopores with sizes between 3.6-30 nm found in CoHCF/M-1% likely arise within the nanotube structures and spaces between the nanotube bundles. As CoHCF/M-1% possesses largest surface area, it has ability to boost electrochemical reaction kinetics by providing ample intercalation sites for Zn^{2+} and offering sufficient contact with electrolyte.[269] Meanwhile, the abundant pores permit the shortened diffusion pathways for Zn^{2+} transport,[275] enabling superior capacity of CoHCF/M-1% during charge/discharge process.

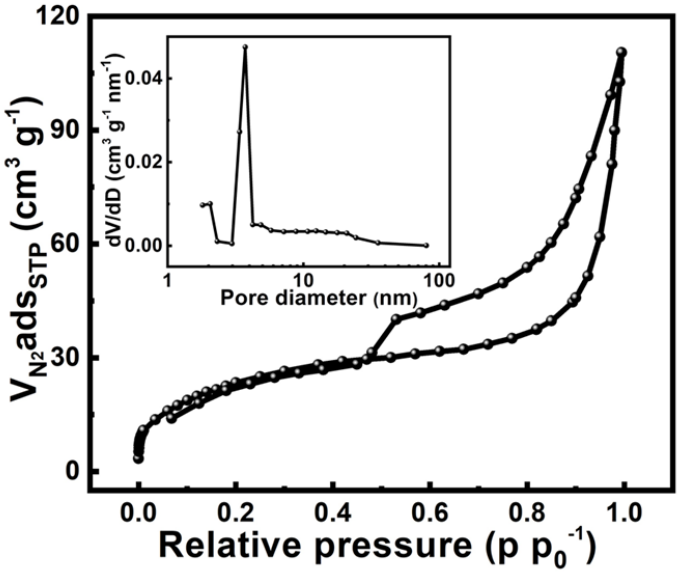


Figure 4-3. N_2 adsorption–desorption isotherms and pore size distribution for porous MXene.[265]

Figure 4-4a shows a transmission electron microscopy (TEM) image of CoHCF/M-1%, in which, it can be clearly observed that mesopores are distributed along the CoHCF nanotubes. While scanning transmission electron microscopy (STEM) image of the composite capturing both the CoHCF nanotube and MXene nanosheet shows well retainment of the in-plane microporosity in the MXene after the synthetic process (**Figure 4-4b**). These align with the BET data interpretation, confirming the origins of porosity measured in CoHCF/M-1%. High-resolution transmission electron microscopy (HRTEM) of the yellow high-lighted area in **Figure 4-4c** reveals the (100) lattice fringe with lattice distance of 0.26 nm for the highly crystalline MXene nanosheet. While in the red highlighted area, the 0.228 nm lattice fringe representing the (420) plane of CoHCF can be observed (**Figure 4-4d**), matching well with the CoHCF/M-1% XRD pattern.

Gaussian deconvolution of the high-resolution Co $2p_{3/2}$ X-Ray photoelectron spectroscopy (XPS) spectra of pure CoHCF and CoHCF/M-1% both identify two major peaks located at 781.5

eV and 786.1 eV, representing the Co^{3+} adsorption and satellite feature, respectively (**Figure 4-4e**).[170] While more precise comparison of the two spectra further reveals an additional weak peak at 782.7 eV in CoHCF/M-1% that is commonly assigned to Co^{2+}.[276] Meanwhile, the Fe $2p_{3/2}$ XPS adsorption of the two materials at 709.8 eV show minimal variations in peak shape and energy position, confirming their unchanged 3+ valence state and their irrelevance in the reduction of Co valence state (**Figure 4-4f**).[170] Furthermore, deconvolution of the CoHCF/M-1% Ti *2p* XPS resulted in three isolated peak pairs, which includes the Ti-C(I) peaks at 454.2 eV (460.3 eV), the Ti-C(II) peaks at 455.6 eV (461.7eV) and the Ti-Cl peaks 458.2 eV (463.8 eV) (**Figure 4-5a**). When compared to the pure MXene sample (**Figure 4-5b**), proportion between Ti-C(II) versus Ti-C(I) is increased, indicating oxidation of the MXene central layer Ti after the composition. These results combined point to the fact that Co-C bonds have likely formed between the CoHCF and MXene nanosheet, these would explain presence of Co^{2+} via bonding with the less electron withdrawing C and the increased amount of oxidized Ti is caused by formation of the Co-C-Ti configuration that puts them against the more electronegative metal element of Co. Benefited from the interfacial interaction and the metallic conductivity of MXene, CoHCF/MXene composites are expected to facilitate the ion and electron transport pathways during electrochemical reactions and exhibit improved rate capability.[277] Moreover, Co-C chemical bonds have potential to alleviate volume change and irreversible structural transformation during repeated intercalation/deintercalation process, thus enhancing the stability of the composite.

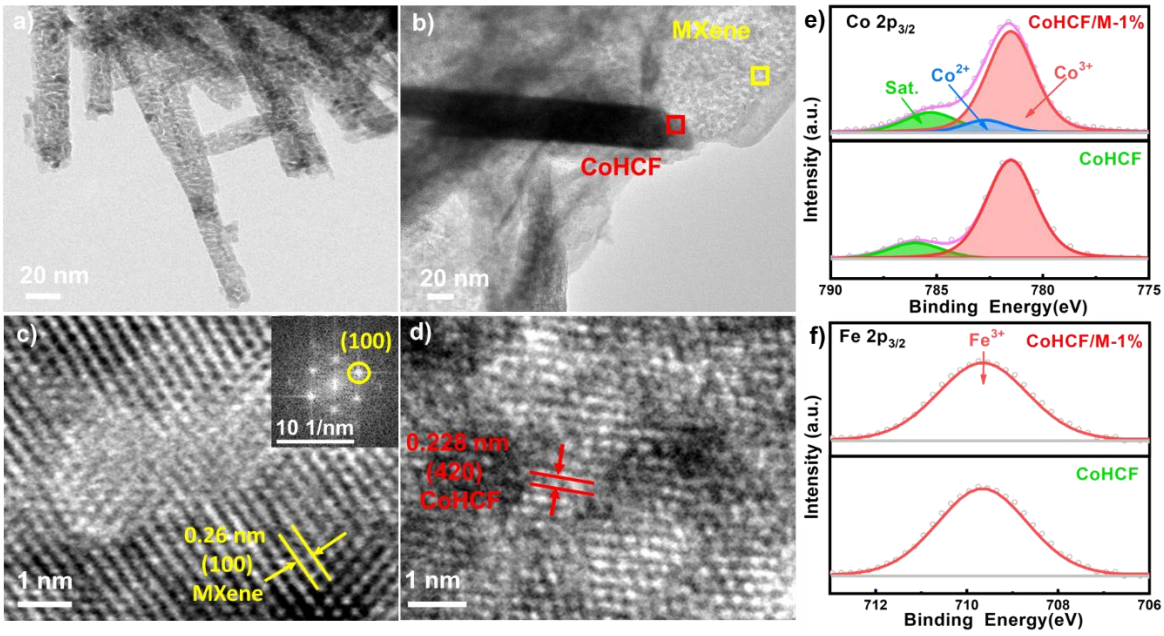


Figure 4-4. a)-d) TEM, STEM and HR-TEM images of CoHCF/M-1%. e) Co2$p_{3/2}$ and f) Fe 2$p_{3/2}$ XPS spectra of CoHCF and CoHCF/M-1%.

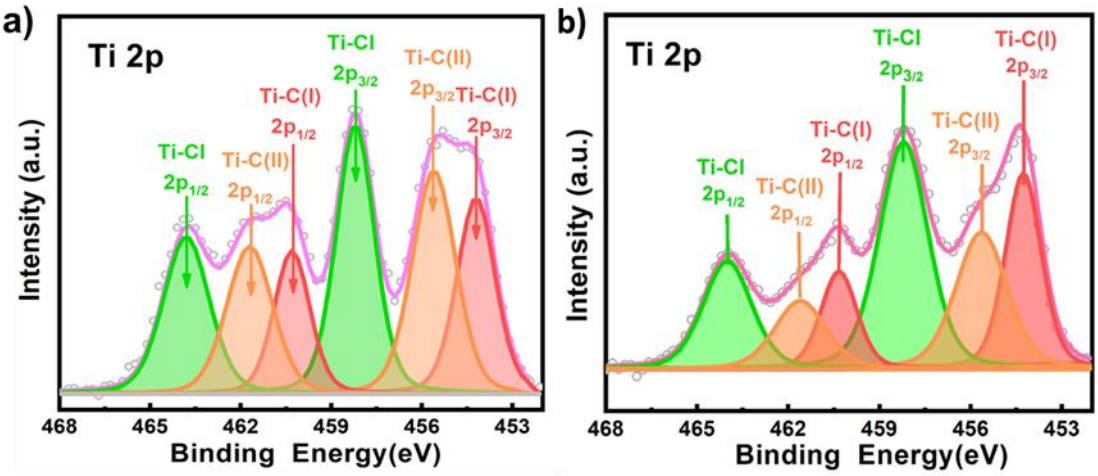


Figure 4-5. Ti 2p XPS spectra of a) CoHCF/M-1% and b) porous MXene.[265]

Insight into the electronic state and atomic structures of the composite materials were also obtained through comparing the Co K-edge X-ray absorption near-edge structure (XANES) spectra of the materials against CoO and Co_2O_3 References (**Figure 4-6a**). As shown, the absorption edge position (E_0) of CoHCF is located at 7728.6 eV, which is identical to the edge position of the Co_2O_3 reference that contains predominately low spin Co^{3+}.[278, 279] In comparison, the E_0 of both CoHCF/M-1% and CoHCF/M-2% are at a slightly left-shifted position of 7727.8 eV, indicating lower oxidation state. Comparison of pre-edge peaks near 7722.1 eV, which are associated with the Co 1*s* → 3*d* transition, also reveals that CoHCF has a clearly more apparent peak when compared to the CoHCF/MXene composites. Fading of the pre-edge peak generally reflects increased Co T_d symmetry, and in this case would also imply higher proportion of fully saturated Co centers and less defective CoHCF crystal structure.[278, 279] To further analyze changes in the Co local coordination environment induced by compositing with MXene, extended X-ray absorption fine structure (EXAFS) are measured and the k^3-weighted Fourier-transformed (FT) spectra are presented in **Figure 4-6b**. The pure CoHCF exhibits three distinct features at 1.62 Å, 2.73 Å and 4.71 Å, which matches previously reported distances of neighboring cyanide N, cyanide C and Fe near the Co octahedral site.[278, 279] Similarly, these three features are also found in CoHCF/M-1% and CoHCF/M-2%, but they are notably narrower than the peaks observed in pure CoHCF. Such changes reflect tightened distribution of the ion distances in the local environment and are interpretated in a larger scale as increased long-range ordering of the CoHCF crystalline. The increased peak intensity also leads to the same inference as they imply higher Co coordination numbers with neighbouring atoms.[166, 259, 262, 263, 280, 281] Meanwhile, the Co-N bond distance in the composites are measured to extend above 1.70 Å, whereas the Co-C distance are

reduced to near 2.40 Å. The former is mainly induced by the previously observed reduction of the Co ions that adds electron density into the antibonding e_g* orbitals.[279] While the latter can be explained by the newly formed Co-C connection between CoHCF and porous MXene that are drastically shorter than the Co and cyanide C distance within the CoHCF crystal, which weighs down the average Co-C coordination distance in the composite. Fe k-edge XANES spectra of the samples were also investigated to analyze changes in the Fe atomic conditions induced by composition with the MXene nanosheet (**Figure 4-6c**). In alignment with the XPS results, E_0 of the three samples show minimal variations as they are all located at almost the identical position of 7126.6 eV, which matches precisely with the E_0 of the Fe_2O_3,[282] confirming the 3+ Fe average oxidation state for the bulk of the CoHCF crystals. Moreover, the composite pre-edge peaks at 7116.5 eV are found to be less intensive and less distinctive when compared to the pure CoHCF counterpart. The improved symmetry points to the same conclusion made with the Co XANES analysis that CoHCF crystals in the composite are less defective. Meanwhile, Fe K-edge EXAFS R-space spectra of all samples show three distinct peaks corresponding to the Fe-C, Fe-N and Fe-Co coordination distances (**Figure 4-6d**).[283] The peaks show minimal variations in position, matching well with the largely unchanged Fe oxidation state observed in both XPS and XANES. The consistent Fe-C and Fe-N distances among the samples also support the claim on Co-C bonds formation between the CoHCF and MXene nanosheet given their direct correlation with the Co-cyanide bridge.

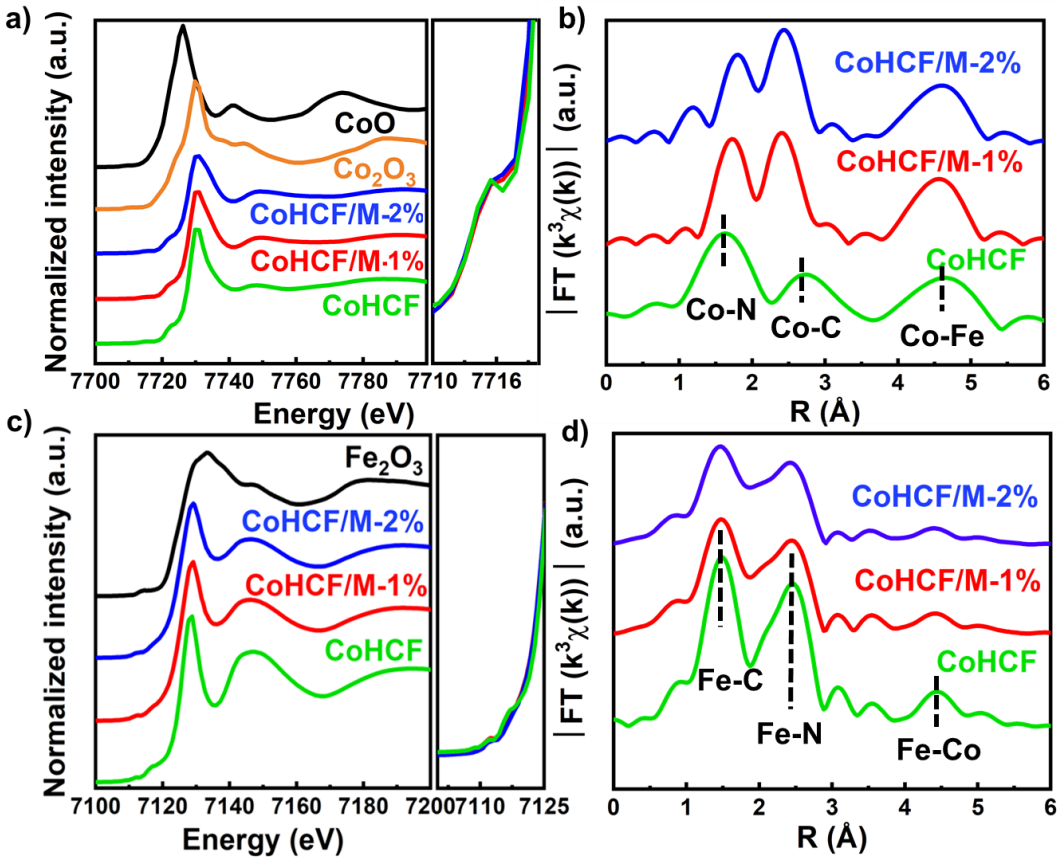


Figure 4-6. a) Normalized Co K-edge XANES spectra, b) Co K-edge EXAFS R-space spectra, c) normalized Fe K-edge XANES spectra, d) Fe K-edge EXAFS R-space spectra of CoHCF, CoHCF/M-1% and CoHCF/M-2%.

Thermogravimetric analysis (TGA) performed at 2°C/min in air show three separate regions of weight loss (**Figure 4-7**). In the first section between 30 to 120°C, the weight change is primary caused by evaporation of surface or adsorbed water, while weight lost in the second section between 120 to 200°C represent removal of interstitial water molecules that reside near the structure defects.[284] Lastly, the weight loss above 200 °C is attributed to the decomposition of the cyanide bridge in the CoHCF structure. From the TGA graph, the pure CoHCF nanosphere is

measured to contain 16.6 wt.% of interstitial water, while the water content in CoHCF/M-1% and CoHCF/M-2% are identified to be 13.5 and 11.1 wt.%, respectively. Given that interstitial water content is proportional to the number of structural vacancies, this indicates reduced defect abundancy in the composite materials.[285] Meanwhile, composition analysis of the CoHCF components by inductively coupled plasma atomic emission spectroscopy (ICP-AES) reveals a Fe/Co atomic ratio of 0.78 for the pure CoHCF, while the composites achieve higher Fe/Co ratio of 0.89 and 0.93 (**Table 4-1**). Upon normalizing to the Co content, the element and defect proportions in CoHCF, CoHCF/M-1% and CoHCF/M-2% are determined to be $Co[Fe(CN)_6]_{0.78}\square_{0.22}\bullet 2.5H_2O$, $Co[Fe(CN)_6]_{0.89}\square_{0.11}\bullet 2.1H_2O$ and $Co[Fe(CN)_6]_{0.93}\square_{0.07}\bullet 1.7H_2O$, respectively. (□ stands for $[Fe(CN)_6]^{3-}$vacancy) These quantitative analysis results align with the X-ray spectroscopic analyses on reduced CoHCF vacancies in the composite samples, which provides more intercalation spaces for Zn^{2+}, and thus enabling enhanced discharge capacity. Meanwhile, the reduced water content allows CoHCF/MXene an ultra-stable structure, ensuring long cycle life when used as ZIBs cathode.

The mechanism of defect reduction by MXene host is proposed here. Pre-adsorption of Co^{2+} onto the MXene nanosheets is particularly important for regulating the speed of agitation and segregating molecules, as interactions between Co^{2+} and the MXene surface functional groups alter its interaction with the incoming $Fe(CN)_6^{3-}$ and surrounding water molecules, which enforces steric hindrance toward the water molecules and minimizes their entry into the CoHCF crystal.[260, 281, 284] This distinctive structure has the following advantages. Firstly, with the buffer of MXene, such highly crystalline structural arrangement with large surface area would free up the previously occupied tunnels to enable extensive and rapid access toward more intercalation sites for the Zn^{2+}

ions, making it possible to boost capacity. Moreover, the enhanced overall conductivity enables faster electron transport speed in the composite, ensuring a higher rate capability and lower resistance. Furthermore, with significantly lowered water content and existed Co-C chemical bonds, the composite shows great potential in preserving the integrity of the crystalline structure during repeatedly Zn^{2+} intercalation/deintercalation. Therefore, the CoHCF/MXene composites are expected to perform excellent electrochemical performance during charge/discharge process.

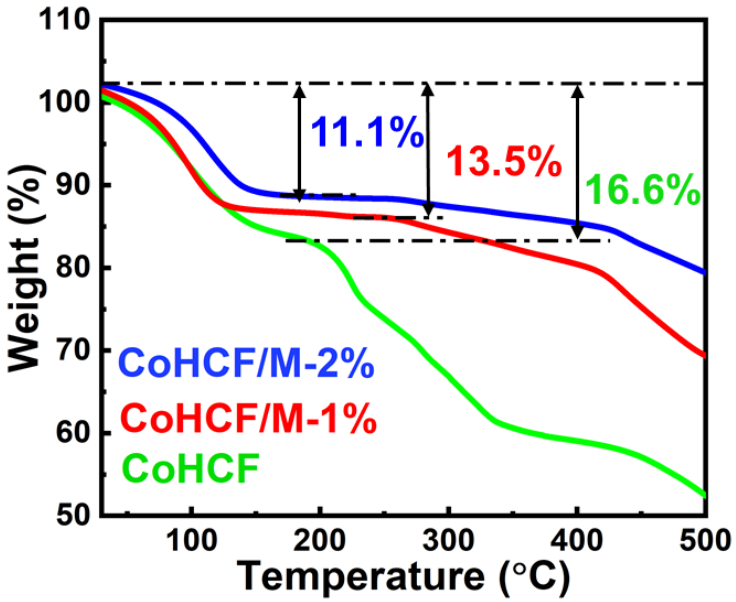


Figure 4-7. TGA plots of CoHCF, CoHCF/M-1%, CoHCF/M-2%.

Table 4-1. ICP results of CoHCF in composites

Sample	Atomic%		Relative atomic ratio		H_2O molecules per host lattice (wt.%)
	Co	Fe	Co	Fe	
CoHCF	57.4	42.6	1.00	0.78	16.6

CoHCF/M-1%	54.1	45.9	1.00	0.89	13.5
CoHCF/M-2%	53.2	46.8	1.00	0.93	11.1

4.3.2 Electrochemical Performance

To verify the influences of CoHCF morphology and crystal structure modifications on their electrochemical performance, the as-prepared samples were evaluated as cathode in half cells fabricated with zinc foil anode and 15 M $ZnCl_2$ electrolyte. Galvanostatic charge and discharge profiles of these half cells between 0.7 and 2.0 V at 0.1 A g^{-1} show that CoHCF/M-1% achieves the highest discharge plateaus of 1.95 and 1.82 V among all three samples (**Figure 4-8a**). It also achieves a capacity of 197.0 mAh g^{-1}, which exceeds the 179.2 mAh g^{-1} of CoHCF/M-2% and 145.6 mAh g^{-1} of pristine CoHCF nanospheres. The porous MXene was also measured in a half cell for comparison, and it delivers 57.5 mAh g^{-1} with primarily capacitive contributions, verifying its minimal contribution to capacities delivered above 1.8 V. The significantly improved performance measured with CoHCF/M-1% is the combined results of elevated surface area provided by the nanotube morphology and reduced defect quantity in the CoHCF lattice. The former increase the site accessibility and mass diffusion to achieve high capacity utilization, while the latter increases number of suitable intercalation site and establishes platform that are more suitable for Zn^{2+} ion diffusion.[281] Comparison between pure CoHCF and CoHCF/M-2% with similar surface area also supports the claim on positive influence of reduced structure defects, as their performance variation would primarily be induced by differences in the CoHCF crystal structure. CoHCF/M-1% also demonstrates strong rate capability, achieving 197.0, 180.2, 172.9,

157.5 mAh g^{-1} at the currents of 0.1, 0.5, 1.0, 2.0 A g^{-1}, respectively (**Figure 4-8b**). Its 50 mV voltage drop after increasing the current density twenty times from 0.1 to 2.0 Ag^{-1} is also relatively low. Among three samples, CoHCF/M-1% shows stable crystal structure as its capacity returns to initial value after experiencing high rate cycles (**Figure 4-8c**). Compared to CoHCF, the outstanding rate capability of CoHCF/M-1% is owing to the low water content and improved conductivity with the addition of MXene which help to facilitate the Zn^{2+} ion diffusion.[267] Additionally, all three samples show minimal performance lost upon returning to the initial current, confirming their tolerance toward high current cycling. As for their long-term cycling, CoHCF/M-1% maintains 94.4% of its initially capacity after 3000 cycles of operation at 2.0 A g^{-1}, while CoHCF/M-2% shows decent capacity retention of 86.1% with majority of the lost occurred in the early stages (**Figure 4-8d**). In contrast, the pure CoHCF experiences continuous capacity lost over the 3000 cycles and only retains 72.5% of its capacity at the end of the test. The improved cycling stability of the CoHCF/MXene composites is attributed to their lessen interstitial water content and unique Co-C bonds, which increase their tolerance toward structural collapse upon repeated Zn intercalation/extraction.[260, 286] Nyquist plots of the three samples calculated from electrode impedance spectroscopy (EIS) measurements all show a single semicircle in the mid-frequency range associated with charge-transfer resistance and a oblique line in the low-frequency area (**Figure 4-8e**).[287] Among them, CoHCF/M-2% exhibits the lowest series resistance owing to its higher content the conductive MXene. While CoHCF/M-1% display the smallest semicircle, indicative of its fastest reaction kinetics enabled by high active site accessibility through its porous nanotube morphology.[264] Comparison between this work and reported PBA cathodes for Zn-ion batteries reveal that the remarkable electrochemical performance of CoHCF/M-1% (**Table 4-2**).

As expected, the low vacancies, high surface area, unique Co-C bonds and enhanced conductivity features of CoHCF/M-1% guaranties abundant intercalation sites, stable crystal structure and fast Zn^{2+} diffusion.

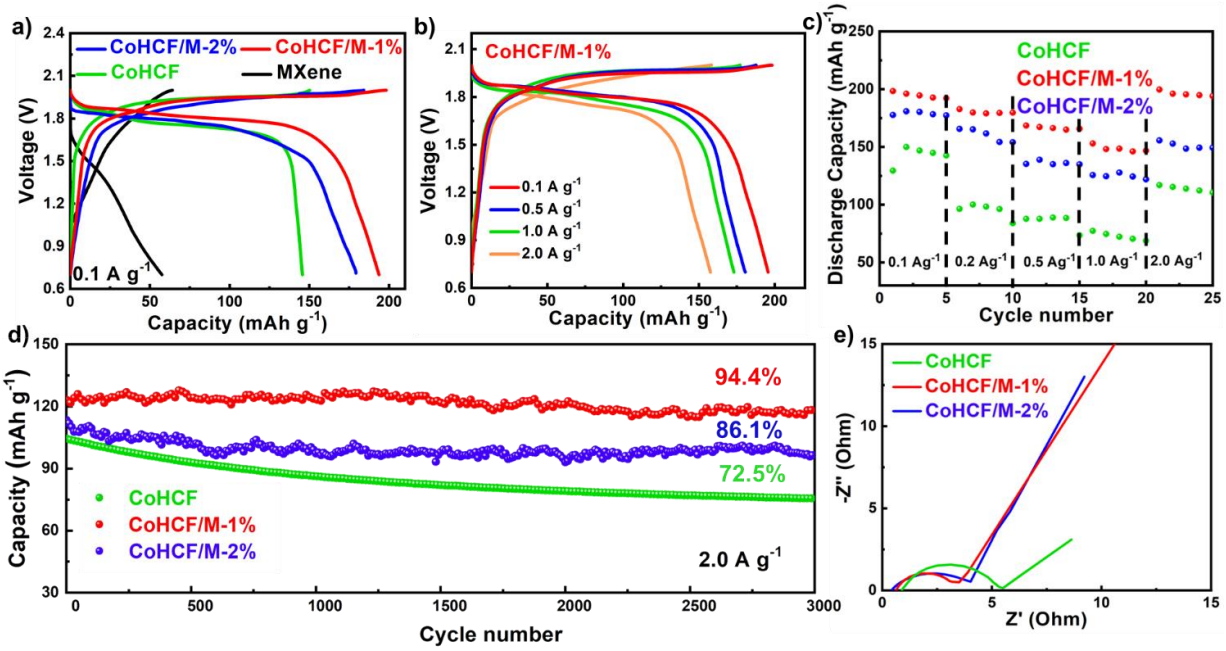


Figure 4-8. a) Galvanostatic charge and discharge curves, c) rate capability and d) long term cycling performances at 2.0 A g^{-1} of CoHCF, CoHCF/M-1% and CoHCF/M-2%. b) GCD curves of CoHCF/M-1% at different rates. e) EIS plots of ZIBs using CoHCF, CoHCF/M-1% and CoHCF/M-2% as cathodes.

Table 4-2. Electrochemical performance comparison of CoHCF/MXene and other Prussian blue analogues ZIBs cathode reported in literature.

Cathode material	Voltage window (vs Zn/Zn^{2+})	Average operating voltage (vs Zn/Zn^{2+})	Specific capacity (mAh g^{-1})	Cycle performance
ZnHCF[168]	0.8-2.0 V	1.73V	66.5 at 0.06 A g^{-1}	80% after 200 cycles at 0.3 A g^{-1}
ZnHCF@MnO_2[288]	1.4-1.9 V	1.68 V	118 at 0.1 A g^{-1}	77% after 1000 cycles at 0.5 A g^{-1}
CuHCF[169]	0.6-1.3 V vs. SHE	1.73 V	53 at 0.06 A g^{-1}	96.3% after 100 cycles at 0.06A g^{-1}
CuHCF[289]	1.4-2.3 V	1.8 V	70.4 at 0.3 A g^{-1}	76.5% after 1000 cycles at 1.8 A g^{-1}
NiHCF[290]	0.9-1.9	1.5 V	75 at 0.1 A g^{-1}	81% after 1000 cycles at 0.5 A g^{-1}
CoHCF[170]	0.7-2.0 V	1.75 V	173.4 at 0.3 A g^{-1}	100% after 2200 cycles at 3 A g^{-1}
NaFeHCF[291]	0.8-2.0 V	1.3 V	73.6 at 0.25 A g^{-1}	92.1% after 2000 cycles at 2 A g^{-1}
CoHCF/MXene (This work)	0.7-2.0 V	1.8 V	197 at 0.1 A g^{-1}	94% after 3000 cycles at 2.0 A g^{-1}

4.3.3 *Ex-situ* Characterization

To trace the source for the improved performances, *ex-situ* Co $2p_{3/2}$ and Fe $2p_{3/2}$ XPS spectra of CoHCF/M-1% at its discharged and charged states were collected for quantitative analysis (**Figure 4-9a, b**). As shown, when CoHCF/M-1% is discharged to 0.7 V vs. Zn/Zn^{2+} at 0.1 A g^{-1}, 60.0% of the Fe^{3+} is reduced and the Co^{2+} proportion is boosted from 9.9% to 30.2%.

Both redox transitions show high reversibility, as the Co^{2+} percentage returned to near its initial state at 10.4% and the Fe^{3+} adsorption completely disappears when the electrode is recharged to 2.0 V. In contrast, only 10.8% of the Co^{3+}/Co^{2+} and 32.2% of the Fe^{3+}/Fe^{2+} redoxes are activated when pure CoHCF is discharged to the same condition (**Figure 4-9c, d**). Reversibility of this Fe redox reaction is also poor, since 27.6% of the Fe remained with an oxidation of 2+ when CoHCF is fully charged back to 2.0 V, signaling inability to extract intercalated Zn^{2+} ions and permanent capacity lost. Further Zn $2p_{3/2}$ XPS results also reveal more successful Zn^{2+} reversibility in CoHCF/M-1% compared to CoHCF (**Figure 4-9e**). Building on the XPS analysis, discrepancies between the two samples in their *ex-situ* XRD analysis are also investigated (**Figure 4-9f & 4-10**). For CoHCF/M-1%, it experiences clear crystal phase transition upon Zn intercalation during discharge, its (200) peak gradually loses intensity and completely disappears when the voltage is lowered to 0.7 V. During this process, a new peak with strong intensity at 17.6° appears when the battery is discharged to 1.8 V, which corresponds to the (011) plane. The phase transition is reversed upon the cell are recharge, with the (200) peak of 18.4° reappearing at 1.7 V, and the (011) peak completely disappear once the half cell is fully recharged to 2.0 V. Positioning of the (200) peak after discharge and charge process shows minimal variation and the peak is also notably narrower, revealing the highly reversible phase transition of CoHCF/M-1%. Similarly, the pure CoHCF also experiences the phase transition with a fading (200) peak and an emerging (011) peak during discharge (**Figure 4-10**). However, the (200) peak failed to return to its initial position when recharged, suggesting lattice space shrink that is likely caused by attraction force from Zn^{2+} ions remained in the crystal structure. These *ex-situ* characterizations explain the improved capacity of CoHCF/M-1% as the more feasible intercalation sites offer more redox reactions.

Meanwhile its lower water content and Co-C bonds well preserve the crystallinity structure of CoHCF, avoiding capacity loss caused by structure collapse.[281]

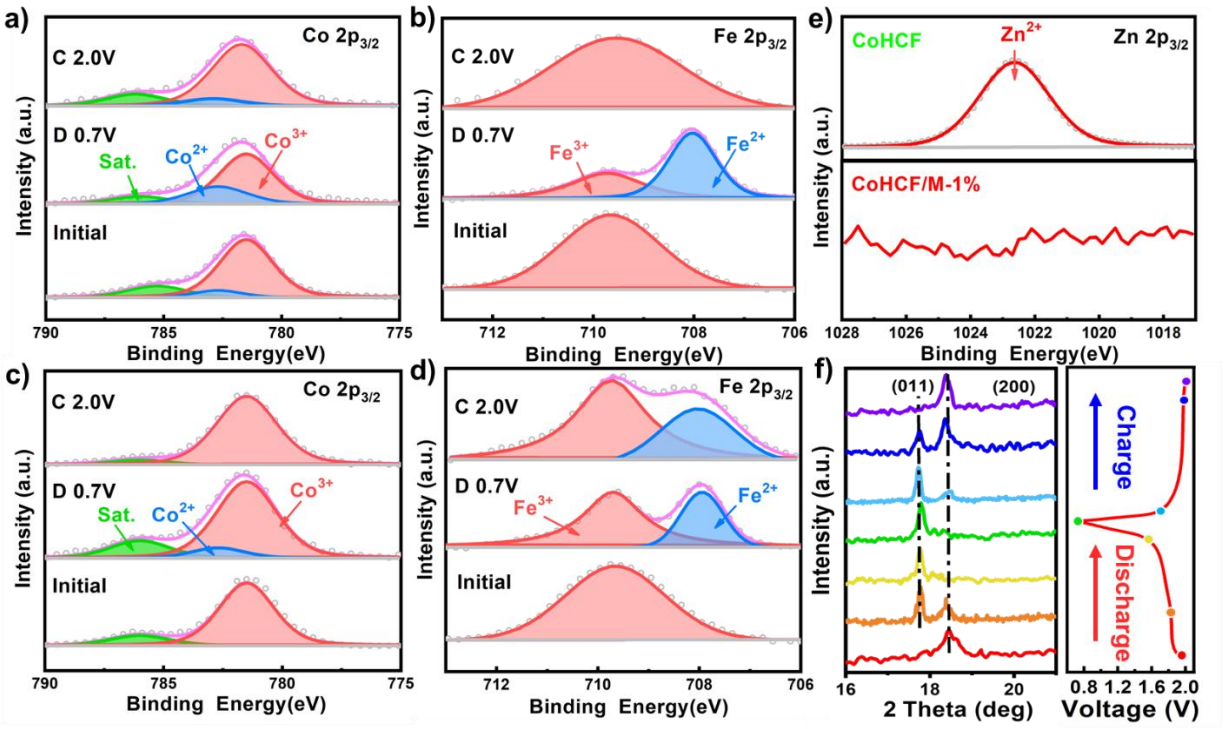


Figure 4-9. *Ex-situ* Co $2p_{3/2}$ XPS spectra of a) CoHCF/M-1%, c) CoHCF and Fe $2p_{3/2}$ XPS spectra of b) CoHCF/M-1%, d) CoHCF at the initial state, discharged to 0.7 V and recharged to 2.0 V vs. Zn/Zn^{2+}. e) Zn $2p_{3/2}$ XPS spectra of CoHCF (top) and CoHCF/M-1% (bottom) after cycling. f) *Ex-situ* XRD patterns of CoHCF/M-1% at selected cycling potentials.

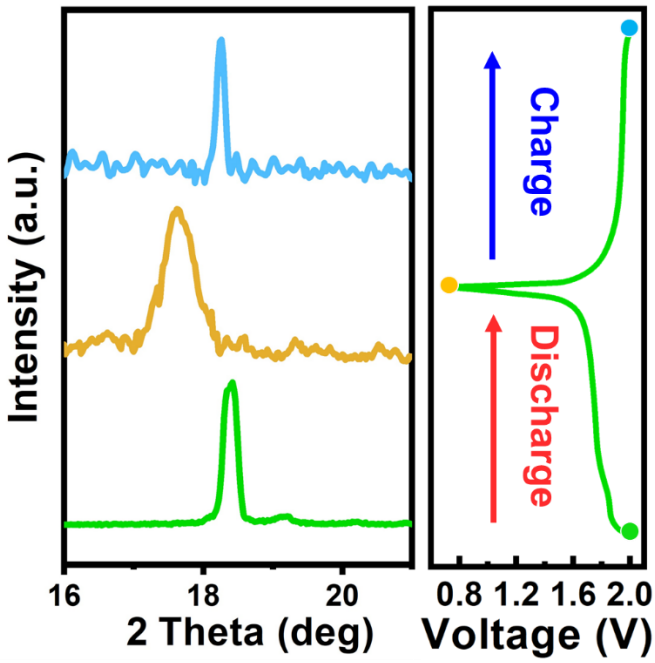


Figure 4-10. *Ex-situ* XRD plots of CoHCF before and after cycling.

4.4 Conclusion

To summarize, an effective strategy is developed to synthesize low vacancy CoHCF nanotubes on porous MXene nanosheets as superior composite for ZIB cathode application. Specifically, the negative surface charges on the MXene nanosheets are utilized to induce growth of CoHCF nanotube, while influencing the Co^{2+} interactions with CN^- ligands and water molecule to form crystals with well-established structure. This is discovered to improve tolerance toward Zn^{2+} insertion/extraction and reversibility of the redox transition. Benefiting from the high specific surface area, enhanced conductivity and reduced structural defects, the CoHCF/M-1% composite achieves a high discharge capacity of 197 mAh g^{-1} at 0.1 A g^{-1} and only lost 5.6% of its initial capacity after 3000 cycles at 2.0 A g^{-1}. This work demonstrates a facile method to induce

modulated growth of high crystalline PBA on porous MXene as stable composite electrode, and it is of high practical value for investigations in a wide range of energy storage application.

Chapter 5 Porous Cl-terminated MXene Promoted Horizontal Growth of Zn Electrodeposition Towards Non-Dendritic Zn Anode

5.1 Introduction

Metal anodes featured with high theoretical energy density and reversibility toward electrochemical process are of great importance for rechargeable batteries, but numerous obstacles exist prior to fulfillment of their complete potentials.[178, 292, 293] Among the different metal anodes, zinc (Zn) is extensively investigated due to its high theoretical capacity (820 mAh g^{-1}), low redox potential (−0.76 V *vs.* standard hydrogen electrode), environmental benignity and intrinsic safety.[181, 186, 294] However, its propensity to participate in side reactions such as self-corrosion and hydrogen evolution reaction often results in poor Coulombic Efficiency (CE).[179, 256] More importantly, dendrites formation during repeated cycling can pierce the separator and cause internal short circuiting that leads to complete battery failure, severely hampering the commercialization of rechargeable zinc-ion batteries (ZIBs).[127, 179, 186, 295, 296]

One possible solution for the dendritic issue is through the optimizing the nucleation and growth by finetuning the Zn anode surface atomic structure.[187, 294, 297, 298] Particularly, the (0002) crystal plane has been identified to induce even charge distribution in the electrolyte-electrode interface, which encourages smooth and parallel deposition.[299, 300] This contrast against the other common crystal planes of $(10\bar{1}0)$ and $(10\bar{1}1)$ that cause inhomogeneous interfacial charge distribution and uneven Zn^{2+} flux near the electrode surface, leading to rapid dendrites formation.[294, 299, 301, 302] The difference in cycle life between the preferred (0002) and the other crystal planes have been reported to exceed five folds, as the (0002) plane was also modeled to

exhibit lower surface energy that ensures electrochemical stability.[299, 303] Other research efforts encompassing electrolyte modifications and surface engineering have also been devoted with corresponding positive and drawbacks.[304, 305] For example, electrolyte optimization strategy such as "water-in-salt" systems have been reported to improve life span from 5.3 h to 170 h, though low ionic conductivity due to limited water content.[181] However, the expensive cost of the electrolyte are practical challenges remain to be overcome.[181, 306, 307] Meanwhile, several nanostructured materials (ZrO_2,[308] TiO_2,[184] $CaCO_3$,[185] PA,[309] *etc.*) have been investigated as protective coating layer, but low conductivity of these ceramic and polymeric materials inevitably increase the anode surface resistance.[305, 310] As a result, despite successful suppression of Zn dendrites formation, overall performance of the above-mentioned strategies are still far from satisfactory for practical applications, especially considering their low current density (<5 mA cm^{-2}) and large overpotential (> 0.1 V at 5 mA cm^{-2}).[295, 302] To summarize, an ideal coating layer is required to be: i) well adhered to Zn substrate, ii) highly ionic and electrical conductive to avoid extra impedance, iii) wettable in aqueous electrolyte environment and iv) flexible to accommodate volume change of Zn anode.[311]

To this end, MXenes with hexagonal closed packed structure would provide the ideal lattice match, negatively charged surface, superb conductivity and high hydrophilicity desired for the targeted ZIBs application.[312, 313] Previous studies using $Ti_3C_2T_x$[314] and sulfur-doped $Ti_3C_2T_x$[315] have shown preliminary successes, but limited porosity and randomly distributed termination still hinders overall performances. In this contribution, for the first time, porous Cl-terminated MXene (p-Ti_2CCl_2) is utilized as coating layer to realize stable Zn platting/stripping and prevent dendrite

growth for ZIBs application. Particularly, uniform Cl terminations on the p-Ti_2CCl_2 are utilized to minimize variance in near surface Zn^{2+} distribution, while its surface crystal arrangement induces preferential growth of the Zn (0002) crystal plane for dense and leveled deposition. Furthermore, the highly hydrophilic p-MXene ensures sufficient electrolyte coverage on the electrode surface and its high porosity enables sufficient ion transfer for rapid reactions. With these advantages, the p-Ti_2CCl_2 coated Zn anodes achieve low polarization and remarkably ultralong lifespan of 2000 h under both low and high current density of 1 and 10 mA cm^{-2} in symmetric cells. When assembled with MnO_2 cathode in a full cell, the ZIBs deliver distinctive capacity of 200 mAh g^{-1} at 5 C with excellent capacity retention of 91% after 2000 cycles. Remarkably, this work reveals the significance of porosity and terminations for MXene coating layers, paving way for promising large-scale zinc-based energy storage devices.

5.2 Experimental Section

Synthesis of Ti_2CCl_2 and porous Ti_2CCl_2 (p-Ti_2CCl_2). Porous Ti_2CCl_2 was produced using the eutectic etching method reported by our group.[265] Ti_2AlC was mixed with NaCl and $ZnCl_2$ in molar ratio of 1:9:6. Then the mixture was annealed at 550 ºC for 5 h, followed by HCl washing and freeze-drying. Non-porous MXene was etched in same condition without NaCl.

Fabrication of Ti_2CCl_2//Zn and p-Ti_2CCl_2//Zn. First, produced Ti_2CCl_2 or p-Ti_2CCl_2 powders were mixed with polyvinylidene difluoride (PVDF) at a weight ratio of 1:9 in NMP (N-methyl pyrrolidone) solvent followed by 12 h magnetic stirring at room temperature. Then, the resulting suspension was dispersed uniformly onto Zn foils by spray coating method and finally dried in vacuum at 80 °C overnight.

Material Charaterization. X-ray powder diffraction results were achieved by XRD, Rigaku Miniflex 600 with Cu Kα radiation as X-ray source. Scanning Electron Microscope (SEM) images of the samples were performed by Zeiss ULTRA. Transmission Electron Microscopy (TEM) pictures were recorded by JEOL, JEM-2010, 200 kV. The surface chemistry of p-Ti_2CCl_2//Zn was investigated by X-ray photoelectron spectra (XPS) by Thermal Scientific K-Alpha X-ray Photoelectron Spectrometer System with binding energies of C 1s calibrated by to 284.5 eV. Contact angles of 5 μL 2 M $ZnSO_4$ droplets on the bare and MXene coated Zn foils were tested by Dataphysics OCA20 contact angle meter.

Electrochemical Measurement. Typically, two bare Zn or MXene coated Zn foils were assembled in symmetric cells using glass microfiber filter membrane and 2 M $ZnSO_4$ as separator and electrolyte, respectively. The potentiostatic current-time transient curves of symmetric cells were achieved at a current density of 0.2 and 10 mA cm^{-2} with total capacity of 0.2 and 5 mAh cm^{-2} on a LAND battery-testing equipment to investigate the stripping/plating manner and cycling stability of bare and modified Zn foils. For Zn/MnO_2 full cells, commercial MnO_2 were firstly mixed together with CNT in weight ratio of 3:1 and then sonicated in ethanol. Afterwards, the ink was filtrated on glass fibre cloth with mass loading of MnO_2 estimated to be 1.2-1.5 mg cm^{-2}, and then dried at 80 °C overnight. The battery was fabricated with MnO_2 coated glass fibre, bare or p-Ti_2CCl_2//Zn foil and 2 M $ZnSO_4$/0.1 M $MnSO_4$ as cathode, anode and electrolyte. Galvanostatic charge/discharge (GCD) and cyclability tests were carried out on LAND battery system while cyclic voltammetry (CV) tests and electrochemical impedance spectroscopy (EIS) measurements were conducted on electrochemical station (BioLogic VMP-300).

Simulation of the Electric Field Contribution in COMSOL. Simplified two dimensional electric field distribution at the interface between electrolyte and anode was simulated based on a parallel plate capacitor model using COMSOL to demonstrate the inhibitory effect of p-Ti_2CCl_2 coating layer during Zn crystals growth. The length of two electrodes was set to be 250 μm with distance of 200 μm. The protuberance of bare Zn surface was represented by two semicircles with a diameter of 40 μm and a height of 50 μm. Moreover, there is a thin coating layer with a thickness of 10 μm for p-Ti_2CCl_2//Zn anode model. The size information of these simulations are based on the resultant SEM images. It should be noted that these models can only represent an ideal system other than real condition. The ionic conductivity of 2 M $ZnSO_4$ which filled in the gap between anodes was 5 S m^{-1}.[314] And the electrical conductivity of p-Ti_2CCl_2 and Zn metal were set to be 1.6×10^3 S m^{-1} (achieved from conductivity test) and 1.67×10^7 S m^{-1}, respectively.[177] The cathodic potential parameters are set based on the experimental voltage hysteresis (with or without p-Ti_2CCl_2 coating) and the anodic potential is zero constantly.

5.3 Results and Discussion

5.3.1 Structural Characterization of MXene

Few layers p-Ti_2CCl_2 was firstly synthesized by a eutectic etching ($ZnCl_2$/NaCl) method reported in our previous literature,[265] while non-porous Ti_2CCl_2 was prepared by etching with $ZnCl_2$.[21] As shown in their X-ray diffraction (XRD) patterns, both of the MXene samples exhibit characteristic peaks located at 10.22º corresponding to the (002) planes, verifying their layered structures with interlayer distance of 8.68 Å (**Figure 5-1a**). Meanwhile, scanning electron microscopy (SEM) images of the p-Ti_2CCl_2 and Ti_2CCl_2 reveal proper exfoliation when compared

to the Ti_2AlC MAX parent (**Figure 5-1b-d**). Transmission electron microscopy (TEM) measurement further confirms distribution of porosity with sizes above 5 nm across the p-Ti_2CCl_2 sheet (**Figure 5-2a**), which are not presence in the Ti_2CCl_2 (**Figure 5-2b**). Moreover, elemental analysis by X-ray photoelectron spectroscopy (XPS) reveal presence of Ti-Cl adsorption at 458.6 eV ($2p_{3/2}$)/464.8 eV ($2p_{1/2}$) in the high-resolution Ti *2p* spectra (**Figure 5-2c**), and at 199.0 eV ($2p_{3/2}$)/200.6 eV ($2p_{1/2}$) in the Cl *2p* spectra, validating predominate Cl termination on the p-MXene (**Figure 5-2d**). Upon confirming their successful synthesis, the as-prepared Ti_2CCl_2 samples were mixed in NMP with PVDF and spray coated onto bare Zn foils, the resulting electrodes are denoted as p-Ti_2CCl_2//Zn and Ti_2CCl_2//Zn, respectively (**Figure 5-2e**). Surfaces of both coated samples are observed by top-view SEM to be homogeneously covered by the MXene nanosheets, with no agglomeration or other undesired structures that might disrupt the zinc deposition (**Figure 5-3**). The flat surface and desirable porosity of the p-Ti_2CCl_2 coating layer are promising for future uniform and efficient Zn stripping/plating.

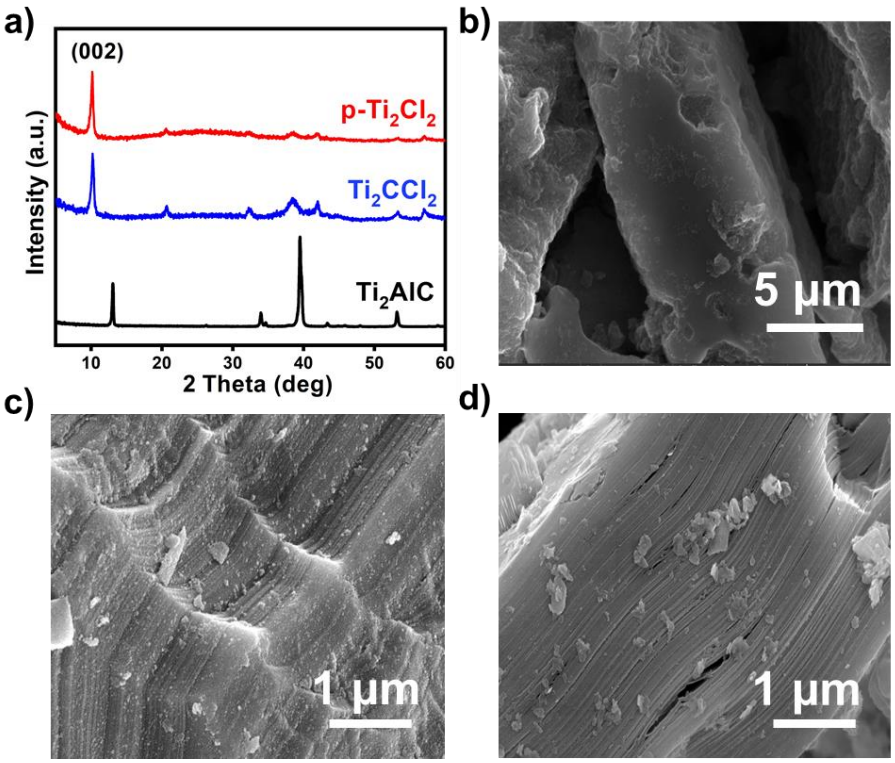


Figure 5-1. a) XRD patterns of Ti_2AlC, Ti_2CCl_2 and p-Ti_2CCl_2. SEM images of b) Ti_2AlC, c) Ti_2CCl_2 and d) p-Ti_2CCl_2.

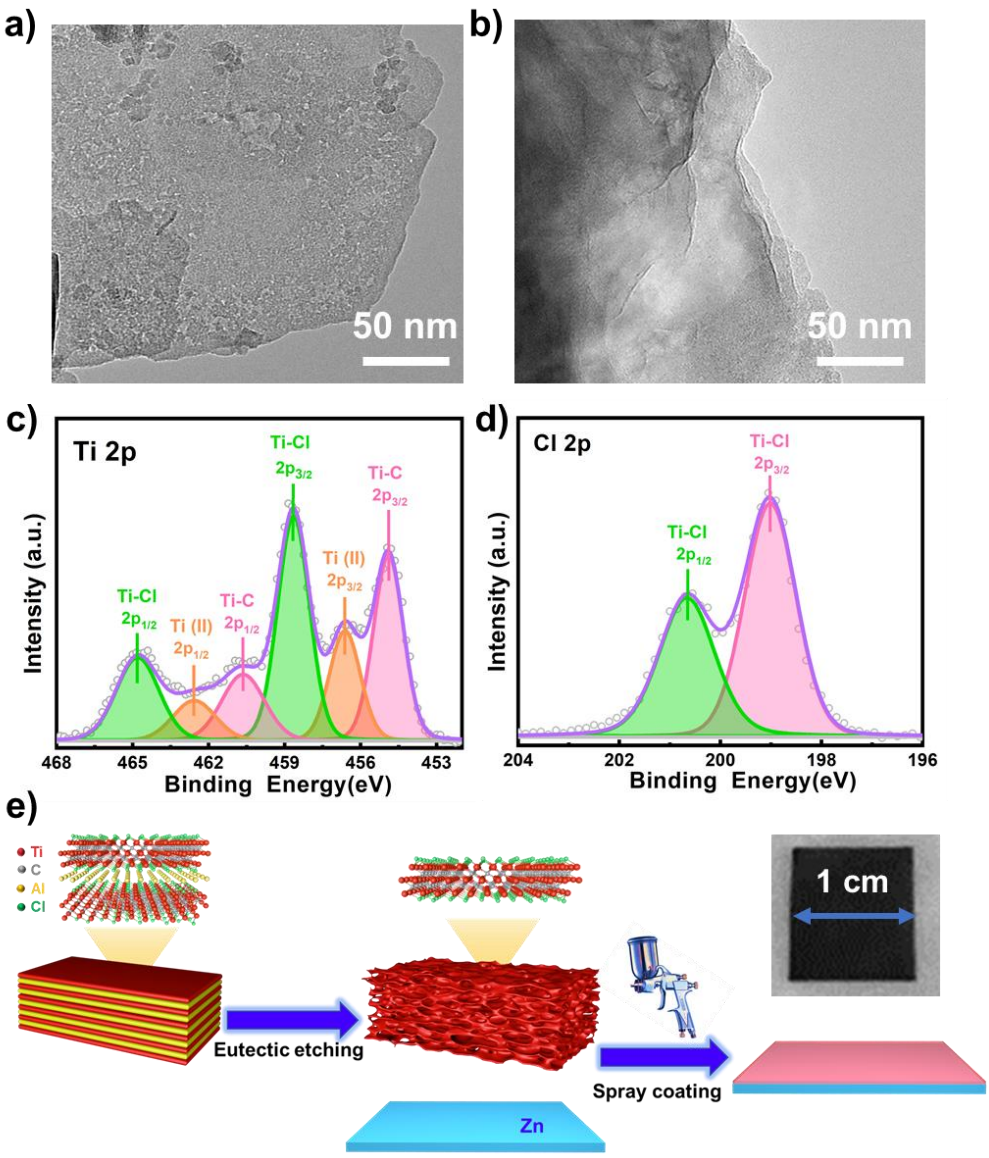


Figure 5-2. TEM images of a) Ti_2CCl_2 and b) p-Ti_2CCl_2. c)-d) Ti 2p, Cl 2p XPS spectra of p-Ti_2CCl_2. e) Schematic illustration of p-Ti_2CCl_2//Zn and Ti_2CCl_2//Zn electrodes fabrication.

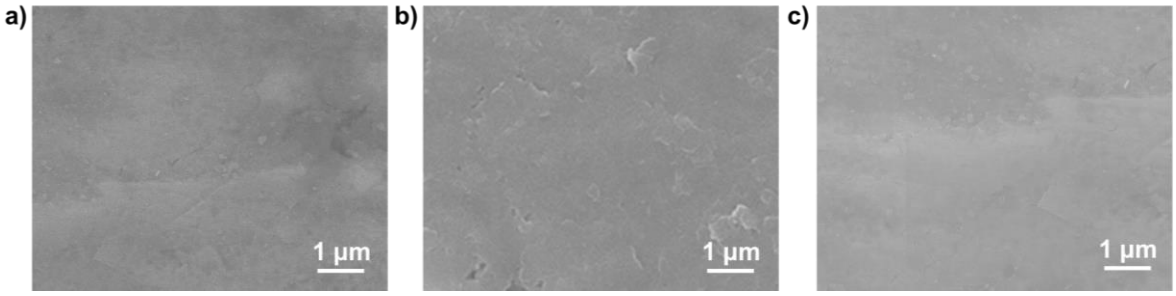


Figure 5-3. SEM images of a) bare Zn, b) Ti_2CCl_2//Zn and c) p-Ti_2CCl_2//Zn.

An obvious change to the electrode surface upon being coated by the Ti_2CCl_2 layer is their wettability toward the selected aqueous electrolyte, which was analyzed by contact angle measurements. As shown in **Figure 5-4a**, the bare zinc foil exhibits a contact angle of 134°, indicating a surface with high hydrophobicity, whereas the surface contact angle of Ti_2CCl_2//Zn is significantly reduced to 102° (**Figure 5-4b**). The change is attributed to specific behavior of the surface chloride functional group on MXene that are hydrophilic.[316] Interestingly, the contact angle of p-Ti_2CCl_2//Zn reaches an even lower value of 70°, which shifts the electrode surface to one that is moderately hydrophilic (**Figure 5-4c**). The differences between p-MXene//Zn and n-MXene//Zn reveal positive influences of the structural porosity toward electrolyte contact, likely through fluid absorption and increased adsorption sites. These are anticipated to improve electrolyte/electrode accessibility and ion flux uniformity, minimizing factors that are known to trigger dendrite formation.[187]

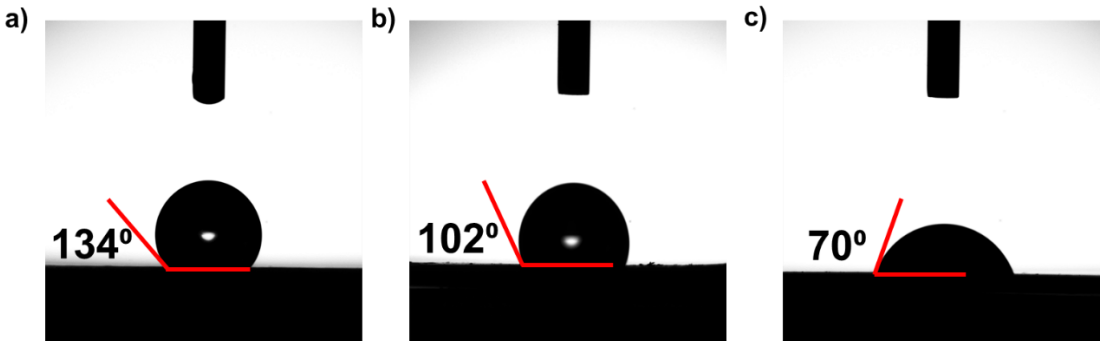


Figure 5-4. Contact angles of 2 M $ZnSO_4$ solution on a) bare Zn, b) Ti_2CCl_2//Zn and c) p-Ti_2CCl_2//Zn electrodes.

5.3.2 Anodes Electrochemical Performance

Building on the above discussed advantages of the MXene coated electrodes, each sample was evacuated in symmetric cells with 2 M $ZnSO_4$ electrolyte. The plating/stripping tests were first performed at 1 mA cm^{-2} with a limited capacity of 1 mAh cm^{-2} (**Figure 5-5a**,**b**). As shown, p-Ti_2CCl_2//Zn displays an ultra stable voltage profile with the lowest voltage hysteresis of 20 mV after 1000 h. While Ti_2CCl_2//Zn also endures 1000 h of cycling, but its overpotential reaches 35 mV. In stark contrast to the stable voltage platform observed on the Ti_2CCl_2 coated sample, the bare Zn foil experience large voltage fluctuation after 50 hours of cycling, and short circuited at 313 h with the cell voltage suddenly dropping below 5 mV. The cells were further evaluated at harsher conditions with a higher operating current density of 10 mA cm^{-2} with capacity limit of 5 mAh cm^{-2} to demonstrate their practical viability (**Figure 5-5c,d**). As expected, short circuiting of the bare Zn foils occurs at an earlier stage of 236 h and the cell voltage fluctuates with greater magnitude. Meanwhile, both of the MXene coated zinc electrodes achieve stable cycling for 1000 h or 2000 cycles, with the p-Ti_2CCl_2//Zn manifesting a lower polarization of 80 mV compared to

the 120 mV of Ti_2CCl_2//Zn, verifying the effectiveness of the MXene layers on promoting stable cycling in practical conditions. The improvement in cycling performance is attributed to the uniformly charged surface on the MXene protective layers, which promote homogeneous distribution of Zn^{2+} ions during the platting/stripping process.[305] Cyclic voltammetry (CV) analysis in half cell versus Zn foil reveal similar behaviors for all three samples, and it shows p-Ti_2CCl_2//Zn reaching far higher peak current densities in both the anodic and cathodic scans (**Figure 5-5e**).[317] The CV curves also shows significant cathodic onset potential decreased from the 117 mV of bare Zn foil to the 64 mV of Ti_2CCl_2 and 50 mV of p-Ti_2CCl_2 (**Figure 5-5f**). The reduced overpotentials represent the facilitated Zn plating with the help of MXenes. While the enlarged current represent the boosted nucleation active sites of porous MXene layers compared to non-porous MXene.[318]

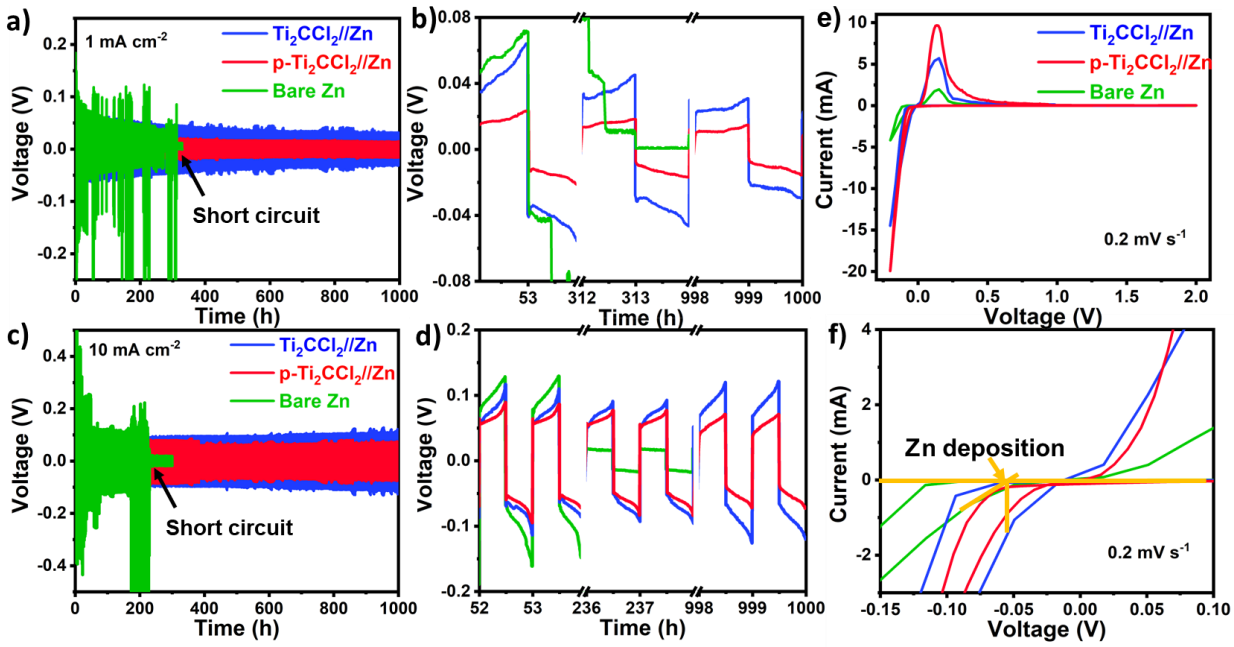


Figure 5-5. Galvanostatic cycling voltage profiles of bare Zn foil, Ti_2CCl_2//Zn and p-Ti_2CCl_2//Zn symmetric cells at a), b) the current density of 1 mA cm^{-2} with capacity limit of 1 mAh cm^{-2}, and c), d) the current density of 10 mA cm^{-2} with capacity limit of 5 mAh cm^{-2}. e), f) Cyclic voltammetry curves and enlarged profiles of bare Zn foil, Ti_2CCl_2//Zn and p-Ti_2CCl_2//Zn plating/stripping performance.

Electrochemical impedance spectroscopy (EIS) also reflects a similar trend, as the high-frequency regime semi-circles of the MXene coated samples are significantly smaller than the one of bare Zn foil, which are direct indication of faster charge transfer and reduced interface resistance (**Figure 5-6a**). Additionally, the trend remains after 100 cycles of zinc platting/stripping, ensuring that improvements induced by the MXene layers are not temporary. The kinetic improvements measured are attributed to the combined contributions of optimized surface chemistry and surface structure, which permit lower nucleation energy and more uniform Zn nucleation.[302, 314] In the

ensuing rate performance analysis, p-Ti_2CCl_2//Zn outperforms the Ti_2CCl_2//Zn and zinc foil as expected, with polarizations of 12, 20, 36, 60 and 80 mV at the current densities of 0.2, 1, 2, 5, and 10 mA cm^{-2}, respectively (**Figure 5-6b**). These results outperform many in previously reported literatures regarding Zn anodes protection (**Figure 5-6c**, **Table 5-2**). In addition, p-Ti_2CCl_2//Zn is the only one of the three samples that recover to its original state when the current density is turn back from 10 to 0.2 mA cm^{-2}, whereas the final polarization of Ti_2CCl_2//Zn is cut to 48.3 % of the original value. Bare Zn even encounters short circuit caused by undesired zinc dendrite when returned to initial current density. This comparison again demonstrates the high reversibility of p-Ti_2CCl_2//Zn toward zinc platting/stripping in different working condition. Its high cyclability is further supported by long term stability test, which shows p-Ti_2CCl_2//Zn achieving ultra-long cycling of 2000 h at both low and high current densities without obvious oscillation, proving its excellent potential for practical applications (**Figure 5-6d**).

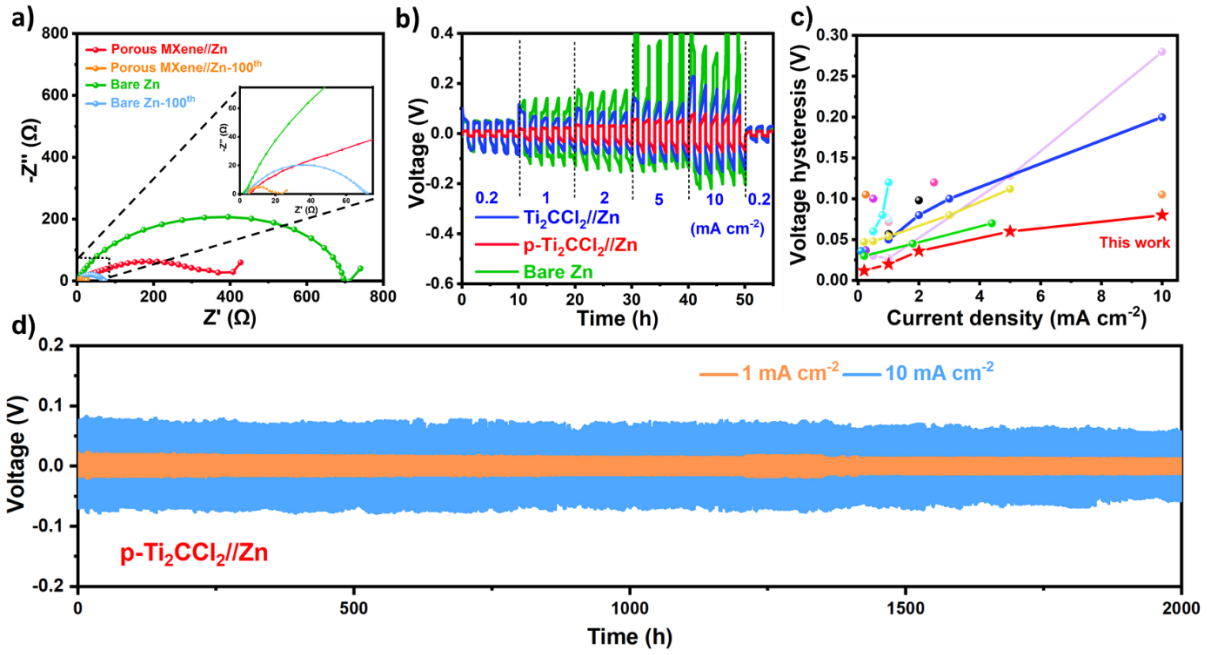


Figure 5-6. a) electrode impedance spectroscopies and b) rate performance of bare Zn foil, Ti_2CCl_2//Zn and p-Ti_2CCl_2//Zn. c) Voltage polarizations of p-Ti_2CCl_2//Zn versus other reported works. d) Long term cycling performance of p-Ti_2CCl_2//Zn at 1 mA cm^{-2} and 10 mA cm^{-2} for 2000 h.

Table 5-1. Comparison of this work and previously reported Zn anode protection results

Anode materials	Electrolyte	Voltage hysteresis (mV)	Current density (mA cm^{-2})	Area Capacity (mAh cm^{-2})	Cycle Life (h)	Ref.
$CaCO_3$@Zn	3M $ZnSO_4$+0.1M $MnSO_4$	105	0.25	0.05	836	185
CNT@Zn	2 M $Zn(CF_3SO_3)_2$	36	0.1	0.5	1800	319
Polyamide@Zn	$Zn(TfO)_2$	100	0.05	0.25	8000	309

ZrO_2@Zn	2 M $ZnSO_4$	37	0.25	0.125	3800	308
TiO_2@Zn	3 M $Zn(CF_3SO_3)_2$	57.2	1	1	150	184
MoS_2@Zn	1 M $ZnSO_4$+1 M $MnSO_4$	120	2.5	0.416	165	310
ZnS@Zn	1 M $ZnSO_4$	98	2	2	1100	295
ZnF_2@Zn	2 M $ZnSO_4$	71.5	1	1	800	320
PANZ@Zn	2 M $Zn(TfO)_2$	75	1	1	1145	321
HsGDY@Zn	2 M $ZnSO_4$	60	0.5	0.1	2400	322
		80	1	0.1	2400	
		120	2	0.1	2400	
Kaolin-Zn	2 M $ZnSO_4$	30	0.2	0.05	50	307
		45	1.8	0.45	50	
		70	4.4	1.1	800	
rGO@Zn	1 M $ZnSO_4$	50	1	2	200	323
		80	2	2	200	
		100	5	2	200	
		200	10	2	200	
MXene@Zn	2M $ZnSO_4$+0.2M $MnSO_4$	47	0.2	0.2	800	314
		48	0.5			
		54	1			
		80	3			
		112	5			
ZnSe@Zn	1M $ZnSO_4$	28	1	1	1500	305
		105	10	1	1500	
S/MXene@ZnS@Zn	2M $ZnSO_4$	30	0.5	0.5	1600	315
		26	1	0.5	1100	
		27	1	1	1100	
		128	5	5	400	
		279	10	1	180	
p-Ti_2CCl_2@Zn	2M $ZnSO_4$	12	0.2	0.2		**This work**
		20	1	1	2000	
		36	2	2		
		60	5	5		
		80	10	5	2000	

Post cycling characterizations of p-Ti_2CCl_2//Zn and the short circuited Zn foil were also collected after operation at 10 mA cm^{-2} to compare their morphological and cryptological changes. As shown in **Figure 5-7a**, cross-section SEM image of p-Ti_2CCl_2//Zn reveals a smooth and dense deposited layer of Zn with thickness of around 1 μm on top of the 10 μm thick p-Ti_2CCl_2 coating layer. Meanwhile, its top view SEM image shows that the deposited layer consists of hexagonal basal Zn crystals horizontally and homogeneously across the surface (**Figure 5-7b**). In comparison, randomly oriented nanoflakes with different sizes are found on the bare Zn foil surface in alignment with previous reporting, which is known to cause short circuit (**Figure 5-7c,d**).[302, 315, 320] Notable differences in crystal plane are also identified in the post cycling XRD spectra of the two samples. Specifically, rapid growth of the (0002) peak is observed in p-Ti_2CCl_2//Zn, with its $I_{(0002)}/I_{(10\bar{1}1)}$ ratio raised rapidly from 0.19 to 0.42 in 1000 cycles, while its $I_{(10\bar{1}0)}/I_{(10\bar{1}1)}$ remain around 0.23 and 0.27 during the same period (**Figure 5-8a** and **Table 5-2**). This indicate a preference for (0002) peak growth, which is likely due to Ti_2CCl_2 and the zinc (0002) plane sharing a hexagonal crystal arrangement of similar dimension. As for the bare Zn electrode, its $I_{(0002)}/I_{(10\bar{1}1)}$ ratio only reached 0.15 when it short-circuited, where as the $I_{(10\bar{1}0)}/I_{(10\bar{1}1)}$ grew more than four times from 0.47 to 1.16 (**Figure 5-8b**). Crystal arrangements of the three planes are demonstrated by the visual illustration displayed in **Figure 5-8c**. Of which, the (0002) plane is known to prefer grow along the basial axis in parallel to the substrate, whereas the $(10\bar{1}0)$ and $(10\bar{1}1)$ planes are often affiliated with dendrite formation.[324] Their variations directly lead to the different deposition phenomenon presented in **Figure 5-8d**. As deposition on the bare Zn surface occurs predominately in the form of $(10\bar{1}1)$ or $(10\bar{1}0)$ flakes, each step of the platting/stripping

process adds onto the surface inhomogeneity, which eventually ends in short circuiting by dendrite contact. The p-Ti_2CCl_2//Zn on the other hand promotes growth of the (0002) planes, leading to formation of smooth and dense deposit layer that are highly suitable for long term stable cycling.

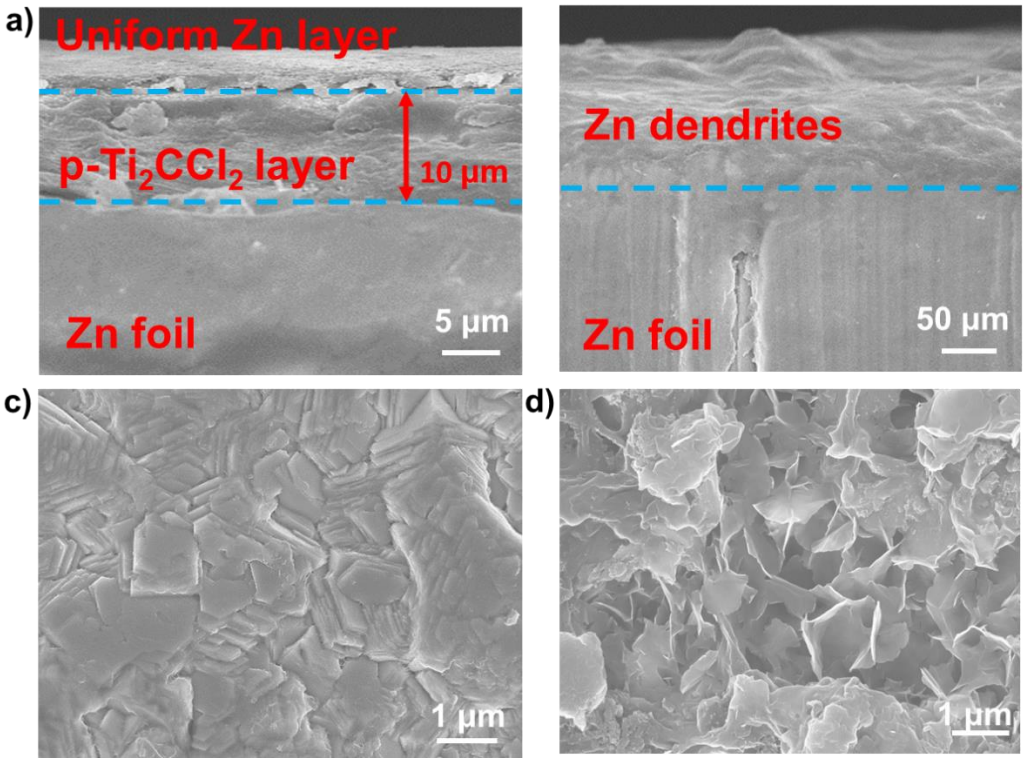


Figure 5-7. Cross-sectional and top-view SEM images of a), c) p-Ti_2CCl_2//Zn electrode and b), d) bare Zn electrode after cycling.

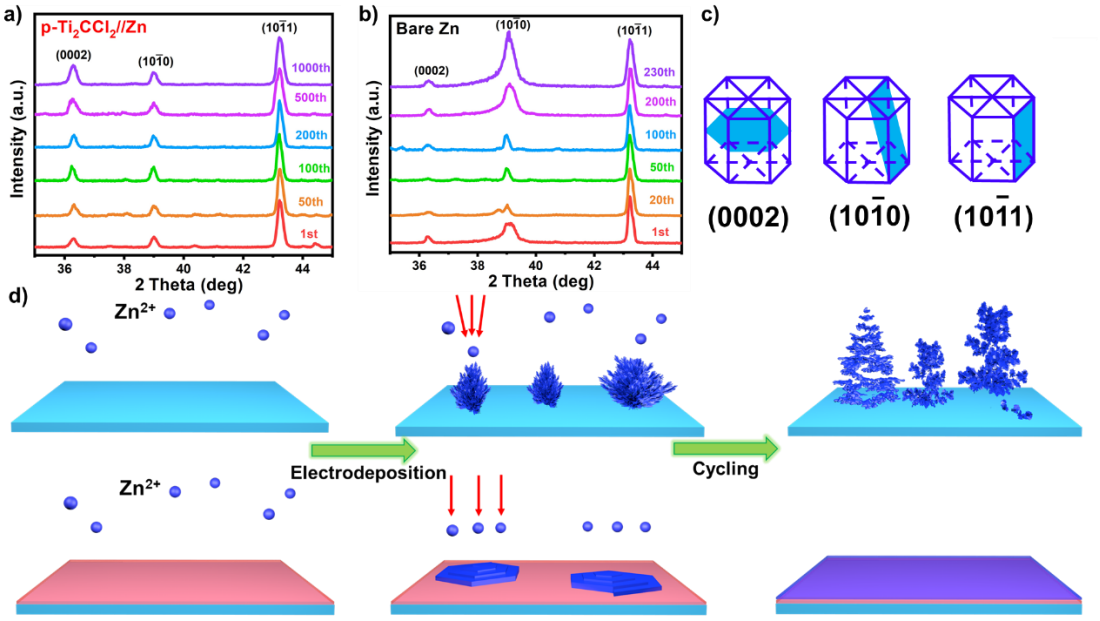


Figure 5-8. XRD spectra of a) p-Ti_2CCl_2//Zn and b) bare Zn after different cycles at 10 mA cm^{-2}. c) Scheme of crystallographic planes of (0002), (**10$\bar{1}$0**) and (**10$\bar{1}$1**). d) Schematic illustration of Zn deposition and cycling on p-Ti_2CCl_2//Zn (top) and bare Zn (bottom).

Table 5-2. XRD comparasion of p-Ti_2CCl_2//Zn and bare Zn after different cycles and electrodeposition times

	p-Ti_2CCl_2//Zn			Bare Zn		
		$I_{0002}/I_{10\bar{1}1}$	$I_{10\bar{1}0}/I_{10\bar{1}1}$		$I_{0002}/I_{10\bar{1}1}$	$I_{10\bar{1}0}/I_{10\bar{1}1}$
Cycle number	1^{st}	0.19	0.23	1^{st}	0.15	0.47
	50^{th}	0.26	0.23	20^{th}	0.09	0.24
	100^{th}	0.33	0.32	50^{th}	0.08	0.27
	200^{th}	0.29	0.27	100^{th}	0.15	0.36
	500^{th}	0.37	0.29	200^{th}	0.16	0.69
	1000^{th}	0.42	0.27	230^{th}	0.15	1.16
Electrodeposition time	Initial	0.06	0.28	Initial	0.06	0.28
	20 min	0.12	0.18	20 min	0.09	0.41
	40 min	0.21	0.31	40 min	0.08	0.49
	1 hour	0.25	0.26	1 hour	0.05	0.69

More direct observations of the morphological evolutions were further collected on samples subjected to 20, 40 and 60 mins of Zn electrodeposition at 10 mA cm^{-2}. As shown in **Figure 5-9a-c**, the deposits on p-Ti_2CCl_2//Zn adapt the hexagonal morphology early on and expand horizontally in size with increasing deposition time, while its vertical growth occurs layer by layer with limited void spaces. Such type of basal growth are ideal for the targeted ZIB application given the minimal surface-to-bulk ratio of the deposit,[324] which minimize surface roughness and increase electrode energy density. In striking contrast, zinc clusters with randomly oriented planes are observed after 20 mins of deposition on the bare Zn surface (**Figure 5-9d**). They further aggregate as deposition time increases, resulting in large protrusions of irregularly shaped zinc dendrite by the end of the 60 mins deposition (**Figure 5-9e,f**). The different deposition behaviors are also captured in larger scale by optical microscopy (**Figure 5-9g**). The presence of sharp dendrite on the Zn foil is apparent after 20 mins of platting, while surface roughness and cluster formation are also worsened as the deposition continues. By contrast, the deposition on p-Ti_2CCl_2//Zn remained compact and smooth throughout the entire deposition process, without any discernible dendrite formation over 1 hour of deposition (**Figure 5-9h**).

Ex-situ XRD spectra of the electrodeposition samples also points to a similar conclusion as the post cycling analysis, which shows bare Zn favoring the $(10\bar{1}0)$ growth with its $I_{(10\bar{1}0)}/I_{(10\bar{1}1)}$ ratio growing significantly from 0.28 to 0.69 in 1 h of deposition, while its $I_{(0002)}/I_{(10\bar{1}1)}$ ratio reduces from 0.06 to 0.05 (**Figure 5-9i & Table 5-2**). As for the p-Ti_2CCl_2//Zn, its $I_{(0002)}/I_{(10\bar{1}1)}$ ratio gradually increases from 0.06 to 0.12 in 20 mins and then to 0.25 in 1 h, with minimal growth of the $I_{(10\bar{1}0)}/I_{(10\bar{1}1)}$ ratio (**Figure 5-9j & Table 5-2**). This experiment again verifies deposition

of the Zn (0002) plane is favored on the p-Ti_2CCl_2//Zn surface, ensuring that accumulation of the (0002) plane occur during the deposition process, instead of it being a residue from the platting/stripping process. Lastly, theoretical simulation of the electric field distributions at the electrode/electrolyte interface are modeled using COMSOL Multiphysics to reveal the impact of dendrite length to uniformity of near surface electric field. As depicted in **Figure 5-9k**, uneven micro-protrusions found on the bare Zn foil would cause inhomogeneity of surrounding field, leading to high electric field intensity of 2820 V m^{-1} at the tip of the structure that exacerbate dendrite growth.[320] Meanwhile, the flat deposits on p-Ti_2CCl_2//Zn effectively passivated the electric field perturbance, promoting even charge redistribution that minimize variances with maximum electric field intensity reduced to 530 V m^{-1} (**Figure 5-9l**).

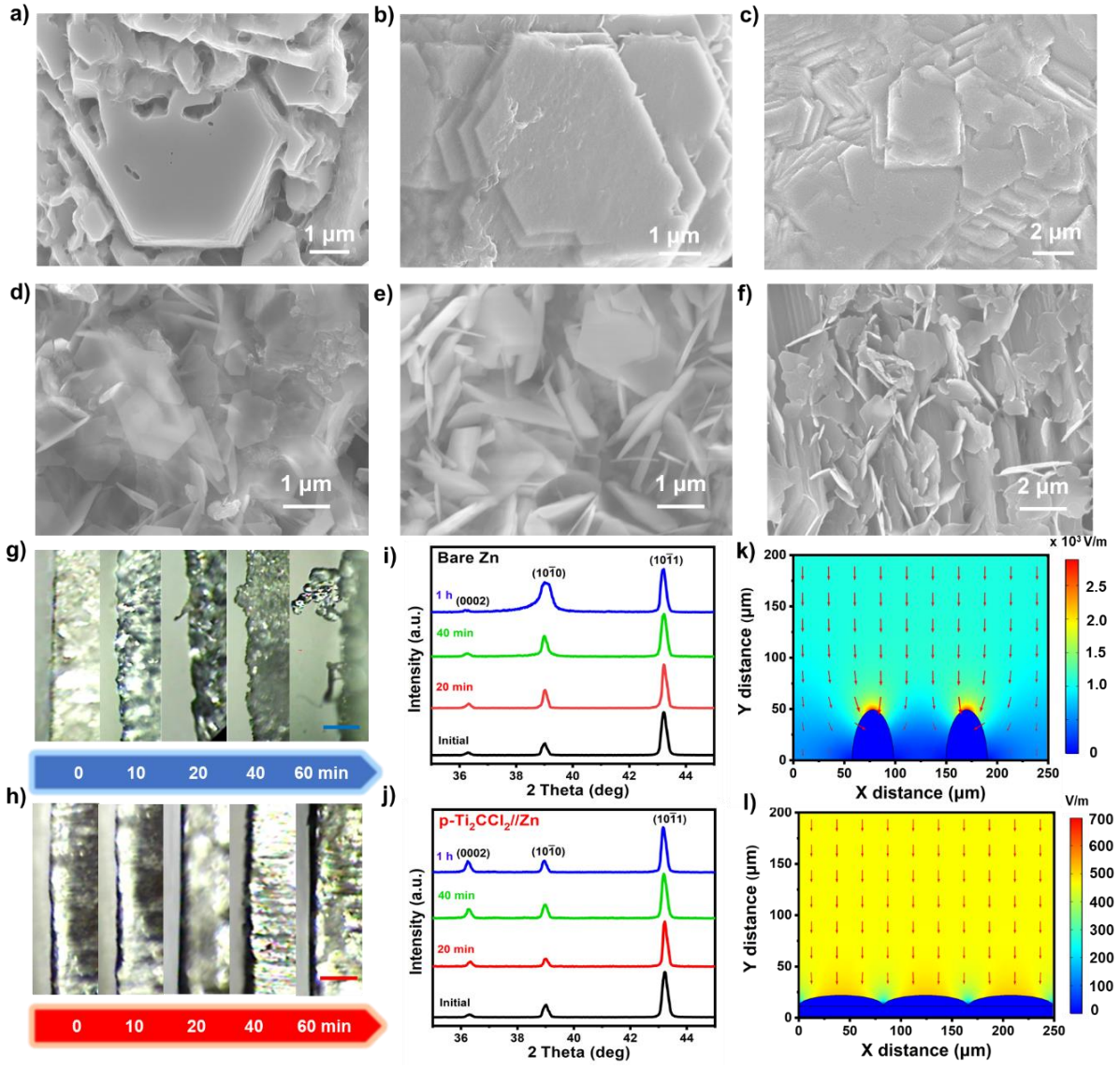


Figure 5-9. SEM images of a)-c) p-Ti_2CCl_2//Zn and d)-f) bare Zn electrodes after 20, 40, 60 min Zn deposition. *In-situ* optical microscopy visualization of g) bare Zn and h) p-Ti_2CCl_2//Zn, with scale bar representing 50 μm. *Ex-situ* XRD spectra of i) bare Zn and j) p-Ti_2CCl_2//Zn. Electric field simulation of k) bare Zn and l) p-Ti_2CCl_2//Zn.

To address the influence of MXene terminations during the dendrite prevention process, Ti_2CT_X with random terminations is prepared using LiF and HCl as reported.[325] XRD patterns showing (002) peak at 10.1º and SEM image with layered structure reveal the successful synthesis (**Figure 5-10a,b**). Although Ti_2CT_X//Zn also shows more stable cycling performance than bare Zn foil, it encounters short circuit after 931 h at 1 mA cm^{-2} and 920 h at 10 mA cm^{-2} with significantly higher voltage hysteresis than those of Ti_2CCl_2//Zn and p-Ti_2CCl_2//Zn (**Figure 5-10c**). To probe the reason of inferior performance of Ti_2CT_X compared to Ti_2CCl_2, SEM and XRD characterizations are also performed during zinc deposition process. As shown in **Figure 5-10d**, even though Ti_2CT_X//Zn can also passivate the dendrite growth after 20 mins by forming parallel plates, subsequent vertical flakes start to grow after 40 mins (**Figure 5-10e**). Finally, dendrites growing vertically still exist after 1 h (**Figure 5-10f**). The morphology formation well matches *ex-situ* XRD results in **Figure 5-11** and **Table 5-3**, the $I_{(0002)}/I_{(10\bar{1}1)}$ ratio indeed increases to 0.15 in 40 mins, but then sharply decreases to 0.05 in 1 h, with growth of the $I_{(10\bar{1}0)}/I_{(10\bar{1}1)}$ ratio sharply boosting from 0.24 at 20 mins to 0.68 at 40 mins. After 1 h, the $I_{(0002)}/I_{(10\bar{1}1)}$ and $I_{(10\bar{1}0)}/I_{(10\bar{1}1)}$ ratio drop to 0.05 and 0.11. This phenomenon can be explained by the random distributed terminations of Ti_2CT_X. These diverse terminations with different affinity result in uneven electric field distribution, promoting zinc crystals growing along $(10\bar{1}0)$ after 40 mins and $(10\bar{1}1)$ after 1 h during Zn plating process, which eventually form dendrites.

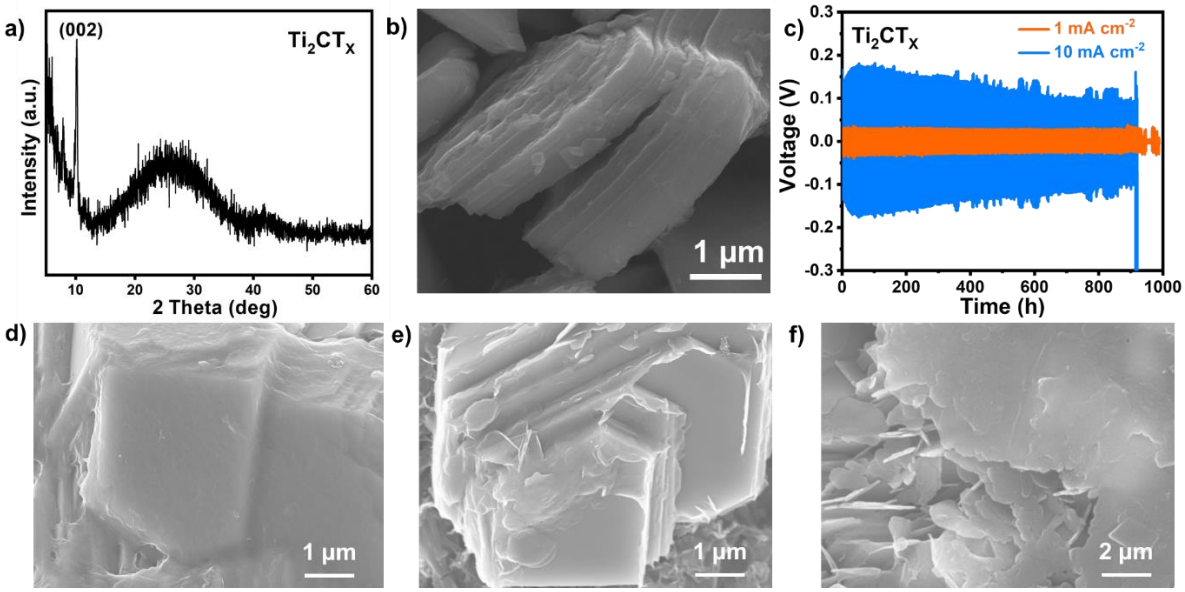


Figure 5-10. a) XRD and b) SEM results of Ti_2CT_X. c) Cycling results of Ti_2CT_X//Zn symmetric cells at 1 mA cm^{-2} and 10 mA cm^{-2}. SEM images of Ti_2CT_X//Zn after electrodeposition time of d) 20 min, e) 40 min and f) 1 h.

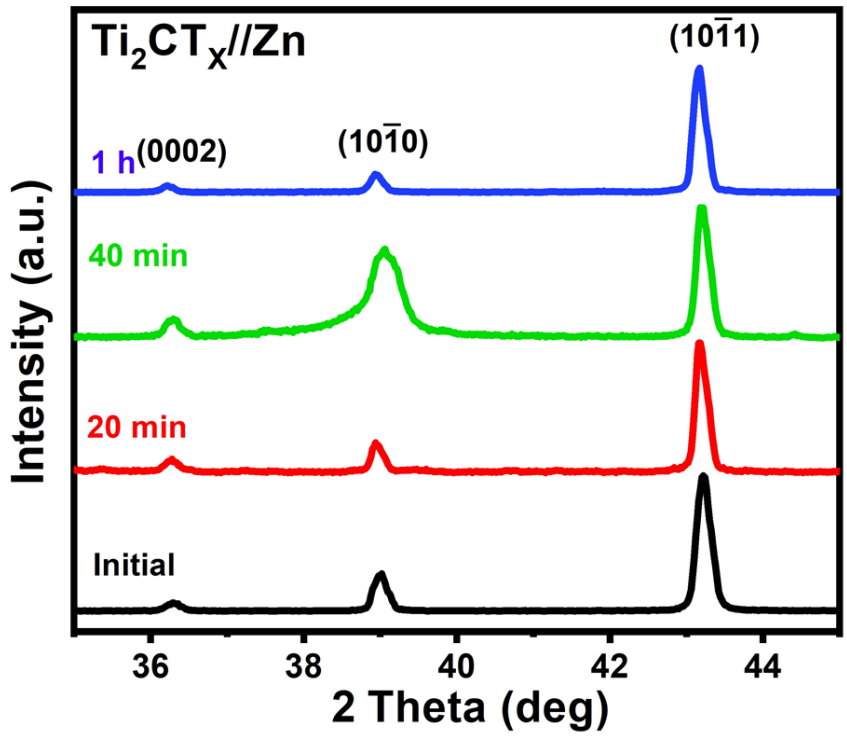


Figure 5-11. *Ex-situ* XRD results of Ti_2CT_X//Zn after electrodeposition time of 20 min, 40 min and 1 h.

Table 5-3. XRD information of Ti_2CT_X//Zn

	Ti_2CT_X//Zn		
		$I_{0002}/I_{10\bar{1}1}$	$I_{10\bar{1}0}/I_{10\bar{1}1}$
Electrodeposition time	Initial	0.06	0.28
	20 min	0.11	0.24
	40 min	0.15	0.68
	1 hour	0.05	0.11

5.3.3 Full Cell Electrochemical Performance

Building on the above observations, practical application viability of the anodes were further evaluated in full cells by pairing with commercially available MnO_2 that have been widely investigated as aqueous ZIBs cathode owing to their low cost and high theoretical capacity.[326] Although the full cell cycling stability heavily depends on the cathode material, the test still permits probing of impacts by the modified anode. CV graphs of all three ZIBs exhibit redox peaks that align with previous reporting,[327] with two anodic peaks near 1.58 V and 1.64 V, and two cathodic peaks positioned near 1.23 V and 1.39 V, confirming that the baseline redox reactions remain the same (**Figure 5-12a**). The lower voltage polarization of 30 mV and higher current suggest smaller polarization and improved Zn^{2+} kinetic benefited by p-Ti_2CCl_2.[295, 308] Their galvanostatic charge-discharge (GCD) curves at current density of 0.1 C also share similar platforms, with the p-Ti_2CCl_2//Zn ZIB delivering a remarkable capacity of 302.1 mAh g^{-1} that is higher than the 292.3 mAh g^{-1} of bare Zn ZIBs (**Figure 5-12b**). **Figure 5-12c** compares the rate capability of the two ZIBs, which shows the p-Ti_2CCl_2//Zn outperforming the bare Zn ZIBs anode on discharge capacities and voltages in all testing conditions. The lower charge transfer resistance further confirms the higher ion conductivity of p-Ti_2CCl_2//Zn anode compared to bare Zn anode (**Figure 5-12d**).[310] The p-Ti_2CCl_2//Zn ZIB also possesses ultralong cycling stability, maintaining 91% of its 200 $mAhg^{-1}$ discharge capacity for over 2000 cycles operation at 5 C (**Figure 5-12e**). Its surface after the full cell cycling remains free of dendrite and is occupied predominately by hexagonal shape zinc deposit **(Figure 5-13)**. This cycling performance is top tier among the reported literature, confirming the high viability of p-Ti_2CCl_2//Zn as anode for practical ZIBs.

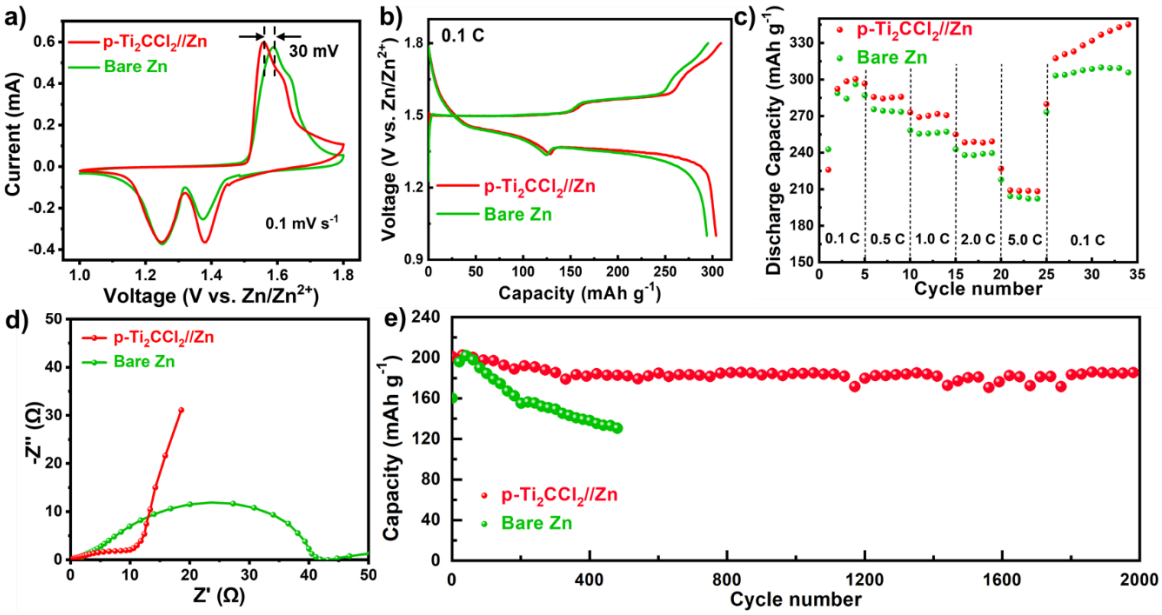


Figure 5-12. a) GCD, b) rate capability, c) CV, d) EIS and e) cycling curves of full cells with bare Zn and p-Ti_2CCl_2//Zn as anodes and MnO_2 as cathode.

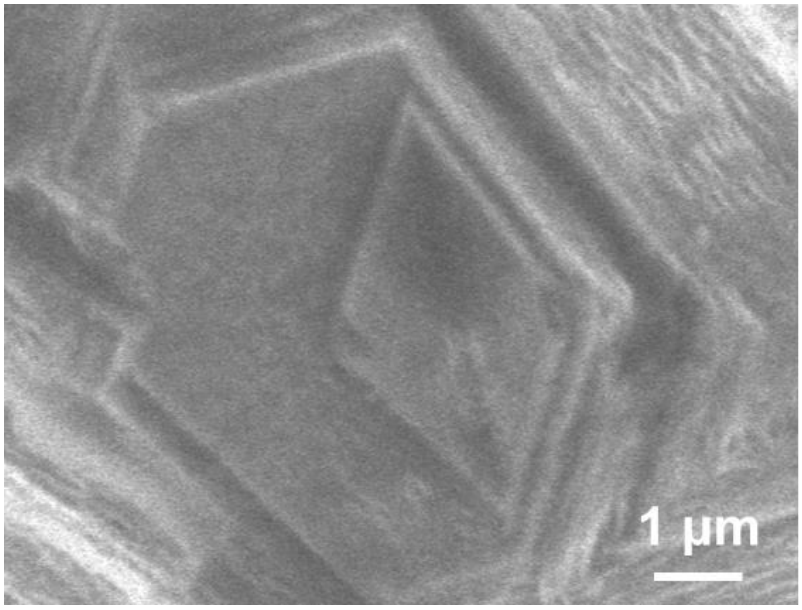


Figure 5-13. SEM image of p-Ti_2CCl_2//Zn after full cell test.

5.4 Conclusion

In summary, this study developed a widely applicable strategy to resolve the long-standing issue of zinc dendrite in ZIBs using Cl-terminated porous MXene. The p-Ti_2CCl_2 provides a hexagonal crystal structured platform that promote preferential growth of Zn (0002) crystal planes through close structure alignment. Meanwhile, its uniform Cl terminations lowers the zinc nucleation energy and suppress dendrite appearance through minimizing the protuberances in the surface electric field. The high ionic conductivity and hydrophilicity of p-Ti_2CCl_2 are also critical for the optimal electrochemical performance as they provide sufficient electrolyte and ion flux during repeated zinc platting/stripping. As a result, the p-Ti_2CCl_2//Zn anode achieves reduced overpotential of 80 mV at the high current density of 10 mA cm^{-2} for over 2000 h in symmetric cell. This high cyclability further extends to full cell assembled with MnO_2 cathode, which achieves stable cycling of 2000 cycles at current density of 5 C with a capacity retention of 91%. Overall, our findings on the Cl-terminated porous MXene solidifies the case for implementation of the safe and environmentally friendly aqueous Zn-ion systems, paving a path for the continued development of dendrite-free metal anode for next-generation battery systems.

Chapter 6 Summary and Future Perspectives

6.1 Summary

In this thesis, porous MXene is produced by an advanced green chemistry method and its applications for dual ion battery (Chapter 3) and zinc ion battery (Chapter 4 and 5) are explored. Using different characterization techniques, the mechanism to induce porosity during the synthesis of MXene is identified. The function of its porosity and Cl terminations during CoHCF crystal growth and zinc electrodeposition rearrangement are also unveiled. Further insights of MXene and MXene based composites for electrochemical applications are underlined in energy storage devices.

In Chapter 3, a nonhazardous annealing synthesis is introduced to produce Cl-terminated MXene ($Ti_3C_2Cl_2$) with controllable in-plane porosity prepared directly from MAX precursor (Ti_3AlC_2) using salt mixture of NaCl and $ZnCl_2$. Phase diagram analysis of the mixture dependencies on composition and temperature reveals a pore-preserving mechanism enabled by unique eutectic mixture, which leads to substantial increase in mesoporosity and four-folds growth in surface area. DFT modeling demonstrates the lower Li diffusion barrier of $Ti_3C_2Cl_2$ compared to $Ti_3C_2T_x$. While X-ray spectroscopies analyses reveal increase of TiC_6 octahedral symmetry in the MXene layers as a result of the predominant Cl-terminations. Benefiting from these optimizations, the resulting porous $Ti_3C_2Cl_2$ achieves a high capacity of 382 mAh g^{-1} at current density of 0.1 A g^{-1} as anode for dual ion battery, with excellent capacity retention of 89% after 1000 cycles at 2.0 A g^{-1}. A $Ti_3C_2Cl_2$/graphite dual-ion battery full cell was fabricated to demonstrate the material application potential, which delivers 242 mAh g^{-1} at 0.1 A g^{-1} with 83%

retention over 1000 cycles at 1.0 A g^{-1}. To summarize, a new path based on green chemistry is demonstrated to optimize MXene porosity and structural crystallinity for electrochemical applications.

In Chapter 4, in-plane porous MXene is further employed as conductive template to grow cobalt hexacyanoferrate. It is identified that the negative charges of porous MXene successfully induce the crystal growth of CoHCF from nanospheres to nanotubes. Aided from the unique morphology, the surface area of the composite is increased to 237.9 m^2 g^{-1}, providing more Zn^{2+} ion intercalation sites. Meanwhile, the crystalline of CoHCF is found to be increased with the addition of porous MXene. The formed metastable Co^{2+}-MXene influences the competitive relationship between CN^- and H_2O, reducing the structural vacancies in the CoHCF. By alleviating the drawbacks of PBAs as ZIBs cathode material including low surface area, low conductivity and high defectiveness, the nanotube shaped CoHCF/MXene composite delivers high capacity of 197 mAh g^{-1} at 0.1 A g^{-1} with significant voltage plateau over 1.8 V and only 5.6% capacity decay after 3000 cycling at 2.0 A g^{-1}. This work underlines the multifunction of porous MXene during inducing the crystal growth of CoHCF: controllably modifying the morphology, increasing crystalline and enhancing overall conductivity of the composite, thus greatly improves the electrochemical performance of CoHCF. These adjustments are given rise to the negative charged nature, metallic conductivity, and high porosity of the synthesized MXene.

In Chapter 5, porous MXene is applied as coating layer for Zn anode to suppress the dendrite growth. The uniformly distributed Cl terminations of the as-prepared MXene helps to rearrange the electrodeposition of Zn^{2+} ions towards horizontal plates with significantly increased (0002) crystal planes compared to bare Zn foils. It is unveiled that random terminations on Ti_2CT_x are

detrimental for uniformizing Zn deposition compared to Ti_2CCl_2. Based on the advantage of MXene, porous Ti_2CCl_2 helps to lower the voltage hysteresis. Due to the high porosity and hydrophilicity characteristics of porous Ti_2CCl_2, the lifespan of symmetric cell is extended up to 2000 h even at 10 mA cm^{-2}, with low voltage polarization of 80 mV. The zinc ion battery fabricated with MnO_2 as cathode and porous MXene//Zn as anode exhibits excellent capacity retention of 91% after 2000 cycles. This work uncovers the importance of sole terminations on MXene during suppressing dendrite growth and unveils the benefit of porosity on MXene as efficient coating layer, paving the way for porous MXene as redistributor for other metal anodes.

6.2 Future Outlook

Based on the above results in the thesis, suggestions for future research and development regarding porous MXenes and their applications for energy storage devices are provided.

1. ***Further exploration on eutectic mixture synthesis towards porous MXene with different halogen terminations.*** Although eutectic mixture etching strategy has been proven to be effective in synthesizing porous MXene in Chapter 3, only Cl termination was studied. As MXenes with other halogen terminations (-Br, -I) have also been invented,[21] eutectic etching method may also be employed to create in-plane pores on MXene with varieties of terminations. The different halogen termination and surface chemistry of porous MXene and their influence on electrochemical performance are important information for further optimization of the materials. Moreover, intercalation kinetics and discharge capacity of the porous MXene can be further improved through tunning its interlayer spacing, this can be done through modification of parameters such as organic solvents, additives in its delamination process. However, attention

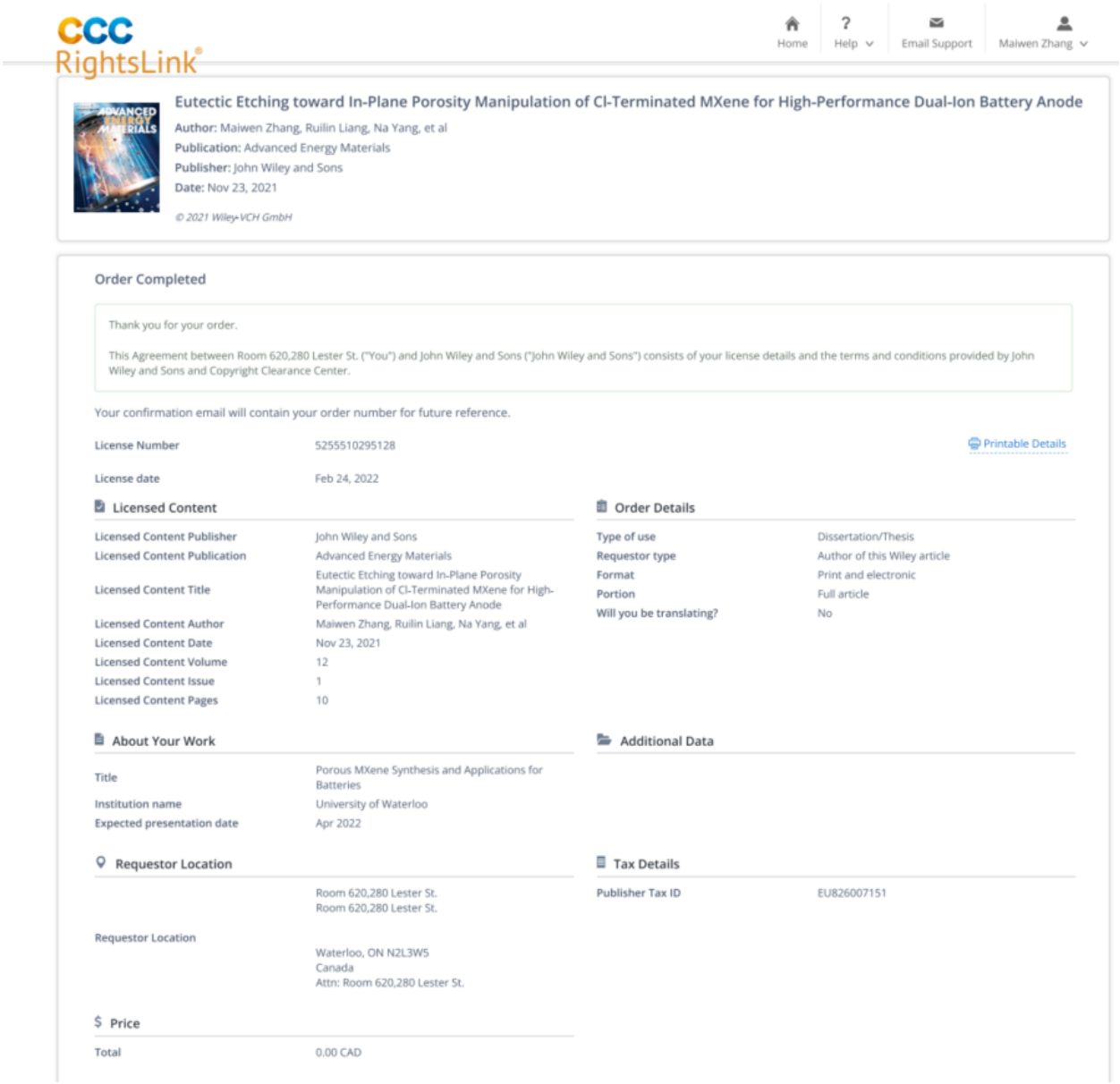
should be paid that terminations may be replaced by -OH or -O during the delamination process. Characterization such as EDS and XPS can be used to examine the termination difference before and after delamination. Beside fundamental investigations, scaling up the eutectic etching method with optimization of temperature, heating rate and precursor ratio can also provide better feasibility for this green chemistry synthesis method.

2. ***Developing composites based on porous MXene.*** In Chapter 4, the as-prepared porous MXene is proven to effectively enhance the energy storage capability of CoHCF as ZIB cathode. The inducing effect of porous MXene is attractive for tuning the crystalline structure and morphology of the composite materials as the negative charged MXene can absorb the cationic precursor for control of the crystal growth route of nanomaterials. The work in this thesis only discussed the effect of Co^{2+} cation concentration during the synthesis. Exploring different types of cations such as Ni^{2+} and Cu^{2+} are encouraged to study their susceptibility to the inducing effect from MXene. The effect of different terminations (-Br, -I) on MXenes during composite growth is also worth to be investigated. Further research regarding composition with organic materials or metal-organic frameworks, which are also promising ZIBs cathode candidates, are recommended to pursue high performance energy storage devices.

3. ***Defects and doping engineering on porous MXene.*** Defects (vacancies) design and atom doping are effective strategies to modify the stability and properties of MXenes. In conventional HF etching, the highly concentrated HF can cause more defects on produced MXene,[8] but the determining factor of defects on MXenes nanosheet produced by eutectic etching method is yet to be unveiled. As the active sites of MXene can be greatly improved by defects and atom (N, S, P) doping engineering,[7] these modifications are likely to enhance the electrode activity.

Additionally, when used as redistribution layer for metal anode, porous MXene with modified electronic structure can attract more zinc ions in the electrolyte, resulting in denser and more planar deposition layer.

Letters of Copyright Permission



CCC RightsLink®

Home | Help | Email Support | Maiwen Zhang

Eutectic Etching toward In-Plane Porosity Manipulation of Cl-Terminated MXene for High-Performance Dual-Ion Battery Anode

Author: Maiwen Zhang, Ruilin Liang, Na Yang, et al
Publication: Advanced Energy Materials
Publisher: John Wiley and Sons
Date: Nov 23, 2021

© 2021 Wiley-VCH GmbH

Order Completed

Thank you for your order.

This Agreement between Room 620,280 Lester St. ("You") and John Wiley and Sons ("John Wiley and Sons") consists of your license details and the terms and conditions provided by John Wiley and Sons and Copyright Clearance Center.

Your confirmation email will contain your order number for future reference.

Printable Details

License Number	5255510295128
License date	Feb 24, 2022

Licensed Content

Licensed Content Publisher	John Wiley and Sons
Licensed Content Publication	Advanced Energy Materials
Licensed Content Title	Eutectic Etching toward In-Plane Porosity Manipulation of Cl-Terminated MXene for High-Performance Dual-Ion Battery Anode
Licensed Content Author	Maiwen Zhang, Ruilin Liang, Na Yang, et al
Licensed Content Date	Nov 23, 2021
Licensed Content Volume	12
Licensed Content Issue	1
Licensed Content Pages	10

Order Details

Type of use	Dissertation/Thesis
Requestor type	Author of this Wiley article
Format	Print and electronic
Portion	Full article
Will you be translating?	No

About Your Work

Title	Porous MXene Synthesis and Applications for Batteries
Institution name	University of Waterloo
Expected presentation date	Apr 2022

Additional Data

Requestor Location

	Room 620,280 Lester St. Room 620,280 Lester St.
Requestor Location	Waterloo, ON N2L3W5 Canada Attn: Room 620,280 Lester St.

Tax Details

Publisher Tax ID	EU826007151

Price

Total	0.00 CAD

References

[1] M. Naguib, M. Kurtoglu, V. Presser, J. Lu, J. Niu, M. Heon, L. Hultman, Y. Gogotsi, M. W. Barsoum, *Adv. Mater.* **2011**, *23*, 4248.

[2] B. Anasori, M. R. Lukatskaya, Y. Gogotsi, *Nature Reviews Materials* **2017**, *2*, 1.

[3] M. Naguib, M. W. Barsoum, Y. Gogotsi, *Adv. Mater.* **2021**, *33*, 2103393.

[4] M. Naguib, V. N. Mochalin, M. W. Barsoum, Y. Gogotsi, *Adv. Mater.* **2014**, *26*, 992.

[5] A. Lipatov, H. Lu, M. Alhabeb, B. Anasori, A. Gruverman, Y. Gogotsi, A. Sinitskii, *Sci. Adv.* **2018**, *4*, eaat0491.

[6] Y. Zhang, L. Wang, N. Zhang, Z. Zhou, *RSC Adv.* **2018**, *8*, 19895.

[7] L. Gao, C. Li, W. Huang, S. Mei, H. Lin, Q. Ou, Y. Zhang, J. Guo, F. Zhang, S. Xu, *Chem. Mater.* **2020**, *32*, 1703.

[8] C. Zhang, Y. Ma, X. Zhang, S. Abdolhosseinzadeh, H. Sheng, W. Lan, A. Pakdel, J. Heier, F. Nüesch, *Energy & Environmental Materials* **2020**, *3*, 29.

[9] F. Ming, H. Liang, G. Huang, Z. Bayhan, H. N. Alshareef, *Adv. Mater.* **2021**, *33*, 2004039.

[10] C. Xu, L. Wang, Z. Liu, L. Chen, J. Guo, N. Kang, X.-L. Ma, H.-M. Cheng, W. Ren, *Nature Mater* **2015**, *14*, 1135.

[11] J. Jia, T. Xiong, L. Zhao, F. Wang, H. Liu, R. Hu, J. Zhou, W. Zhou, S. Chen, *ACS nano* **2017**, *11*, 12509.

[12] J. A. Kumar, P. Prakash, T. Krithiga, D. J. Amarnath, J. Premkumar, N. Rajamohan, Y. Vasseghian, P. Saravanan, M. Rajasimman, *Chemosphere* **2022**, *286*, 131607.

[13] J. Zhu, E. Ha, G. Zhao, Y. Zhou, D. Huang, G. Yue, L. Hu, N. Sun, Y. Wang, L. Y. S. Lee, *Coord. Chem. Rev.* **2017**, *352*, 306.

[14] M. Alhabeb, K. Maleski, B. Anasori, P. Lelyukh, L. Clark, S. Sin, Y. Gogotsi, *Chem. Mater.* **2017**, *29*, 7633.

[15] L. Wang, W. Tao, L. Yuan, Z. Liu, Q. Huang, Z. Chai, J. K. Gibson, W. Shi, *Chem. Commun.* **2017**, *53*, 12084.

[16] F. Jamil, H. M. Ali, M. M. Janjua, *Journal of Energy Storage* **2021**, *35*, 102322.

[17] M. Ghidiu, M. R. Lukatskaya, M.-Q. Zhao, Y. Gogotsi, M. W. Barsoum, *Nature* **2014**, *516*, 78.

[18] A. Lipatov, M. Alhabeb, M. R. Lukatskaya, A. Boson, Y. Gogotsi, A. Sinitskii, *Advanced Electronic Materials* **2016**, *2*, 1600255.

[19] W. Sun, S. Shah, Y. Chen, Z. Tan, H. Gao, T. Habib, M. Radovic, M. Green, *J. Mater. Chem. A* **2017**, *5*, 21663.

[20] S. Yang, P. Zhang, F. Wang, A. G. Ricciardulli, M. R. Lohe, P. W. Blom, X. Feng, *Angew. Chem.* **2018**, *130*, 15717.

[21] Y. Li, H. Shao, Z. Lin, J. Lu, L. Liu, B. Duployer, P. O. Persson, P. Eklund, L. Hultman, M. Li, *Nature Mater* **2020**, *19*, 894.

[22] M. Li, J. Lu, K. Luo, Y. Li, K. Chang, K. Chen, J. Zhou, J. Rosen, L. Hultman, P. Eklund, *J. Am. Chem. Soc.* **2019**, *141*, 4730.

[23] V. Kamysbayev, A. S. Filatov, H. Hu, X. Rui, F. Lagunas, D. Wang, R. F. Klie, D. V. Talapin, *Science* **2020**, *369*, 979.

[24] J. Pang, R. G. Mendes, A. Bachmatiuk, L. Zhao, H. Q. Ta, T. Gemming, H. Liu, Z. Liu, M. H. Rummeli, *Chem. Soc. Rev.* **2019**, *48*, 72.

[25] K. Maleski, V. N. Mochalin, Y. Gogotsi, *Chem. Mater.* **2017**, *29*, 1632.

[26] T. Hu, M. Hu, Z. Li, H. Zhang, C. Zhang, J. Wang, X. Wang, *PCCP* **2016**, *18*, 20256.

[27] G. Lv, J. Wang, Z. Shi, L. Fan, *Mater. Lett.* **2018**, *219*, 45.

[28] A. Qian, J. Y. Seo, H. Shi, J. Y. Lee, C. H. Chung, *ChemSusChem* **2018**, *11*, 3719.

[29] O. Mashtalir, M. Naguib, V. N. Mochalin, Y. Dall'Agnese, M. Heon, M. W. Barsoum, Y. Gogotsi, *Nat. Commun.* **2013**, *4*, 1.

[30] Y. Omomo, T. Sasaki, L. Wang, M. Watanabe, *J. Am. Chem. Soc.* **2003**, *125*, 3568.

[31] C. E. Ren, K. B. Hatzell, M. Alhabeb, Z. Ling, K. A. Mahmoud, Y. Gogotsi, *J. Phys. Chem. Lett.* **2015**, *6*, 4026.

[32] H. Wang, Y. Wu, X. Yuan, G. Zeng, J. Zhou, X. Wang, J. W. Chew, *Adv. Mater.* **2018**, *30*, 1704561.

[33] X. Xie, M.-Q. Zhao, B. Anasori, K. Maleski, C. E. Ren, J. Li, B. W. Byles, E. Pomerantseva, G. Wang, Y. Gogotsi, *Nano Energy* **2016**, *26*, 513.

[34] M. A. Hope, A. C. Forse, K. J. Griffith, M. R. Lukatskaya, M. Ghidiu, Y. Gogotsi, C. P. Grey, *PCCP* **2016**, *18*, 5099.

[35] C. A. Voigt, M. Ghidiu, V. Natu, M. W. Barsoum, *The Journal of Physical Chemistry C* **2018**, *122*, 23172.

[36] M. Naguib, R. R. Unocic, B. L. Armstrong, J. Nanda, *Dalton Trans* **2015**, *44*, 9353.

[37] I. Persson, L.-Å. Näslund, J. Halim, M. W. Barsoum, V. Darakchieva, J. Palisaitis, J. Rosen, P. O. Å. Persson, *2D Materials* **2017**, *5*, 015002.

[38] P. Lian, Y. Dong, Z.-S. Wu, S. Zheng, X. Wang, S. Wang, C. Sun, J. Qin, X. Shi, X. Bao, *Nano Energy* **2017**, *40*, 1.

[39] M. Seredych, C. E. Shuck, D. Pinto, M. Alhabeb, E. Precetti, G. Deysher, B. Anasori, N. Kurra, Y. Gogotsi, *Chem. Mater.* **2019**, *31*, 3324.

[40] J. Zhou, X. Zha, F. Y. Chen, Q. Ye, P. Eklund, S. Du, Q. Huang, *Angew. Chem. Int. Ed.* **2016**, *55*, 5008.

[41] K. Wang, Y. Zhou, W. Xu, D. Huang, Z. Wang, M. Hong, *Ceram. Int.* **2016**, *42*, 8419.

[42] Z. Li, L. Wang, D. Sun, Y. Zhang, B. Liu, Q. Hu, A. Zhou, *Materials Science and Engineering: B* **2015**, *191*, 33.

[43] H. Ghassemi, W. Harlow, O. Mashtalir, M. Beidaghi, M. Lukatskaya, Y. Gogotsi, M. L. Taheri, *J. Mater. Chem. A* **2014**, *2*, 14339.

[44] V. N. Borysiuk, V. N. Mochalin, Y. Gogotsi, *Nanotechnology* **2015**, *26*, 265705.

[45] Z. Ling, C. E. Ren, M.-Q. Zhao, J. Yang, J. M. Giammarco, J. Qiu, M. W. Barsoum, Y. Gogotsi, *PNAS* **2014**, *111*, 16676.

[46] C. Zhang, B. Anasori, A. Seral‐Ascaso, S. H. Park, N. McEvoy, A. Shmeliov, G. S. Duesberg, J. N. Coleman, Y. Gogotsi, V. Nicolosi, *Adv. Mater.* **2017**, *29*, 1702678.

[47] H. Wang, Y. Wu, J. Zhang, G. Li, H. Huang, X. Zhang, Q. Jiang, *Mater. Lett.* **2015**, *160*, 537.
[48] K. Hantanasirisakul, Y. Gogotsi, *Adv. Mater.* **2018**, *30*, 1804779.
[49] D. Xiong, X. Li, Z. Bai, S. Lu, *Small* **2018**, *14*, 1703419.
[50] C. Zhang, M. P. Kremer, A. Seral‐Ascaso, S. H. Park, N. McEvoy, B. Anasori, Y. Gogotsi, V. Nicolosi, *Adv. Funct. Mater.* **2018**, *28*, 1705506.
[51] M. R. Lukatskaya, S. Kota, Z. Lin, M.-Q. Zhao, N. Shpigel, M. D. Levi, J. Halim, P.-L. Taberna, M. W. Barsoum, P. Simon, *Nature Energy* **2017**, *2*, 1.
[52] D. Er, J. Li, M. Naguib, Y. Gogotsi, V. B. Shenoy, *Acs Appl. Mater. Interfaces* **2014**, *6*, 11173.
[53] H. Li, Y. Hou, F. Wang, M. R. Lohe, X. Zhuang, L. Niu, X. Feng, **2017**.
[54] M. Q. Zhao, C. E. Ren, Z. Ling, M. R. Lukatskaya, C. Zhang, K. L. Van Aken, M. W. Barsoum, Y. Gogotsi, *Adv. Mater.* **2015**, *27*, 339.
[55] P. Simon, *ACS nano* **2017**, *11*, 2393.
[56] F. Bu, M. M. Zagho, Y. Ibrahim, B. Ma, A. Elzatahry, D. Zhao, *Nano Today* **2020**, *30*, 100803.
[57] M. Q. Zhao, X. Xie, C. E. Ren, T. Makaryan, B. Anasori, G. Wang, Y. Gogotsi, *Adv. Mater.* **2017**, *29*, 1702410.
[58] X. Li, X. Yin, H. Xu, M. Han, M. Li, S. Liang, L. Cheng, L. Zhang, *Acs Appl. Mater. Interfaces* **2018**, *10*, 34524.
[59] C. E. Ren, M. Q. Zhao, T. Makaryan, J. Halim, M. Boota, S. Kota, B. Anasori, M. W. Barsoum, Y. Gogotsi, *ChemElectroChem* **2016**, *3*, 689.
[60] T. Placke, A. Heckmann, R. Schmuch, P. Meister, K. Beltrop, M. Winter, *Joule* **2018**, *2*, 2528.
[61] Y. Sui, C. Liu, R. C. Masse, Z. G. Neale, M. Atif, M. AlSalhi, G. Cao, *Energy Storage Mater.* **2020**, *25*, 1.
[62] D. Bin, F. Wang, A. G. Tamirat, L. Suo, Y. Wang, C. Wang, Y. Xia, *Adv. Energy Mater.* **2018**, *8*, 1703008.
[63] R. Borah, F. Hughson, J. Johnston, T. Nann, *Materials Today Advances* **2020**, *6*, 100046.
[64] A. Manthiram, *Nat. Commun.* **2020**, *11*, 1.
[65] B. Dunn, H. Kamath, J.-M. Tarascon, *Science* **2011**, *334*, 928.
[66] C. Choi, D. S. Ashby, D. M. Butts, R. H. DeBlock, Q. Wei, J. Lau, B. Dunn, *Nature Reviews Materials* **2020**, *5*, 5.
[67] D. Qu, AIP Conference Proceedings, American Institute of Physics: **2014**; pp 14.
[68] A. Manthiram, *ACS central science* **2017**, *3*, 1063.
[69] A. Vu, Y. Qian, A. Stein, *Adv. Energy Mater.* **2012**, *2*, 1056.
[70] M. D. Levi, D. Aurbach, *The Journal of Physical Chemistry B* **1997**, *101*, 4641.
[71] N. S. Ergang, J. C. Lytle, H. Yan, A. Stein, *J. Electrochem. Soc.* **2005**, *152*, A1989.
[72] H. Yamada, T. Yamato, I. Moriguchi, T. Kudo, *Solid State Ionics* **2004**, *175*, 195.
[73] I. Moriguchi, R. Hidaka, H. Yamada, T. Kudo, H. Murakami, N. Nakashima, *Adv. Mater.* **2006**, *18*, 69.

[74] M. Wakihara, O. Yamamoto, *Lithium ion batteries: fundamentals and performance*. John Wiley & Sons: **2008**.
[75] C. Cachet, R. Wiart, *Electrochim. Acta* **1984**, *29*, 145.
[76] M. Rahman, Y. C. Wong, G. Song, C. Wen, *J. Porous Mater.* **2015**, *22*, 1313.
[77] S. W. Oh, S.-T. Myung, S.-M. Oh, C. S. Yoon, K. Amine, Y.-K. Sun, *Electrochim. Acta* **2010**, *55*, 1193.
[78] L. Beaulieu, T. Hatchard, A. Bonakdarpour, M. Fleischauer, J. Dahn, *J. Electrochem. Soc.* **2003**, *150*, A1457.
[79] S. Chu, A. Majumdar, *Nature* **2012**, *488*, 294.
[80] X. Wang, Y. L. Ding, Y. P. Deng, Z. Chen, *Adv. Energy Mater.* **2020**, *10*, 1903864.
[81] T. Or, S. W. Gourley, K. Kaliyappan, A. Yu, Z. Chen, *Carbon Energy* **2020**.
[82] G. L. Zhu, C. Z. Zhao, J. Q. Huang, C. He, J. Zhang, S. Chen, L. Xu, H. Yuan, Q. Zhang, *Small* **2019**, *15*, 1805389.
[83] Y. Chen, Y. Kang, Y. Zhao, L. Wang, J. Liu, Y. Li, Z. Liang, X. He, X. Li, N. Tavajohi, *J. Energy Chem.* **2021**, *59*, 83.
[84] L. Đorđević, F. Arcudi, M. Prato, *Nat. Protoc.* **2019**, *14*, 2931. DOI 10.1038/s41596-019-0207-x.
[85] T. T. D. Nguyen, S. Abada, A. Lecocq, J. Bernard, M. Petit, G. Marlair, S. Grugeon, S. Laruelle, *World Electric Vehicle Journal* **2019**, *10*, 79.
[86] H. Xu, C. Peng, Y. Yan, F. Dong, H. Sun, J. Yang, S. Zheng, *Carbon Energy* **2019**, *1*, 276.
[87] M. Li, C. Wang, Z. Chen, K. Xu, J. Lu, *Chem. Rev.* **2020**.
[88] J. Wu, Y. Cao, H. Zhao, J. Mao, Z. Guo, *Carbon Energy* **2019**, *1*, 57.
[89] S. Chen, D. Wang, Y. Zhao, D. Wang, *Small Methods* **2018**, *2*, 1800038.
[90] J. Meng, Q. Pang, L. Mai, *Matter* **2020**, *2*, 1363.
[91] Y. P. Deng, Z. G. Wu, R. Liang, Y. Jiang, D. Luo, A. Yu, Z. Chen, *Adv. Funct. Mater.* **2019**, *29*, 1808522.
[92] R. Paul, Q. Dai, C. Hu, L. Dai, *Carbon Energy* **2019**, *1*, 19.
[93] K. Kaliyappan, T. Or, Y. P. Deng, Y. Hu, Z. Bai, Z. Chen, *Adv. Funct. Mater.* **2020**, *30*, 1910251.
[94] S. Lou, Y. Zhao, J. Wang, G. Yin, C. Du, X. Sun, *Small* **2019**, *15*, 1904740.
[95] J. Fu, R. Liang, G. Liu, A. Yu, Z. Bai, L. Yang, Z. Chen, *Adv. Mater.* **2019**, *31*, 1805230.
[96] G. Li, F. Lu, X. Dou, X. Wang, D. Luo, H. Sun, A. Yu, Z. Chen, *J. Am. Chem. Soc.* **2020**, *142*, 3583.
[97] W. Shin, J. Lu, X. Ji, *Carbon Energy* **2019**, *1*, 165.
[98] X. Y. Fan, J. Han, Y. L. Ding, Y. P. Deng, D. Luo, X. Zeng, Z. Jiang, L. Gou, D. L. Li, Z. Chen, *Adv. Energy Mater.* **2019**, *9*, 1900673.
[99] H. Yuan, J. Nai, H. Tian, Z. Ju, W. Zhang, Y. Liu, X. Tao, X. W. D. Lou, *Sci. Adv.* **2020**, *6*, eaaz3112.
[100] C. Y. Chan, P.-K. Lee, Z. Xu, Y. Denis, *Electrochim. Acta* **2018**, *263*, 34.
[101] J. Xu, Y. Dou, Z. Wei, J. Ma, Y. Deng, Y. Li, H. Liu, S. Dou, *Adv. Sci.* **2017**, *4*, 1700146.

[102] M. Wang, Y. Tang, *Adv. Energy Mater.* **2018**, *8*, 1703320.
[103] X. Yang, J. Luo, X. Sun, *Chem. Soc. Rev.* **2020**, *49*, 2140.
[104] I. A. Rodríguez-Pérez, X. Ji, *ACS Energy Lett.* **2017**, *2*, 1762.
[105] P. Arora, Z. Zhang, *Chem. Rev.* **2004**, *104*, 4419.
[106] X. Zhou, Q. Liu, C. Jiang, B. Ji, X. Ji, Y. Tang, H. M. Cheng, *Angew. Chem. Int. Ed.* **2020**, *59*, 3802.
[107] T. Placke, S. Rothermel, O. Fromm, P. Meister, S. F. Lux, J. Huesker, H.-W. Meyer, M. Winter, *J. Electrochem. Soc.* **2013**, *160*, A1979.
[108] M. E. Speer, M. Kolek, J. J. Jassoy, J. Heine, M. Winter, P. M. Bieker, B. Esser, *Chem. Commun.* **2015**, *51*, 15261.
[109] M. L. Aubrey, J. R. Long, *J. Am. Chem. Soc.* **2015**, *137*, 13594.
[110] J. Kasnatscheew, T. Placke, B. Streipert, S. Rothermel, R. Wagner, P. Meister, I. C. Laskovic, M. Winter, *J. Electrochem. Soc.* **2017**, *164*, A2479.
[111] X. Yao, Y. Ke, W. Ren, X. Wang, F. Xiong, W. Yang, M. Qin, Q. Li, L. Mai, *Adv. Energy Mater.* **2019**, *9*, 1803260.
[112] L. Zhang, H. Wang, X. Zhang, Y. Tang, *Adv. Funct. Mater.* **2021**, *31*, 2010958.
[113] M. Zhang, M. Shoaib, H. Fei, T. Wang, J. Zhong, L. Fan, L. Wang, H. Luo, S. Tan, Y. Wang, *Adv. Energy Mater.* **2019**, *9*, 1901663.
[114] X. Wang, S. Wang, K. Shen, S. He, X. Hou, F. Chen, *J. Mater. Chem. A* **2020**, *8*, 4007.
[115] H. Tan, D. Chen, X. Rui, Y. Yu, *Adv. Funct. Mater.* **2019**, *29*, 1808745.
[116] X. Zhang, D. Wang, X. Qiu, Y. Ma, D. Kong, K. Müllen, X. Li, L. Zhi, *Nat. Commun.* **2020**, *11*, 1.
[117] S. He, S. Wang, H. Chen, X. Hou, Z. Shao, *J. Mater. Chem. A* **2020**, *8*, 2571.
[118] S. Li, J. Niu, Y. C. Zhao, K. P. So, C. Wang, C. A. Wang, J. Li, *Nat. Commun.* **2015**, *6*, 1.
[119] K. Wang, X. Li, Y. Xie, J. He, Z. Yang, X. Shen, N. Wang, C. Huang, *Acs Appl. Mater. Interfaces* **2019**, *11*, 23990.
[120] C. Song, Y. Li, H. Li, T. He, Q. Guan, J. Yang, X. Li, J. Cheng, B. Wang, *Nano Energy* **2019**, *60*, 285.
[121] M. Li, X. Bi, R. Wang, Y. Li, G. Jiang, L. Li, C. Zhong, Z. Chen, J. Lu, *Matter* **2020**, *2*, 32.
[122] M. M. Huie, D. C. Bock, E. S. Takeuchi, A. C. Marschilok, K. J. Takeuchi, *Coord. Chem. Rev.* **2015**, *287*, 15.
[123] P. Padigi, G. Goncher, D. Evans, R. Solanki, *J. Power Sources* **2015**, *273*, 460.
[124] Q. Li, N. J. Bjerrum, *J. Power Sources* **2002**, *110*, 1.
[125] T. Cai, L. Zhao, H. Hu, T. Li, X. Li, S. Guo, Y. Li, Q. Xue, W. Xing, Z. Yan, *Energy Environ. Sci.* **2018**, *11*, 2341.
[126] C. Li, X. Zhang, W. He, G. Xu, R. Sun, *J. Power Sources* **2020**, *449*, 227596.
[127] Y. Liang, H. Dong, D. Aurbach, Y. Yao, *Nature Energy* **2020**, *5*, 646.
[128] A. Konarov, N. Voronina, J. H. Jo, Z. Bakenov, Y.-K. Sun, S.-T. Myung, *ACS Energy Lett.* **2018**, *3*, 2620.
[129] G. Fang, J. Zhou, A. Pan, S. Liang, *ACS Energy Lett.* **2018**, *3*, 2480.

[130] F. Cheng, J. Chen, X. Gou, P. Shen, *Adv. Mater.* **2005**, *17*, 2753.
[131] T. Reddy, *Linden's Handbook of Batteries, 4th Edition*. McGraw-Hill Education: **2010**.
[132] T. Shoji, M. Hishinuma, T. Yamamoto, *J. Appl. Electrochem.* **1988**, *18*, 521.
[133] C. Xu, B. Li, H. Du, F. Kang, *Angew. Chem. Int. Ed.* **2012**, *51*, 933.
[134] H. Li, C. Xu, C. Han, Y. Chen, C. Wei, B. Li, F. Kang, *J. Electrochem. Soc.* **2015**, *162*, A1439.
[135] Y.-P. Deng, R. Liang, G. Jiang, Y. Jiang, A. Yu, Z. Chen, *ACS Energy Lett.* **2020**, *5*, 1665.
[136] T. Yamamoto, T. Shoji, *Inorg. Chim. Acta* **1986**, *117*, L27.
[137] J. Ming, J. Guo, C. Xia, W. Wang, H. N. Alshareef, *Mater. Sci. Eng., R* **2019**, *135*, 58.
[138] D. Selvakumaran, A. Pan, S. Liang, G. Cao, *J. Mater. Chem. A* **2019**, *7*, 18209.
[139] Y. Zhao, Y. Zhu, X. Zhang, *InfoMat* **2020**, *2*, 237.
[140] F. Wan, Z. Niu, *Angew. Chem. Int. Ed.* **2019**, *58*, 16358.
[141] J. O. Besenhard, *Handbook of battery materials*. John Wiley & Sons: **2008**.
[142] N. Zhang, F. Cheng, J. Liu, L. Wang, X. Long, X. Liu, F. Li, J. Chen, *Nat. Commun.* **2017**, *8*, 1.
[143] B. Wu, G. Zhang, M. Yan, T. Xiong, P. He, L. He, X. Xu, L. Mai, *Small* **2018**, *14*, 1703850.
[144] S. Zhao, B. Han, D. Zhang, Q. Huang, L. Xiao, L. Chen, D. G. Ivey, Y. Deng, W. Wei, *J. Mater. Chem. A* **2018**, *6*, 5733.
[145] Y. Li, S. Wang, J. R. Salvador, J. Wu, B. Liu, W. Yang, J. Yang, W. Zhang, J. Liu, J. Yang, *Chem. Mater.* **2019**, *31*, 2036.
[146] S.-D. Han, S. Kim, D. Li, V. Petkov, H. D. Yoo, P. J. Phillips, H. Wang, J. J. Kim, K. L. More, B. Key, *Chem. Mater.* **2017**, *29*, 4874.
[147] M. H. Alfaruqi, V. Mathew, J. Gim, S. Kim, J. Song, J. P. Baboo, S. H. Choi, J. Kim, *Chem. Mater.* **2015**, *27*, 3609.
[148] H. Pan, Y. Shao, P. Yan, Y. Cheng, K. S. Han, Z. Nie, C. Wang, J. Yang, X. Li, P. Bhattacharya, *Nature Energy* **2016**, *1*, 16039.
[149] N. Zhang, Y. Dong, M. Jia, X. Bian, Y. Wang, M. Qiu, J. Xu, Y. Liu, L. Jiao, F. Cheng, *ACS Energy Lett.* **2018**, *3*, 1366.
[150] J. Ding, Z. Du, L. Gu, B. Li, L. Wang, S. Wang, Y. Gong, S. Yang, *Adv. Mater.* **2018**, *30*, 1800762.
[151] P. Hu, M. Yan, T. Zhu, X. Wang, X. Wei, J. Li, L. Zhou, Z. Li, L. Chen, L. Mai, *Acs Appl. Mater. Interfaces* **2017**, *9*, 42717.
[152] M. Yan, P. He, Y. Chen, S. Wang, Q. Wei, K. Zhao, X. Xu, Q. An, Y. Shuang, Y. Shao, *Adv. Mater.* **2018**, *30*, 1703725.
[153] F. Wan, L. Zhang, X. Dai, X. Wang, Z. Niu, J. Chen, *Nat. Commun.* **2018**, *9*, 1.
[154] F. Ming, H. Liang, Y. Lei, S. Kandambeth, M. Eddaoudi, H. N. Alshareef, *ACS Energy Lett.* **2018**, *3*, 2602.
[155] D. Xu, H. Wang, F. Li, Z. Guan, R. Wang, B. He, Y. Gong, X. Hu, *Adv. Mater. Interfaces* **2019**, *6*, 1801506.

[156] M. H. Wong, Z. Zhang, X. Yang, X. Chen, J. Y. J. C. C. Ying, **2015**, *51*, 13674.
[157] Y. Lu, L. Wang, J. Cheng, J. B. J. C. c. Goodenough, **2012**, *48*, 6544.
[158] Y. You, X.-L. Wu, Y.-X. Yin, Y.-G. J. E. Guo, E. Science, **2014**, *7*, 1643.
[159] G. He, L. F. J. A. E. L. Nazar, **2017**, *2*, 1122.
[160] T. Tojo, Y. Sugiura, R. Inada, Y. Sakurai, *Electrochim. Acta* **2016**, *207*, 22.
[161] L. Reed, S. Ortiz, M. Xiong, E. Menke, *Chem. Commun.* **2015**, *51*, 14397.
[162] L. Chen, J. Bao, X. Dong, D. G. Truhlar, Y. Wang, C. Wang, Y. Xia, *ACS Energy Lett.* **2017**, *2*, 1115.
[163] Z. Liu, G. Pulletikurthi, F. Endres, *Acs Appl. Mater. Interfaces* **2016**, *8*, 12158.
[164] F. Ma, Q. Li, T. Wang, H. Zhang, G. Wu, *Sci. Bull.* **2017**, *62*, 358.
[165] M. Song, H. Tan, D. Chao, H. J. Fan, *Adv. Funct. Mater.* **2018**, *28*, 1802564.
[166] B. Wang, Y. Han, X. Wang, N. Bahlawane, H. Pan, M. Yan, Y. Jiang, *Iscience* **2018**, *3*, 110.
[167] L. Zhang, L. Chen, X. Zhou, Z. Liu, *Adv. Energy Mater.* **2015**, *5*, 1400930.
[168] L. Zhang, L. Chen, X. Zhou, Z. Liu, *Sci. Rep.* **2015**, *5*, 1.
[169] R. Trócoli, F. La Mantia, *ChemSusChem* **2015**, *8*, 481.
[170] L. Ma, S. Chen, C. Long, X. Li, Y. Zhao, Z. Liu, Z. Huang, B. Dong, J. A. Zapien, C. Zhi, *Adv. Energy Mater.* **2019**, *9*, 1902446.
[171] G. Zampardi, F. La Mantia, *Current Opinion in Electrochemistry* **2020**, *21*, 84.
[172] S. Li, Y. Dong, L. Xu, X. Xu, L. He, L. Mai, *Adv. Mater.* **2014**, *26*, 3545.
[173] D. Kundu, P. Oberholzer, C. Glaros, A. Bouzid, E. Tervoort, A. Pasquarello, M. Niederberger, *Chem. Mater.* **2018**, *30*, 3874.
[174] Y. Cheng, L. Luo, L. Zhong, J. Chen, B. Li, W. Wang, S. X. Mao, C. Wang, V. L. Sprenkle, G. Li, *Acs Appl. Mater. Interfaces* **2016**, *8*, 13673.
[175] P. He, M. Yan, G. Zhang, R. Sun, L. Chen, Q. An, L. Mai, *Adv. Energy Mater.* **2017**, *7*, 1601920.
[176] C. Li, X. Zhang, W. He, G. Xu, R. J. J. o. P. S. Sun, **2020**, *449*, 227596.
[177] Y. Zeng, X. Zhang, R. Qin, X. Liu, P. Fang, D. Zheng, Y. Tong, X. Lu, *Adv. Mater.* **2019**, *31*, 1903675.
[178] H. Wang, R. Tan, Z. Yang, Y. Feng, X. Duan, J. Ma, *Adv. Energy Mater.* **2021**, *11*, 2000962.
[179] Q. Zhang, J. Luan, Y. Tang, X. Ji, H. Wang, *Angew. Chem. Int. Ed.* **2020**, *59*, 13180.
[180] K. E. Sun, T. K. Hoang, T. N. L. Doan, Y. Yu, X. Zhu, Y. Tian, P. Chen, *Acs Appl. Mater. Interfaces* **2017**, *9*, 9681.
[181] F. Wang, O. Borodin, T. Gao, X. Fan, W. Sun, F. Han, A. Faraone, J. A. Dura, K. Xu, C. Wang, *Nature Mater* **2018**, *17*, 543.
[182] J. Park, A. Papoutsi, R. T. Ash, M. A. Marin, P. Poirazi, S. M. Smirnakis, *Nat. Commun.* **2019**, *10*, 1.
[183] K. Shi, M. Ren, I. Zhitomirsky, *ACS Sustainable Chemistry & Engineering* **2014**, *2*, 1289.
[184] K. Zhao, C. Wang, Y. Yu, M. Yan, Q. Wei, P. He, Y. Dong, Z. Zhang, X. Wang, L. Mai, *Adv. Mater. Interfaces* **2018**, *5*, 1800848.

[185] L. Kang, M. Cui, F. Jiang, Y. Gao, H. Luo, J. Liu, W. Liang, C. Zhi, *Adv. Energy Mater.* **2018**, *8*, 1801090.
[186] Z. Cao, P. Zhuang, X. Zhang, M. Ye, J. Shen, P. M. Ajayan, *Adv. Energy Mater.* **2020**, *10*, 2001599.
[187] Q. Yang, Q. Li, Z. Liu, D. Wang, Y. Guo, X. Li, Y. Tang, H. Li, B. Dong, C. Zhi, *Adv. Mater.* **2020**, *32*, 2001854.
[188] Q. Zhang, J. Luan, L. Fu, S. Wu, Y. Tang, X. Ji, H. Wang, *Angew. Chem.* **2019**, *131*, 15988.
[189] Y. Yin, S. Wang, Q. Zhang, Y. Song, N. Chang, Y. Pan, H. Zhang, X. Li, *Adv. Mater.* **2020**, *32*, 1906803.
[190] X. Chen, X.-R. Chen, T.-Z. Hou, B.-Q. Li, X.-B. Cheng, R. Zhang, Q. Zhang, *Sci. Adv.* **2019**, *5*, eaau7728.
[191] W. Doh, V. Papaefthimiou, S. Zafeiratos, *Surface science tools for nanomaterials characterization* **2015**, 317.
[192] J. Halim, K. M. Cook, M. Naguib, P. Eklund, Y. Gogotsi, J. Rosen, M. W. Barsoum, *Appl. Surf. Sci.* **2016**, *362*, 406.
[193] X. Wang, X. Fan, M. Li, W. Zhu, J. Xue, F. Ye, L. Cheng, *Ceram. Int.* **2021**, *47*, 13628.
[194] L. Ding, Y. Wei, Y. Wang, H. Chen, J. Caro, H. Wang, *Angew. Chem. Int. Ed.* **2017**, *56*, 1825.
[195] C. H. van Oversteeg, H. Q. Doan, F. M. de Groot, T. Cuk, *Chem. Soc. Rev.* **2017**, *46*, 102.
[196] K. Chokprasombat, C. Sirisathitkul, P. Harding, S. Chandarak, R. Yimnirun, *Journal of Nanomaterials* **2012**, *2012*.
[197] M. Agote-Arán, I. Lezcano-González, A. G. Greenaway, S. Hayama, S. Díaz-Moreno, A. B. Kroner, A. M. Beale, *Applied Catalysis A: General* **2019**, *570*, 283.
[198] A. K. Fard, G. Mckay, R. Chamoun, T. Rhadfi, H. Preud'Homme, M. A. Atieh, *Chem. Eng. J.* **2017**, *317*, 331.
[199] R. Hebbar, A. Isloor, A. Ismail, Contact angle measurements. In *Membrane characterization*, Elsevier: 2017; pp 219.
[200] M. Naguib, J. Come, B. Dyatkin, V. Presser, P.-L. Taberna, P. Simon, M. W. Barsoum, Y. Gogotsi, *Electrochem. Commun.* **2012**, *16*, 61.
[201] X. Huang, Z. Wang, R. Knibbe, B. Luo, S. A. Ahad, D. Sun, L. Wang, *Energy Technology* **2019**, *7*, 1801001.
[202] W. Choi, H.-C. Shin, J. M. Kim, J.-Y. Choi, W.-S. Yoon, *Journal of Electrochemical Science and Technology* **2020**, *11*, 1.
[203] S. Bellani, F. Wang, G. Longoni, L. Najafi, R. Oropesa-Nunez, A. E. Del Rio Castillo, M. Prato, X. Zhuang, V. Pellegrini, X. Feng, *Nano Lett.* **2018**, *18*, 7155.
[204] C. Jiang, L. Xiang, S. Miao, L. Shi, D. Xie, J. Yan, Z. Zheng, X. Zhang, Y. Tang, *Adv. Mater.* **2020**, *32*, 1908470.
[205] S. Rothermel, P. Meister, G. Schmuelling, O. Fromm, H.-W. Meyer, S. Nowak, M. Winter, T. Placke, *Energy Environ. Sci.* **2014**, *7*, 3412.
[206] Y. Dong, H. Shi, Z. S. Wu, *Adv. Funct. Mater.* **2020**, *30*, 2000706.

[207] P. Zhang, R. A. Soomro, Z. Guan, N. Sun, B. Xu, *Energy Storage Mater.* **2020**.

[208] O. Mashtalir, M. R. Lukatskaya, M. Q. Zhao, M. W. Barsoum, Y. Gogotsi, *Adv. Mater.* **2015**, *27*, 3501.

[209] M.-Q. Zhao, M. Torelli, C. E. Ren, M. Ghidiu, Z. Ling, B. Anasori, M. W. Barsoum, Y. Gogotsi, *Nano Energy* **2016**, *30*, 603.

[210] C. Chen, M. Boota, X. Xie, M. Zhao, B. Anasori, C. E. Ren, L. Miao, J. Jiang, Y. Gogotsi, *J. Mater. Chem. A* **2017**, *5*, 5260.

[211] M. Boota, B. Anasori, C. Voigt, M. Q. Zhao, M. W. Barsoum, Y. Gogotsi, *Adv. Mater.* **2016**, *28*, 1517.

[212] X. Xie, K. Kretschmer, B. Anasori, B. Sun, G. Wang, Y. Gogotsi, *ACS Applied Nano Materials* **2018**, *1*, 505.

[213] Y. Li, H. Shao, Z. Lin, J. Lu, L. Liu, B. Duployer, P. O. Persson, P. Eklund, L. Hultman, M. Li, *Nature Mater* **2020**, 1.

[214] L.-Y. Xiu, Z.-Y. Wang, J.-S. Qiu, *Rare Metals* **2020**, *39*, 1237.

[215] S. Kajiyama, L. Szabova, H. Iinuma, A. Sugahara, K. Gotoh, K. Sodeyama, Y. Tateyama, M. Okubo, A. Yamada, *Adv. Energy Mater.* **2017**, *7*, 1601873.

[216] B. Ravel, M. Newville, *J Synchrotron Radiat* **2005**, *12*, 537.

[217] M. Zhang, Y. Pei, W. Liu, R. Liang, Y.-P. Deng, Z. Chen, A. Yu, *Nano Energy 81*, 105643.

[218] J. P. Perdew, K. Burke, M. Ernzerhof, *Phys. Rev. Lett.* **1996**, *77*, 3865.

[219] Y. Wang, M. Zhou, L.-C. Xu, W. Zhao, R. Li, Z. Yang, R. Liu, X. Li, *J. Power Sources* **2020**, *451*, 227791.

[220] Y.-P. Deng, Y. Jiang, R. Liang, S.-J. Zhang, D. Luo, Y. Hu, X. Wang, J.-T. Li, A. Yu, Z. Chen, *Nat. Commun.* **2020**, *11*, 1.

[221] S. Subrahmanyan. An investigation of pore collapse in asymmetric polysulfone membranes. Virginia Tech, **2003**.

[222] A. Abdulraheem, J.-C. Roegiers, M. Zaman, The 33th US Symposium on Rock Mechanics (USRMS), American Rock Mechanics Association: **1992**.

[223] S. J. Shaw, G. S. Perry, *Thermochim. Acta* **1990**, *157*, 329.

[224] J. Luo, X. Tao, J. Zhang, Y. Xia, H. Huang, L. Zhang, Y. Gan, C. Liang, W. Zhang, *ACS nano* **2016**, *10*, 2491.

[225] Y. Dall'Agnese, P. Rozier, P.-L. Taberna, Y. Gogotsi, P. Simon, *J. Power Sources* **2016**, *306*, 510.

[226] M. Naguib, R. A. Adams, Y. Zhao, D. Zemlyanov, A. Varma, J. Nanda, V. G. Pol, *Chem. Commun.* **2017**, *53*, 6883.

[227] F. Du, H. Tang, L. Pan, T. Zhang, H. Lu, J. Xiong, J. Yang, C. J. Zhang, *Electrochim. Acta* **2017**, *235*, 690.

[228] Z. Ma, X. Zhou, W. Deng, D. Lei, Z. Liu, *Acs Appl. Mater. Interfaces* **2018**, *10*, 3634.

[229] M. Zhang, W. Liu, R. Liang, R. Tjandra, A. Yu, *Sustainable Energy & Fuels* **2019**, *3*, 2499.

[230] S. J. Kim, M. Naguib, M. Zhao, C. Zhang, H.-T. Jung, M. W. Barsoum, Y. Gogotsi, *Electrochim. Acta* **2015**, *163*, 246.

[231] D. Sun, M. Wang, Z. Li, G. Fan, L.-Z. Fan, A. Zhou, *Electrochem. Commun.* **2014**, *47*, 80.

[232] C. Zhang, S. J. Kim, M. Ghidiu, M. Q. Zhao, M. W. Barsoum, V. Nicolosi, Y. Gogotsi, *Adv. Funct. Mater.* **2016**, *26*, 4143.

[233] F. Kong, X. He, Q. Liu, X. Qi, D. Sun, Y. Zheng, R. Wang, Y. Bai, *Electrochem. Commun.* **2018**, *97*, 16.

[234] V. Schier, H.-J. Michel, J. Halbritter, *Fresenius' journal of analytical chemistry* **1993**, *346*, 227.

[235] E. Magni, G. A. Somorjai, *Surf. Sci.* **1996**, *345*, 1.

[236] C. Mousty‐Desbuquoit, J. Riga, J. J. Verbist, *The Journal of Chemical Physics* **1983**, *79*, 26.

[237] Y. Cao, Q. Deng, Z. Liu, D. Shen, T. Wang, Q. Huang, S. Du, N. Jiang, C.-T. Lin, J. Yu, *RSC Adv.* **2017**, *7*, 20494.

[238] J. Tang, T. S. Mathis, N. Kurra, A. Sarycheva, X. Xiao, M. N. Hedhili, Q. Jiang, H. N. Alshareef, B. Xu, F. Pan, *Angew. Chem. Int. Ed.* **2019**, *58*, 17849.

[239] J. Yan, C. E. Ren, K. Maleski, C. B. Hatter, B. Anasori, P. Urbankowski, A. Sarycheva, Y. Gogotsi, *Adv. Funct. Mater.* **2017**, *27*, 1701264.

[240] B. Gupta, N. Kumar, K. Panda, V. Kanan, S. Joshi, I. Visoly-Fisher, *Sci. Rep.* **2017**, *7*, 1.

[241] M. Magnuson, L.-Å. Näslund, *Physical Review Research* **2020**, *2*, 033516.

[242] M. R. Lukatskaya, S. M. Bak, X. Yu, X. Q. Yang, M. W. Barsoum, Y. Gogotsi, *Adv. Energy Mater.* **2015**, *5*, 1500589.

[243] C. Shi, M. Beidaghi, M. Naguib, O. Mashtalir, Y. Gogotsi, S. J. Billinge, *Phys. Rev. Lett.* **2014**, *112*, 125501.

[244] J. Lu, I. Persson, H. Lind, J. Palisaitis, M. Li, Y. Li, K. Chen, J. Zhou, S. Du, Z. Chai, *Nanoscale Advances* **2019**, *1*, 3680.

[245] Y. Bai, K. Zhou, N. Srikanth, J. H. Pang, X. He, R. Wang, *RSC Adv.* **2016**, *6*, 35731.

[246] V. Shukla, N. K. Jena, S. R. Naqvi, W. Luo, R. Ahuja, *Nano Energy* **2019**, *58*, 877.

[247] Y. Xie, P. Kent, *Phys Rev B* **2013**, *87*, 235441.

[248] Y.-X. Yu, *The Journal of Physical Chemistry C* **2016**, *120*, 5288.

[249] X. Tong, F. Zhang, G. Chen, X. Liu, L. Gu, Y. J. A. E. M. Tang, **2018**, *8*, 1701967.

[250] M. Sheng, F. Zhang, B. Ji, X. Tong, Y. Tang, *Adv. Energy Mater.* **2017**, *7*, 1601963.

[251] Y. Liu, X. Hu, G. Zhong, J. Chen, H. Zhan, Z. Wen, *J. Mater. Chem. A* **2019**, *7*, 24271.

[252] L.-N. Wu, S.-Y. Shen, Y.-H. Hong, C.-H. Shen, F.-M. Han, F. Fu, X.-D. Zhou, L. Huang, J.-T. Li, S.-G. Sun, *Acs Appl. Mater. Interfaces* **2019**, *11*, 12570.

[253] D. Yu, L. Cheng, M. Chen, J. Wang, W. Zhou, W. Wei, H. Wang, *Acs Appl. Mater. Interfaces* **2019**, *11*, 45755.

[254] N. Gunawardhana, G.-J. Park, A. K. Thapa, N. Dimov, M. Sasidharan, H. Nakamura, M. Yoshio, *J. Power Sources* **2012**, *203*, 257.

[255] L. Fan, Q. Liu, S. Chen, Z. Xu, B. Lu, *Adv. Energy Mater.* **2017**, *7*, 1602778.

[256] B. Tang, L. Shan, S. Liang, J. Zhou, *Energy Environ. Sci.* **2019**, *12*, 3288.

[257] M. Zhang, R. Liang, T. Or, Y.-P. Deng, A. Yu, Z. Chen, *Small Structures*, 2000064.

[258] L. Ma, S. Chen, N. Li, Z. Liu, Z. Tang, J. A. Zapien, S. Chen, J. Fan, C. Zhi, *Adv. Mater.* **2020**, *32*, 1908121.

[259] Z. Li, T. Liu, R. Meng, L. Gao, Y. Zou, P. Peng, Y. Shao, X. Liang, *Energy & Environmental Materials* **2021**, *4*, 111.

[260] T. Cao, F. Zhang, M. Chen, T. Shao, Z. Li, Q. Xu, D. Cheng, H. Liu, Y. Xia, *Acs Appl. Mater. Interfaces* **2021**.

[261] Z. Zhang, J.-G. Wang, B. Wei, *Nanomaterials* **2017**, *7*, 228.

[262] X. Wu, M. Sun, S. Guo, J. Qian, Y. Liu, Y. Cao, X. Ai, H. Yang, *ChemNanoMat* **2015**, *1*, 188.

[263] G. Du, H. Pang, *Energy Storage Mater.* **2021**.

[264] X. Zhu, Z. Cao, W. Wang, H. Li, J. Dong, S. Gao, D. Xu, L. Li, J. Shen, M. Ye, *ACS nano* **2021**, *15*, 2971.

[265] M. Zhang, R. Liang, N. Yang, R. Gao, Y. Zheng, Y. P. Deng, Y. Hu, A. Yu, Z. Chen, *Adv. Energy Mater.* **2021**, 2102493.

[266] Y. Liu, Z. Dai, W. Zhang, Y. Jiang, J. Peng, D. Wu, B. Chen, W. Wei, X. Chen, Z. Liu, *ACS nano* **2021**, *15*, 9065.

[267] H. Ming, N. L. Torad, Y.-D. Chiang, K. C.-W. Wu, Y. Yamauchi, *CrystEngComm* **2012**, *14*, 3387.

[268] F. Qu, A. Shi, M. Yang, J. Jiang, G. Shen, R. Yu, *Anal. Chim. Acta* **2007**, *605*, 28.

[269] M. B. Zakaria, T. Chikyow, *Coord. Chem. Rev.* **2017**, *352*, 328.

[270] N. Yamamoto, T. Okuhara, T. Nakato, *J. Mater. Chem.* **2001**, *11*, 1858.

[271] K. A. Colwell, M. N. Jackson, R. M. Torres-Gavosto, S. Jawahery, B. Vlaisavljevich, J. M. Falkowski, B. Smit, S. C. Weston, J. R. Long, *J. Am. Chem. Soc.* **2021**, *143*, 5044.

[272] Y. Feng, M. Sakaki, J.-h. Kim, J. Huang, K. Kajiyoshi, *New J. Chem.* **2018**, *42*, 20212.

[273] J. Nai, S. Wang, X. W. D. Lou, *Sci. Adv.* **2019**, *5*, eaax5095.

[274] H.-P. Lin, S.-T. Wong, C.-Y. Mou, C.-Y. Tang, *The Journal of Physical Chemistry B* **2000**, *104*, 8967.

[275] Y. Fu, Q. Wei, G. Zhang, X. Wang, J. Zhang, Y. Hu, D. Wang, L. Zuin, T. Zhou, Y. Wu, *Adv. Energy Mater.* **2018**, *8*, 1801445.

[276] Y. Kang, S. Wang, K. Hui, H.-F. Li, F. Liang, X.-L. Wu, Q. Zhang, W. Zhou, L. Chen, F. Chen, *Materials Today Energy* **2021**, *20*, 100572.

[277] S. Luo, L. Xie, F. Han, W. Wei, Y. Huang, H. Zhang, M. Zhu, O. G. Schmidt, L. Wang, *Adv. Funct. Mater.* **2019**, *29*, 1901336.

[278] W. H. Lie, C. Deng, Y. Yang, C. Tsounis, K.-H. Wu, M. V. C. Hioe, N. M. Bedford, D.-W. Wang, *Green Chem* **2021**.

[279] A. Bordage, R. Moulin, E. Fonda, G. Fornasieri, E. Rivière, A. Bleuzen, *J. Am. Chem. Soc.* **2018**, *140*, 10332.

[280] J. Qian, C. Wu, Y. Cao, Z. Ma, Y. Huang, X. Ai, H. Yang, *Adv. Energy Mater.* **2018**, *8*, 1702619.

[281] C. Li, R. Zang, P. Li, Z. Man, S. Wang, X. Li, Y. Wu, S. Liu, G. Wang, *Chemistry–An Asian Journal* **2018**, *13*, 342.

[282] C. Chankhantha, P. Thanasuthipitak, P. Kidkhunthod, *Walailak Journal of Science and Technology (WJST)* **2016**, *13*, 977.
[283] Y. You, X. Yu, Y. Yin, K.-W. Nam, Y.-G. Guo, *Nano research* **2015**, *8*, 117.
[284] R. Rehman, J. Peng, H. Yi, Y. Shen, J. Yin, C. Li, C. Fang, Q. Li, J. Han, *RSC Adv.* **2020**, *10*, 27033. DOI 10.1039/D0RA03490H.
[285] A. Zhou, Z. Xu, H. Gao, L. Xue, J. Li, J. B. Goodenough, *Small* **2019**, *15*, 1902420.
[286] Y. You, X.-L. Wu, Y.-X. Yin, Y.-G. Guo, *Energy Environ. Sci.* **2014**, *7*, 1643.
[287] X. Li, M. Li, Q. Yang, D. Wang, L. Ma, G. Liang, Z. Huang, B. Dong, Q. Huang, C. Zhi, *Adv. Energy Mater.* **2020**, *10*, 2001394.
[288] K. Lu, B. Song, Y. Zhang, H. Ma, J. Zhang, *J. Mater. Chem. A* **2017**, *5*, 23628.
[289] C. Li, J. Wu, F. Ma, Y. Chen, L. Fu, Y. Zhu, Y. Zhang, P. Wang, Y. Wu, W. Huang, *ACS Appl. Energy Mater.* **2019**, *2*, 6984.
[290] K. Lu, B. Song, J. Zhang, H. Ma, *J. Power Sources* **2016**, *321*, 257.
[291] C. Li, D. Zhang, F. Ma, T. Ma, J. Wang, Y. Chen, Y. Zhu, L. Fu, Y. Wu, W. Huang, *ChemSusChem* **2019**, *12*, 3732.
[292] M. Li, J. Lu, X. Ji, Y. Li, Y. Shao, Z. Chen, C. Zhong, K. Amine, *Nature Reviews Materials* **2020**, *5*, 276.
[293] J. Liu, Z. Bao, Y. Cui, E. J. Dufek, J. B. Goodenough, P. Khalifah, Q. Li, B. Y. Liaw, P. Liu, A. Manthiram, *Nature Energy* **2019**, *4*, 180.
[294] J. Zheng, Q. Zhao, T. Tang, J. Yin, C. D. Quilty, G. D. Renderos, X. Liu, Y. Deng, L. Wang, D. C. Bock, *Science* **2019**, *366*, 645.
[295] J. Hao, B. Li, X. Li, X. Zeng, S. Zhang, F. Yang, S. Liu, D. Li, C. Wu, Z. Guo, *Adv. Mater.* **2020**, *32*, 2003021.
[296] F. Xie, H. Li, X. Wang, X. Zhi, D. Chao, K. Davey, S. Z. Qiao, *Adv. Energy Mater.* **2021**, *11*, 2003419.
[297] J. Zheng, J. Yin, D. Zhang, G. Li, D. C. Bock, T. Tang, Q. Zhao, X. Liu, A. Warren, Y. Deng, *Sci. Adv.* **2020**, *6*, eabb1122.
[298] S. Li, J. Fu, G. Miao, S. Wang, W. Zhao, Z. Wu, Y. Zhang, X. Yang, *Adv. Mater.* **2021**, *33*, 2008424.
[299] M. Zhou, S. Guo, J. Li, X. Luo, Z. Liu, T. Zhang, X. Cao, M. Long, B. Lu, A. Pan, *Adv. Mater.* **2021**, *33*, 2100187.
[300] D. Yuan, J. Zhao, H. Ren, Y. Chen, R. Chua, E. T. J. Jie, Y. Cai, E. Edison, W. Manalastas Jr, M. W. Wong, *Angew. Chem.* **2021**, *133*, 7289.
[301] Q. Yang, G. Liang, Y. Guo, Z. Liu, B. Yan, D. Wang, Z. Huang, X. Li, J. Fan, C. Zhi, *Adv. Mater.* **2019**, *31*, 1903778.
[302] L. Ma, Q. Li, Y. Ying, F. Ma, S. Chen, Y. Li, H. Huang, C. Zhi, *Adv. Mater.* **2021**, *33*, 2007406.
[303] X. Jia, C. Liu, Z. G. Neale, J. Yang, G. Cao, *Chem. Rev.* **2020**, *120*, 7795.
[304] J. Zhou, M. Xie, F. Wu, Y. Mei, Y. Hao, L. Li, R. Chen, *Adv. Mater.* **2021**, 2106897.
[305] X. Yang, C. Li, Z. Sun, S. Yang, Z. Shi, R. Huang, B. Liu, S. Li, Y. Wu, M. Wang, **2021**.

[306] J. Zhao, J. Zhang, W. Yang, B. Chen, Z. Zhao, H. Qiu, S. Dong, X. Zhou, G. Cui, L. Chen, *Nano Energy* **2019**, *57*, 625.

[307] C. Deng, X. Xie, J. Han, Y. Tang, J. Gao, C. Liu, X. Shi, J. Zhou, S. Liang, *Adv. Funct. Mater.* **2020**, *30*, 2000599.

[308] P. Liang, J. Yi, X. Liu, K. Wu, Z. Wang, J. Cui, Y. Liu, Y. Wang, Y. Xia, J. Zhang, *Adv. Funct. Mater.* **2020**, *30*, 1908528.

[309] Z. Zhao, J. Zhao, Z. Hu, J. Li, J. Li, Y. Zhang, C. Wang, G. Cui, *Energy Environ. Sci.* **2019**, *12*, 1938.

[310] S. Bhoyate, S. Mhin, J.-e. Jeon, K. Park, J. Kim, W. Choi, *Acs Appl. Mater. Interfaces* **2020**, *12*, 27249.

[311] X. Zhang, J. Li, D. Liu, M. Liu, T. Zhou, K. Qi, L. Shi, Y. Zhu, Y. Qian, *Energy Environ. Sci.* **2021**, *14*, 3120.

[312] X. Li, Q. Li, Y. Hou, Q. Yang, Z. Chen, Z. Huang, G. Liang, Y. Zhao, L. Ma, M. Li, *ACS nano* **2021**, *15*, 14631.

[313] C. Sun, C. Wu, X. Gu, C. Wang, Q. Wang, *Nano-micro letters* **2021**, *13*, 1.

[314] N. Zhang, S. Huang, Z. Yuan, J. Zhu, Z. Zhao, Z. Niu, *Angew. Chem. Int. Ed.* **2021**, *60*, 2861.

[315] Y. An, Y. Tian, C. Liu, S. Xiong, J. Feng, Y. Qian, *ACS nano* **2021**, *15*, 15259.

[316] J. Zhang, Y. Zhao, X. Guo, C. Chen, C.-L. Dong, R.-S. Liu, C.-P. Han, Y. Li, Y. Gogotsi, G. Wang, *Nature Catalysis* **2018**, *1*, 985.

[317] H. Yang, Z. Chang, Y. Qiao, H. Deng, X. Mu, P. He, H. Zhou, *Angew. Chem. Int. Ed.* **2020**, *59*, 9377.

[318] X. Li, M. Li, K. Luo, Y. Hou, P. Li, Q. Yang, Z. Huang, G. Liang, Z. Chen, S. Du, *ACS nano* **2021**.

[319] L. Dong, W. Yang, W. Yang, H. Tian, Y. Huang, X. Wang, C. Xu, C. Wang, F. Kang, G. Wang, *Chem. Eng. J.* **2020**, *384*, 123355.

[320] Y. Yang, C. Liu, Z. Lv, H. Yang, Y. Zhang, M. Ye, L. Chen, J. Zhao, C. C. Li, *Adv. Mater.* **2021**, *33*, 2007388.

[321] P. Chen, X. Yuan, Y. Xia, Y. Zhang, L. Fu, L. Liu, N. Yu, Q. Huang, B. Wang, X. Hu, *Adv. Sci.* **2021**, 2100309.

[322] Q. Yang, Y. Guo, B. Yan, C. Wang, Z. Liu, Z. Huang, Y. Wang, Y. Li, H. Li, L. Song, *Adv. Mater.* **2020**, *32*, 2001755.

[323] C. Shen, X. Li, N. Li, K. Xie, J.-g. Wang, X. Liu, B. Wei, *Acs Appl. Mater. Interfaces* **2018**, *10*, 25446.

[324] T. Foroozan, V. Yurkiv, S. Sharifi-Asl, R. Rojaee, F. Mashayek, R. Shahbazian-Yassar, *Acs Appl. Mater. Interfaces* **2019**, *11*, 44077.

[325] X. Li, X. Yin, S. Liang, M. Li, L. Cheng, L. Zhang, *Carbon* **2019**, *146*, 210.

[326] R. Yuksel, O. Buyukcakir, W. K. Seong, R. S. Ruoff, *Adv. Energy Mater.* **2020**, *10*, 1904215.

[327] M. Chamoun, W. R. Brant, C.-W. Tai, G. Karlsson, D. Noréus, *Energy Storage Mater.* **2018**, *15*, 351.